UNIVERSITÀ
DI PARMA

DEPARTMENT OF CHEMISTRY, LIFE SCIENCES AND ENVIRONMENTAL SUSTAINABILITY

Doctoral Programme in Chemical Sciences
XXX Cycle

FROM MOLECULES TO MATERIALS:
STATIC AND DYNAMIC PROPERTIES OF COMPLEX SYSTEMS

Coordinator:
Prof. Roberto Corradini

Supervisor:
Prof. Anna Painelli

PhD student:
Francesco Di Maiolo

2014-2017

Contents

Introduction

Multifunctional molecular materials are highly promising for innovative applications in a large variety of fields, from telecommunications to electronics and spintronics, from photonics to biomedicine.[1, 2, 3, 4, 5] Molecular materials are in general constituted of cheap and abundant elements, show low environmental toxicity and good biocompatibility. They are lightweight, flexible and easy to process. Moreover a precise control of their structure is possible, down to the atomic level, and the powerful techniques of the molecular and supramolecular chemistry allow accessing a practically infinite series of systems. This same large number of possible structures points to the need of a precise understanding of the material properties and the definition of reliable structure-properties relationships as to be able to guide the synthesis towards specific materials with predefined behaviour and properties.

Multifunctional behaviour implies large and non-linear responses of the system to different external stimuli, including for example pressure, temperature, light, etc.[6, 7, 8] Multifunctional behaviour is generally observed in systems with a large electron delocalization and/or with low-lying charge-transfer (CT) degrees of freedom.[9, 10] Two different families of multifunctional molecular materials have been traditionally addressed in the host laboratory: CT dyes and their aggregates with main applications in non-linear optics, [11, 12, 13, 14, 15] and CT crystals, [16, 17, 18] a family of low-dimensional materials among which insulators, metals [19] and superconductors [20] materials are found and that are actively investigated for their ferroelectric [21] and multiferroic [22, 23] properties as well as for their exotic phase transitions.[24, 25, 26, 27]

Parametric Hamiltonians have been proposed and widely adopted in the host laboratory to study the two classes of materials and have been validated against optical spectroscopy data.[11, 14, 28, 29, 30, 31] Essential-state models (ESMs) are the models of choice for CT dyes and their aggregates. Intramolecular CT dominates the low-energy physics of these systems whose electronic structure is described in terms of a reduced number of electronic states, usually corresponding to the main resonating structures.[11, 14, 28] Selected vibrational modes, coupled to CT degrees of freedom, [12] are introduced leading to a coupled electron-vibration Hamiltonian that is diagonalized in a truly non-adiabatic approach.[32, 33, 34] The interaction of intramolecular CT with the environment is introduced in terms of electrostatic interactions with the surrounding, either the solvent (treated in the reaction-field approach) [11] or nearby molecules in an approach to molecular aggregates that goes beyond the exciton model approximations.[35, 36, 37, 38, 39, 40, 41]

Models of choice for CT crystals are based on the famous Hubbard model that accounts for the strongly correlated nature of delocalized electrons in these systems.[42, 43, 44, 45] The intermolecular CT that governs the physics of these systems is described by the Hubbard model that has to be specialized for each system at hand to account for different on-site energies (modified Hubbard model) and/or intermolecular electrostatic interactions (extended Hubbard model).[26, 46] The coupling with molecular vibrations (Holstein coupling) and lattice modes (Peierls coupling) [30, 47] has to be introduced to account for structural and/or electronic instabilities [48] as well as for spectral properties.[49, 31]

In this Thesis, we considerably extend the portfolio of models, methods and numerical approaches available in the host laboratory, moving along two different, yet not unrelated, directions:

1. defining the properties and the behaviour of materials where both intramolecular and intermolecular CT degrees of freedom play a role;
2. defining models and approaches to deal with energy relaxation in open quantum systems.

Low-dimensional systems combining inter and intramolecular CT are discussed in Chapter 2. Relevant model Hamiltonians are derived and diagonalized numerically on finite size systems, in a computationally demanding effort, to demonstrate a rich phase diagram with large stability regions for ferroelectric behaviour and a small, but sizeable, region of multiferroic behaviour. Optical spectra of specific systems are also discussed, showing intriguing properties.

Energy dissipation is central to describe optical spectra and while empirical band-broadening approaches are adequate and sufficiently reliable to describe steady-state spectra, a proper treatment of the relaxation of the quantum system due to the interaction with the environment (the so-called bath) is needed to describe more refined time-resolved spectra, including for example pump-probe [50, 51] and 2D-optical spectra.[52] This brings us in the fascinating field of open quantum systems, a hot research field that was introduced to the host laboratory by this Thesis work.

In Chapter 1, we start discussing relaxation in the simplest system: a photoexcited CT dye described in terms of ESMs. We critically discuss two different strategies to account for the coupling of molecular and environmental degrees of freedom. In the first approach, a chain of classical anharmonic oscillators is attached to the dye in such a way that energy is finally transferred towards a heat reservoir.[53, 54] The coupled quantum-classical hybrid system is then propagated in time in a sequential way using fourth-order Runge-Kutta integration for the quantum system and Verlet algorithm for the classical system. In the second approach, a bath of quantum harmonic oscillators exchanges vibrational quanta with the molecular system, leading to Redfield equation of motion for the reduced density matrix.[55] We use the Short-Iterative-Arnoldi (SIAM) algorithm to numerically integrate the equation. Both approaches lead to similar results and their merits and limitations are critically addressed. Both approaches are finally applied to the experimentally relevant system of resonance energy transfer. We considered two interacting dyes, an energy donor and an energy acceptor, both dyes being coupled to the dissipative bath. Using the two strategies described above, we were able to follow in real time the energy transfer from the excited energy donor molecule towards the energy acceptor.

In Chapter 3, relaxation is introduced in models for CT crystals as needed to address a recent series of ultrafast pump-probe experiments.[56, 57] These experiments use an ultrafast pump in the mid-infrared spectral region, following the time evolution of CT absorption spectra in the near-infrared region. This work is developed along several lines. After the definition and DFT-parametrization of the model Hamiltonian, we defined and numerically solved the coupled quantum-classical hybrid dynamics of the relevant quantum system coupled to a classical chain of dissipative anharmonic oscillators in turn coupled to a thermostat. Along these lines, we were able to reproduce the experimental spectra and, having gained confidence with the approach, we proposed a novel pump-probe experiment on a related system.

Chapter 1

Intermolecular resonance energy transfer

Intermolecular energy transfer describes a process where an excited molecule, called the energy donor, transfers its excess energy to a nearby molecule, called the energy acceptor, in a process that can be schematized as:

$$\mathcal{D}^* + \mathcal{A} \to \mathcal{D} + \mathcal{A}^*, \tag{1.1}$$

where $\mathcal{D}$ and $\mathcal{A}$ are the energy donor and acceptor, respectively, and the star is used to mark excited species. The most trivial mechanism for energy transfer corresponds to a radiative process, where the energy is transferred via a photon that, emitted by $\mathcal{D}^*$, is absorbed by $\mathcal{A}$ in a two-step process:

$$\begin{aligned} \mathcal{D}^* &\to \mathcal{D} + \hbar\omega_{\mathcal{D}}, \\ \mathcal{A} + \hbar\omega_{\mathcal{D}} &\to \mathcal{A}^*, \end{aligned} \tag{1.2}$$

where $\hbar$ is the Planck constant divided by 2π and $\omega_{\mathcal{D}}$ is the frequency of the exchanged photon. Radiative energy transfer may occur when the distance between $\mathcal{D}$ and $\mathcal{A}$ is larger than the photon wavelength (i.e, typically larger than 300 nm). Specific $\mathcal{D}\mathcal{A}$ interactions are not needed for radiative energy transfer, a process that only depends on the spectral overlap between donor emission and acceptor absorption bands and on the sample concentration.[58]

At shorter distances, energy transfer may occur through a single-step non-radiative process. At very short distances, when the intermolecular distance is smaller than the sum of the van der Waals radii (typically 3-4 Å) energy transfer may occur via a concerted electron-transfer process, in a mechanism known as Dexter energy transfer.[59, 60] For larger intermolecular distances, the intermolecular overlap of the orbitals is too weak to allow for a Dexter mechanism. Only electrostatic interactions survive, thus leading to the Resonance Energy Transfer (RET) phenomenon that can be described as the exchange of a virtual photon.[61]

RET plays a key role in photosynthesis, where solar energy absorbed by some chromophores (or aggregates of chromophores) is transferred in an extremely efficient way towards the reaction center. RET is also used by some jellyfish to change the color of the light emitted through bioluminescence. RET has many technological applications: it is exploited in biology to measure the distance between nano-objects (the molecular ruler application) [62] and it is used to design highly-efficient fluorescence sensors.[63] Energy storage and energy transport technologies rely on RET [64] and it is clear that a better understanding of the physics governing RET would lead to important improvements in both the fields of solar cells and light-emitting devices.

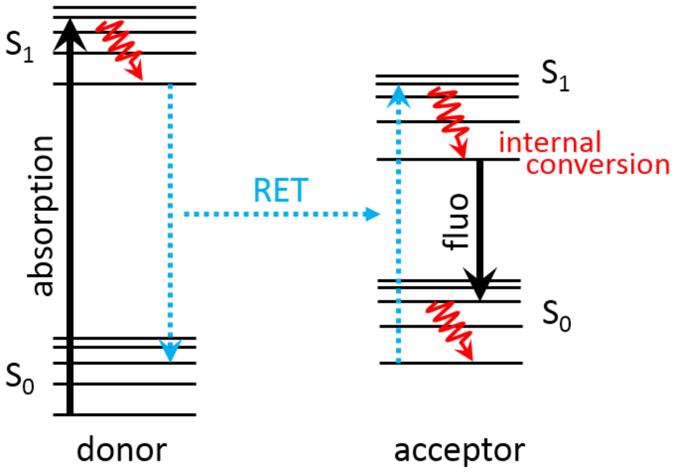

Figure 1.1: Simplified Jablonski diagram describing RET phenomenon.

The first theoretical description of RET dates back to 1948 with Förster groundbreaking work [65, 66, 67]. Förster theory of RET is based on the assumption that the vibrational relaxation of the excited donor is much faster than energy transfer towards the acceptor so that, as shown in the simplified Jablonsky diagram in Fig.1.1, the energy transfer occurs from the relaxed excited state of $\mathcal{D}$. The second hypothesis is that electrostatic interactions between the two molecules are weak if compared with intramolecular energies, making them amenable to a perturbative treatment. Accordingly, the zero order Hamiltonian is the sum of the two molecular Hamiltonians and the unperturbed states can be written as the direct product of the states describing the single molecules:

$$\begin{aligned} |\psi^*_{\mathcal{D}}\psi_{\mathcal{A}}\rangle &= |\psi^*_{\mathcal{D}}\rangle \otimes |\psi_{\mathcal{A}}\rangle, \\ |\psi_{\mathcal{D}}\psi^*_{\mathcal{A}}\rangle &= |\psi_{\mathcal{D}}\rangle \otimes |\psi^*_{\mathcal{A}}\rangle, \end{aligned} \tag{1.3}$$

where starred wave functions are used for molecular excited states. The RET rate can be calculated using the Fermi Golden Rule as:

$$\begin{aligned} k_{RET} &= \frac{2\pi}{\hbar}|V_{\mathcal{D}^*\mathcal{A},\mathcal{D}\mathcal{A}^*}|^2\delta(\omega_{\mathcal{D}} - \omega_{\mathcal{A}}) \\ &= \frac{2\pi}{\hbar}|\langle\psi^*_{\mathcal{D}}\psi_{\mathcal{A}}|\hat{V}|\psi_{\mathcal{D}}\psi^*_{\mathcal{A}}\rangle|^2\delta(\omega_{\mathcal{D}} - \omega_{\mathcal{A}}), \end{aligned} \tag{1.4}$$

where $\hbar$ is the reduced Planck constant, $\hat{V}$ is the quantum operator describing donor-acceptor interaction and $\delta(\omega_{\mathcal{D}} - \omega_{\mathcal{A}})$ is the Dirac δ distribution that guarantees energy conservation.

The interaction energy entering Eq.1.4 can be explicitly written as (SI units):

$$V_{\mathcal{D}^*\mathcal{A},\mathcal{D}\mathcal{A}^*} = \frac{e^2}{4\pi\varepsilon_0 n^2}\left\langle \psi^*_{\mathcal{D}}\psi_{\mathcal{A}} \middle| \frac{1}{\hat{\vec{r}}_{\mathcal{D}\mathcal{A}}} \middle| \psi_{\mathcal{D}}\psi^*_{\mathcal{A}} \right\rangle, \tag{1.5}$$

where e is the electron charge, ε_0 is the vacuum permittivity and n is the medium refractive index. Assuming $|\vec{r}_{\mathcal{D}\mathcal{A}}|$ larger than both donor and acceptor molecular sizes, Eq.1.5 can be rewritten in the dipolar approximation as:

$$V_{\mathcal{D}^*\mathcal{A},\mathcal{D}\mathcal{A}^*} = \frac{e^2}{4\pi\varepsilon_0 n^2}\left[\frac{\vec{\mu}^t_{\mathcal{D}}\vec{\mu}^t_{\mathcal{A}} - 3(\vec{\mu}^t_{\mathcal{D}}\vec{u}_{\mathcal{D}\mathcal{A}})(\vec{\mu}^t_{\mathcal{A}}\vec{u}_{\mathcal{D}\mathcal{A}})}{|\vec{r}_{\mathcal{D}\mathcal{A}}|^3}\right], \tag{1.6}$$

where $\vec{\mu}^t_{\mathcal{D}(\mathcal{A})}=\langle\psi^*_{\mathcal{D}(\mathcal{A})}|\hat{\vec{\mu}}_{\mathcal{D}(\mathcal{A})}|\psi_{\mathcal{D}(\mathcal{A})}\rangle$ is $\mathcal{D}(\mathcal{A})$ transition dipole moment as associated with the emission (absorption) process and $\vec{u}_{\mathcal{D}\mathcal{A}} = \vec{r}_{\mathcal{D}\mathcal{A}}/|\vec{r}_{\mathcal{D}\mathcal{A}}|$ is the unit vector associated with the center-to-center $\mathcal{DA}$ direction. Using Eq.1.6, the Fermi Golden Rule in Eq.1.4 can be recast as:

$$k_{RET} = \frac{\kappa^2}{16\pi^2\varepsilon_0^2\hbar^2 n^4}\frac{|\vec{\mu}^t_{\mathcal{D}}|^2|\vec{\mu}^t_{\mathcal{A}}|^2}{|\vec{r}_{\mathcal{DA}}|^6}\delta(\omega_{\mathcal{D}}-\omega_{\mathcal{A}}), \tag{1.7}$$

where the factor κ^2 depends on the relative $\mathcal{DA}$ orientation and is defined as:

$$\kappa = cos\vartheta_T - 3cos\vartheta_{\mathcal{D}}cos\vartheta_{\mathcal{A}}, \tag{1.8}$$

where the angles $\vartheta_{\mathcal{D}}$, $\vartheta_{\mathcal{A}}$ and ϑ_T are defined in Fig.1.2. In general, κ^2 can assume values going from 0 (perpendicular transition dipole moments) to 4 ($\vartheta_{\mathcal{D}} = \vartheta_{\mathcal{A}} = \vartheta_T = 0$); however, in non-viscous solutions, $\mathcal{D}$ and $\mathcal{A}$ transition dipole moments are assumed to span all possible spatial orientations before $\mathcal{D}^*$ deactivation happens; consequently, κ^2 can be replaced by its average value, $\langle\kappa^2\rangle = 2/3$. On the other hand, in viscous matrices (as well as solids), the randomization by rotational diffusion during $\mathcal{D}^*$ lifetime is hampered and the square of the average value of κ is used, $\kappa^2 = \langle\kappa\rangle^2 = 0.476$.

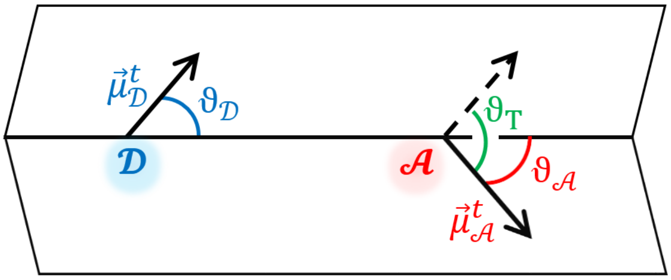

Figure 1.2: Sketch of $\mathcal{DA}$ transition dipole moments and relevant angles entering Eq.1.8.

As originally noticed by Förster [65], the rate in Eq.1.7 can be related to experimentally accessible quantities; more precisely, the transition dipole moment of $\mathcal{D}$ can be obtained from its fluorescence quantum yield, $\Phi_{\mathcal{D}}$, and life-time, $\tau_{\mathcal{D}}$, while the transition dipole moment of $\mathcal{A}$ can be obtained from the integrated absorption. Eq.1.7 can then be rewritten as:

$$k_{RET} = \frac{9000\ln(10)\kappa^2}{128\pi^5 n^4 N_A}\frac{\Phi_{\mathcal{D}}}{\tau_{\mathcal{D}}}\frac{J}{|\vec{r}_{\mathcal{DA}}|^6}, \tag{1.9}$$

where N_A is the Avogadro's number and J is the so-called overlap integral defined as:

$$J = \int_0^\infty d\nu \frac{F_{\mathcal{D}}(\nu)\varepsilon_{\mathcal{A}}(\nu)}{\nu^4}, \tag{1.10}$$

where $F_{\mathcal{D}}(\nu)$ is the area-normalized $\mathcal{D}$ fluorescence spectrum, while $\varepsilon_{\mathcal{A}}(\nu)$ is the $\mathcal{A}$ absorption molar extinction coefficient in units of $\mathrm{M}^{-1}\mathrm{cm}^{-1}$ and the integration is done over the wave number axis. From Eq.1.10 it is clear that J is connected to the overlap between the donor emission and the acceptor absorption spectral bands, ensuring energy conservation and thus playing a role similar to that of the Dirac δ distribution in Eqs.1.4 and 1.7.

Förster theory successfully describes RET, allowing the estimate of the energy transfer rate from quantities that can be estimated experimentally.[65, 66, 67] However, the theory gives no information about the dynamics of RET process. Indeed, fully dynamical models of RET are needed to address time-resolved spectra. Developing dynamical RET models is made non trivial by the need to describe dissipative phenomena competing with RET, thus bringing us in the realm of open quantum systems, i.e. of quantum systems interacting and exchanging energy with the environment. In the rest of the Chapter, we will present two fully dynamical approaches for RET.

The following Section introduces the reader to open quantum systems and to the two approaches we have investigated to study their dissipative dynamics, namely the quantum-classical hybrid approach (Subsection 1.1.1) and Redfield equation for the system reduced density matrix (Subsection 1.1.2). Section 1.2 presents the molecular model adopted in this work for both the energy donor and the energy acceptor. The dissipative dynamics of a coherently excited organic dye is discussed in Section 1.3, whereas Section 1.4 is fully devoted to the real time simulation of RET between two different organic chromophores. Preliminary results on the influence of polar solvation on RET dynamics are presented in Section 1.5, while concluding remarks are reported in Section 1.6.

1.1 Open quantum systems

A molecular system, $\mathcal{S}$, can not be considered a closed system since the interaction with the surrounding environment, $\mathcal{B}$, affects its state. Large effects on the system dynamics can be expected depending on the nature of the environment as well as on the strength of the interaction with the system. If $\mathcal{B}$ is macroscopically large and the $\mathcal{SB}$ coupling strength has a finite value, the energy given to $\mathcal{S}$ (for example by means of an externally applied electric field) will be transferred to $\mathcal{B}$ and, if the environment is in thermal equilibrium, then $\mathcal{S}$ will reach the relevant canonical equilibrium state as well, with the reservoir acting as a heat bath, in a process known as dissipation. However, if $\mathcal{B}$ is small in size, the energy is likely to flow back from $\mathcal{B}$ to $\mathcal{S}$ in what is called Poincaré recurrence.[68, 69] Here we are interested in dissipative phenomena.

In either case, the vector space of the total $\mathcal{SB}$ system can be defined as the direct product of the Hilbert space associated with the system, $\mathcal{H}_{\mathcal{S}}$, times the Hilbert space associated with the environment, $\mathcal{H}_{\mathcal{B}}$:

$$\mathcal{H}_{\mathcal{SB}} = \mathcal{H}_{\mathcal{S}} \otimes \mathcal{H}_{\mathcal{B}}. \tag{1.11}$$

The total $\mathcal{SB}$ Hamiltonian can be written as:

$$\hat{H}_{\mathcal{SB}} = \hat{H}_{\mathcal{S}} + \hat{H}_{\mathcal{B}} + \hat{H}_I, \tag{1.12}$$

where $\hat{H}_{\mathcal{S}}$ is the relevant open system Hamiltonian, $\hat{H}_{\mathcal{B}}$ is the environment Hamiltonian, while $\hat{H}_I$ is the system-environment interaction Hamiltonian.

Indeed, the study of the $\mathcal{SB}$ dynamics is a challenging task due to the enormous number of variables describing the reservoir (or heat bath). Several approximation schemes must be adopted in order to attack the problem of dissipative dynamics.

1.1.1 A quantum-classical hybrid approach to open quantum system dynamics

Studying open quantum systems, one possible approach is to use a classical description of the environment, while still keeping a fully quantum treatment of the system of interest in what is called a quantum-classical hybrid approach. We define $\vec{q}(t) = \{q_i(t)\}$ and $\vec{p}(t) = \{p_i(t)\}$ as the environment time-dependent coordinates and momenta, respectively, so that a reservoir state is represented by a point $(\vec{q}(t), \vec{p}(t))$ in its classical phase space. Assuming that the system-environment interaction Hamiltonian is only described by the environment coordinates, $\hat{H}_I(\vec{q}(t))$, the quantum part of the coupled quantum-classical dynamics can be described through a Schrödinger equation:

$$i\hbar\frac{\partial\Psi(t)}{\partial t} = \left[\hat{H}_{\mathcal{S}} + \hat{H}_I(\vec{q}(t))\right]\Psi(t). \tag{1.13}$$

The classical dynamics of the isolated classical system obeys the equations of motion:

$$\frac{dq_i(t)}{dt} = \frac{\partial H_{\mathcal{B}}(\vec{q},\vec{p})}{\partial p_i}, \quad \frac{dp_i(t)}{dt} = -\frac{\partial H_{\mathcal{B}}(\vec{q},\vec{p})}{\partial q_i}, \tag{1.14}$$

where $H_{\mathcal{B}}$ is a scalar function. In the presence of $\mathcal{SB}$ interaction Hamiltonian an additional potential is felt by the environment and must be accounted for while writing Hamilton's equations of motion; adopting a mean-field approach, the additional force acting on the i-th reservoir coordinate reads:

$$F_i = -\frac{\partial}{\partial q_i}\langle\hat{H}_I(\vec{q}(t))\rangle. \tag{1.15}$$

The coupled quantum-classical dynamics is calculated solving Eq.1.13 together with Eq.1.14 modified in order to account for Eq.1.15. In this way, contributions from the classical reservoir dynamics contaminate the quantum time-evolution and viceversa, thus accounting for the reciprocal $\mathcal{SB}$ feedback. Moreover, in the thermodynamic limit for the reservoir, the environment will affect the system in a non-trivial and almost random way, thus making a Langevin description of the classical dynamics preferable to the canonical equations.

Langevin equation of motion in the Markovian (i.e. non-memory) limit reads:[70, 71]

$$\frac{d^2q_i}{dt^2} = F_i - \gamma\frac{dq_i}{dt} + R(t), \tag{1.16}$$

where $F_i = -\partial H_{\mathcal{B}}/\partial q_i$ is the external force acting on q_i, γ is the static friction coefficient and $R(t)$ is a time-dependent random force. Crucially, Eq.1.16 replaces a large number of $\mathcal{B}$ degrees of freedom by means of the friction coefficient, γ, and the random force, $R(t)$, thus drastically reducing the computational effort required to simulate a reservoir.

The stochastic force, $R(t)$, is modelled in terms of a Gaussian random variable:

$$\langle R(t)\rangle = 0, \quad \langle R_i(t)R_{i'}(t')\rangle = C\delta_{i,i'}\delta(t-t'), \tag{1.17}$$

where C is a positive constant, $\delta_{i,i'}$ ensures short-range correlation and $\delta(t-t')$ underlines the Markovian nature of $R(t)$. The nature of the random force is completely defined by its first two momenta:

$$\left\langle \frac{dq_i(t)}{dt} \right\rangle = 0, \quad \left\langle \left(\frac{dq_i(t)}{dt} \right)^2 \right\rangle = \frac{C}{2\gamma}, \tag{1.18}$$

easily obtained by Fourier transforming (forward and backward) Eq.1.16. Furthermore, using the equipartition theorem, the C constant reads:

$$C = 2\gamma k_b T, \tag{1.19}$$

where k_b is the Boltzmann constant and T is the reservoir temperature. Using Eq.1.19, the random force correlation function becomes:

$$\langle R_i(t) R_{i'}(t') \rangle = 2\gamma k_b T \delta_{i,i'} \delta(t-t'), \tag{1.20}$$

that is the *fluctuation-dissipation* theorem, the variance of the random fluctuating force being proportional to the friction coefficient.[72] The Langevin equation of motion can be conveniently rewritten as:

$$\frac{d^2 q_i}{dt^2} = F_i - \gamma \frac{dq_i}{dt} + \sqrt{2\gamma k_b T} y(t), \tag{1.21}$$

where $\langle y(t) y(t') \rangle = \delta(t-t')$. Although neither $R(t)$ nor $y(t)$ are differentiable, a Wiener process, $w(t)$, can be introduced as:

$$y(t) = \frac{dw(t)}{dt}. \tag{1.22}$$

Moreover, assuming a sufficiently small Δt time-step, a Wiener process evolves in time according to the equation:

$$w(t+\Delta t) = w(t) + \sqrt{\Delta t}\zeta, \tag{1.23}$$

where ζ is a Gaussian random variable of unit width and zero mean; using these results, Eq.1.21 becomes:

$$\frac{d^2 q_i}{dt^2} = F_i - \gamma \frac{dq_i}{dt} + \sqrt{\frac{2\gamma k_b T}{\Delta t}}\zeta, \tag{1.24}$$

that can be numerically solved (for example using Verlet algorithm).

Summing up, the quantum-classical hybrid approach to the dynamics of open quantum systems explicitly treats both the system and the environment degrees of freedom. The quantum system is treated in a fully quantum-mechanical way (through time-dependent Schrödinger equation), while the classical system is attacked exploiting either canonical Hamilton's equations or Langevin dynamics. The expectation value of the time-dependent $\mathcal{SB}$ interaction Hamiltonian is used to couple the quantum and the classical dynamics.

1.1.2 A reduced approach to open quantum system dynamics

In this Subsection, we will attack the problem of the dynamics of open quantum system by exploiting the powerful approach of the reduced density matrix. The total density matrix for the coupled $\mathcal{SB}$ system reads:

$$\hat{\rho}(t) \quad = \quad \sum_k P_k |\phi_k(t)\rangle\langle\phi_k(t)|, \tag{1.25}$$

where $|\phi_k(t)\rangle$ are the quantum states available to the $\mathcal{SB}$ system, each populated with probability P_k. Diagonal and off-diagonal elements of $\hat{\rho}$ are called populations and coherences, respectively. The expectation value of a generic quantum mechanical operator, $\hat{O}$, defined in the total Hilbert space, $\mathcal{H}_{\mathcal{SB}}$, can be calculated as:

$$\langle\hat{O}(t)\rangle = \sum_k P_k \langle\phi_k(t)|\hat{O}|\phi_k(t)\rangle = Tr\{\hat{\rho}(t)\hat{O}\}. \tag{1.26}$$

The total density operator, $\hat{\rho}(t)$, evolves in time according to the Liouville-von Neumann equation of motion:

$$\frac{\partial\hat{\rho}(t)}{\partial t} = \frac{1}{i\hbar}[\hat{H}_{\mathcal{SB}}, \hat{\rho}(t)] = \frac{-i}{\hbar}\mathcal{L}_{\mathcal{SB}}\hat{\rho}(t), \tag{1.27}$$

where $\mathcal{L}_{\mathcal{SB}} = [\hat{H}_{\mathcal{SB}}, ...]$ is the Liouvillian super-operator. In analogy with Eq.1.12, a partitioning of the total Liouvillian is possible, thus getting $\mathcal{L}_{\mathcal{SB}} = \mathcal{L}_{\mathcal{S}} + \mathcal{L}_{\mathcal{B}} + \mathcal{L}_I$.

The reduced density matrix, $\hat{\sigma}(t)$, is defined by taking the trace of the total density operator, $\hat{\rho}(t)$, over the environment degrees of freedom:

$$\hat{\sigma}(t) \quad = \quad Tr_b\{\hat{\rho}(t)\}. \tag{1.28}$$

The average value of an operator, $\hat{O}'$, defined in the system Hilbert space, $\mathcal{H}_S$, is calculated as:

$$\langle \hat{O}'(t) \rangle \;=\; Tr\{\hat{\sigma}(t)\hat{O}'\}. \tag{1.29}$$

This equation tells us that the knowledge of the reduced density matrix is enough as long as we are only interested in the system properties.

In order to derive the exact equation of motion for $\hat{\sigma}(t)$, Zwanzig projection super-operator, $\mathcal{P}$, and its complementary version, $\mathcal{Q}$, are typically introduced:[73, 74]

$$\mathcal{P} = \hat{\rho}_b \otimes Tr_b\{...\}, \tag{1.30}$$

$$\mathcal{Q} = 1 - \mathcal{P}, \tag{1.31}$$

where $\hat{\rho}_b$ is the environment reduced density matrix, representing a stationary reference state of $\mathcal{B}$.

Tracing out the environment degrees of freedom, $\mathcal{P}$ projects the total $\mathcal{SB}$ density operator, $\hat{\rho}(t)$, on $\mathcal{S}$ states:

$$\mathcal{P}\hat{\rho}(t) = \hat{\rho}_b \otimes Tr_b\{\hat{\rho}(t)\} = \hat{\rho}_b \otimes \hat{\sigma}(t), \tag{1.32}$$

whereas $\mathcal{Q}$ projects $\hat{\rho}(t)$ on $\mathcal{B}$ states.

Zwanzig projection super-operator satisfies the following relations:

$$[\mathcal{L}_{\mathcal{S}}, \mathcal{P}] = 0, \quad \mathcal{L}_{\mathcal{B}}\mathcal{P} = \mathcal{P}\mathcal{L}_{\mathcal{B}} = 0. \tag{1.33}$$

Moreover, assuming $Tr_b\{\hat{H}_I\hat{\rho}_b\}$=0 and using Eq.1.30, we get:

$$\mathcal{P}\mathcal{L}_I\mathcal{P} = 0. \tag{1.34}$$

Multiplying both sides of Eq.1.27 from the left by either $\mathcal{P}$ or $\mathcal{Q}$ and integrating, the equation of motion associated with $\mathcal{P}\hat{\rho}(t)$ is obtained:[75]

$$\begin{aligned}\frac{d}{dt}\mathcal{P}\hat{\rho}(t) \;&=\; -\frac{i}{\hbar}\mathcal{P}\mathcal{L}_{\mathcal{SB}}\mathcal{P}(\mathcal{P}\hat{\rho}(t)) \\ &\quad+\left(\frac{i}{\hbar}\right)^2 \int_0^t d\tau \mathcal{P}\mathcal{L}_{\mathcal{SB}}\mathcal{Q}e^{-\frac{i}{\hbar}\mathcal{Q}\mathcal{L}_{\mathcal{SB}}\mathcal{Q}\tau}\mathcal{Q}\mathcal{L}_{\mathcal{SB}}\mathcal{P}(\mathcal{P}\hat{\rho}(t-\tau)).\end{aligned} \tag{1.35}$$

Using Eqs.1.31, 1.33 and 1.34, the equation can be recast as:

$$\begin{aligned}\frac{d}{dt}\mathcal{P}\hat{\rho}(t) \;&=\; -\frac{i}{\hbar}\mathcal{L}_{\mathcal{S}}\mathcal{P}\hat{\rho}(t) \\ &\quad+\left(\frac{i}{\hbar}\right)^2 \int_0^t d\tau \mathcal{P}\mathcal{L}_I e^{-\frac{i}{\hbar}\mathcal{Q}\mathcal{L}_{\mathcal{SB}}\mathcal{Q}\tau}\mathcal{L}_I\mathcal{P}\hat{\rho}(t-\tau),\end{aligned} \tag{1.36}$$

where we used the idempotency of Zwanzig projection super-operator, $\mathcal{P}^2 = \mathcal{P}$, and it is assumed $\mathcal{Q}\hat{\rho}(0) = 0$.

Looking at the right-hand side of Eq.1.36, the first line describes the system dynamics in the absence of the environment, while the second line contains the relaxation super-operator. Eq.1.36 is known as Nakajima-Zwanzig equation, [74] it is exact, but it is difficult to solve; however, assuming weak $\mathcal{S}B$ interactions, the Born approximation can be used, setting $\mathcal{L}_{\mathcal{SB}} \simeq \mathcal{L}_{\mathcal{S}} + \mathcal{L}_{\mathcal{B}}$. Consequently, the relaxation super-operator can be rewritten as:

$$\begin{aligned} \mathcal{P}\mathcal{L}_I e^{-\frac{i}{\hbar}\mathcal{Q}\mathcal{L}_{\mathcal{SB}}\mathcal{Q}\tau}\mathcal{L}_I &\simeq \mathcal{P}\mathcal{L}_I e^{-\frac{i}{\hbar}\mathcal{Q}(\mathcal{L}_{\mathcal{S}}+\mathcal{L}_{\mathcal{B}})\mathcal{Q}\tau}\mathcal{L}_I \\ &\simeq \mathcal{P}\mathcal{L}_I e^{-\frac{i}{\hbar}(\mathcal{L}_{\mathcal{S}}+\mathcal{L}_{\mathcal{B}})\tau}\mathcal{L}_I, \end{aligned} \tag{1.37}$$

where the second line is demonstrated in Appendix A.

Plugging Eq.1.37 into Eq.1.36 and using $\mathcal{P}$ projection super-operator (Eq.1.32), Nakajima-Zwanzig equation becomes:

$$\begin{aligned} \frac{d}{dt}\hat{\sigma}(t) &= -\frac{i}{\hbar}\mathcal{L}_{\mathcal{S}}\hat{\sigma}(t) \\ &+ \left(\frac{i}{\hbar}\right)^2 \int_0^t d\tau \left\langle \mathcal{L}_I e^{-\frac{i}{\hbar}(\mathcal{L}_{\mathcal{S}}+\mathcal{L}_{\mathcal{B}})\tau}\mathcal{L}_I \right\rangle_b \hat{\sigma}(t-\tau), \end{aligned} \tag{1.38}$$

where $\langle ... \rangle_b \equiv Tr_b\{(...)\hat{\rho}_b\}$.

Remembering the interaction representation of a generic $\mathcal{SB}$ operator, $\hat{O}$:

$$\hat{O}(-\tau) = e^{-\frac{i}{\hbar}(\hat{H}_{\mathcal{S}}+\hat{H}_{\mathcal{B}})\tau}\hat{O}e^{\frac{i}{\hbar}(\hat{H}_{\mathcal{S}}+\hat{H}_{\mathcal{B}})\tau}, \tag{1.39}$$

the relaxation super-operator is rewritten as:

$$\left\langle \mathcal{L}_I e^{-\frac{i}{\hbar}(\mathcal{L}_{\mathcal{S}}+\mathcal{L}_{\mathcal{B}})\tau}\mathcal{L}_I \right\rangle_b = \left\langle \mathcal{L}_I \mathcal{L}_I(-\tau) e^{-\frac{i}{\hbar}(\mathcal{L}_{\mathcal{S}}+\mathcal{L}_{\mathcal{B}})\tau} \right\rangle_b. \tag{1.40}$$

Furthermore, adopting the (Markov) approximation, $\hat{\sigma}(t-\tau) \simeq exp[i\mathcal{L}_{\mathcal{S}}\tau/\hbar]\hat{\sigma}(t)$ and remembering that $\hat{\rho}_b$ is a bath time non-dependent reference state, Eq.1.38 becomes:

$$\begin{aligned} \frac{d}{dt}\hat{\sigma}(t) &= -\frac{i}{\hbar}\mathcal{L}_{\mathcal{S}}\hat{\sigma}(t) \\ &+ \left(\frac{i}{\hbar}\right)^2 \int_0^\infty d\tau \left\langle \mathcal{L}_I(0)\mathcal{L}_I(-\tau) \right\rangle_b \hat{\sigma}(t), \end{aligned} \tag{1.41}$$

where the upper limit of the integral is sent to infinity, having assumed the integrand decays to zero after a short time (stationary relaxation tensor approximation [76, 77]). Expanding the Liouvillians, Eq.1.41 becomes:

$$\begin{aligned}\frac{d}{dt}\hat{\sigma}(t) &= -\frac{i}{\hbar}[\hat{H}_{\mathcal{S}}, \hat{\sigma}(t)] \\ &+ \left(\frac{i}{\hbar}\right)^2 \int_0^\infty d\tau \; Tr_b \Big\{ \Big[\hat{H}_I(0), [\hat{H}_I(-\tau), \hat{\rho}_b \otimes \hat{\sigma}(t)]\Big] \Big\}, \end{aligned} \tag{1.42}$$

which is Redfield equation.[55] Crucially, the second line represents the Redfield relaxation super-operator, R, and describes the dissipative effect of the environment on the system dynamics.

Rewriting the Redfield equation with respect to $\hat{H}_{\mathcal{S}}$ eigenstates results:

$$\frac{d}{dt}\sigma_{ab}(t) = -i\omega_{ab}\sigma_{ab}(t) + \sum_{c,d} R_{ab,cd}\sigma_{cd}(t), \quad \forall\ a, b = 1, ..., N, \tag{1.43}$$

where $\sigma_{ab}(t) = \langle a|\hat{\sigma}(t)|b\rangle$ is the generic matrix element of the system reduced density matrix, $\omega_{ab} = (E_a - E_b)/\hbar$ is the relevant transition frequency and N is the $\hat{H}_{\mathcal{S}}$ dimension. The relaxation super-operator element, $R_{ab,cd}$, is conveniently rewritten as:

$$R_{ab,cd} = -\delta_{b,d}\sum_e \Gamma^+_{ae,ec} - \delta_{a,c}\sum_e \Gamma^-_{de,eb} + \Gamma^+_{db,ac} + \Gamma^-_{db,ac}, \tag{1.44}$$

where $\delta_{b,d}$ and $\delta_{a,c}$ are Kronecker delta symbols acting on $\hat{H}_{\mathcal{S}}$ eigenstates and where the Fourier-Laplace transforms of the $\mathcal{B}$ correlation functions are introduced:[78]

$$\begin{aligned}\Gamma^+_{db,ac} &= \frac{1}{\hbar^2}\int_0^\infty d\tau e^{-i\omega_{ac}\tau}\langle \hat{H}^I_{db}(0)\hat{H}^I_{ac}(-\tau)\rangle_b, \\ \Gamma^-_{db,ac} &= \frac{1}{\hbar^2}\int_0^\infty d\tau e^{-i\omega_{db}\tau}\langle \hat{H}^I_{db}(-\tau)\hat{H}^I_{ac}(0)\rangle_b, \end{aligned} \tag{1.45}$$

where $\hat{H}^I_{db}$ is the $\hat{H}_I$ matrix element between $|d\rangle$ and $|b\rangle$ eigenstates.

When $a = b\ \wedge c = d\ \wedge a \neq c$, Eq.1.44 describes population transfer between the system states; on the other hand, decoherence phenomena are described by the components $R_{ab,ab}$, where $a \neq b$. Moreover, $R_{ab,cd}$ terms, where $a \neq b \neq c \neq d$, describe coherence transfer between different couples of states; $R_{aa,cd}$, where $a \neq c \neq d$, describes population to coherence transformation, while $R_{ab,cc}$, where $a \neq b \neq c$, describes the coherence to population conversion. Consequently, while solving Eq.1.43, many different $\hat{\sigma}(t)$ elements are mixed by the relaxation super-operator.

Indeed, this picture can be simplified in a significant way by adopting the *secular approximation* that amounts to neglect all the rapidly oscillating (i.e. non-secular) $R_{ab,cd}$ components.[55, 79] In this approximation only $R_{aa,cc}$ and $R_{ab,ab}$ terms survive together with the special $R_{ab,cd}$ elements that satisfy the resonance condition $|\omega_{ab} - \omega_{cd}| = 0$. Crucially, if only $R_{aa,cc}$ and $R_{ab,ab}$ components are kept, the Redfield equation boils down to the Bloch model. The Bloch model leads to a decoupling of populations and coherences, the former evolving according to Pauli master equation:

$$\frac{d}{dt}\sigma_{aa}(t) \quad = \quad \sum_c R_{aa,cc}\sigma_{cc}(t), \quad \forall a = 1, ..., N, \tag{1.46}$$

the latter according to:

$$\sigma_{ab}(t) \quad = \quad \sigma_{ab}(0)e^{(R_{ab,ab} - i\omega_{ab})t}. \tag{1.47}$$

However, when several non-secular terms enter the system-bath dynamics, the secular approximation and consequently the Bloch model should not be used. This typically happens in systems with multiple vibrational coordinates (sometimes called multicomponent systems), where several states can be close in energy without being degenerate.[80] In these cases, a pseudo non-secular algorithm can be used;[81] setting a threshold, α, one can keep the most important $R_{ab,cd}$ non-secular terms, i.e. those satisfying the relation $|\omega_{ab} - \omega_{cd}| \leq \alpha$.

In conclusion, introducing Zwanzig projection super-operator, $\mathcal{P}$, (Eq.1.30) it was possible to derive the exact equation of motion for the system reduced density matrix, namely Nakajima-Zwanzig equation (Eq.1.36). Furthermore, assuming the weak-coupling limit for the $\mathcal{SB}$ interactions (i.e. Born approximation) and adopting Markov approximation, Redfield equation was derived (Eq.1.42). Both Nakajima-Zwanzig equation and Redfield equation were obtained with no explicit treatment of the environment dynamics, but just focusing on its effect on the system.

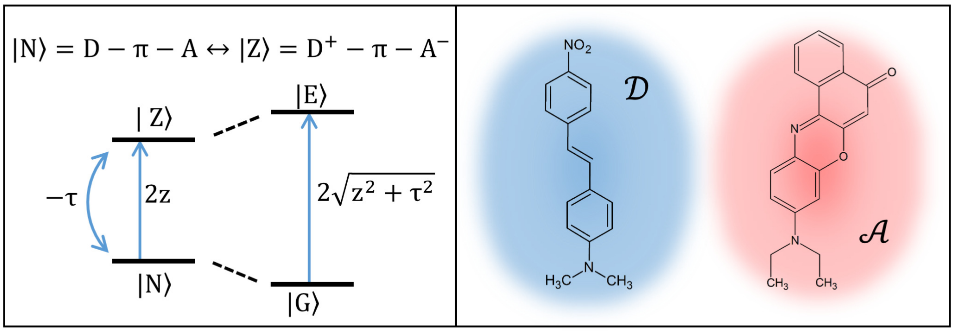

Figure 1.3: CT dipolar chromophores. Left panel: sketch of the two-state model used for a D-π-A dye. Right panel: molecular structures of two different dipolar dyes, namely p,p'-dimethylaminonitrostilbene (DANS) and 9-diethylamino-5-benzo[α]phenoxazinone (Nile Red).

1.2 Essential-state models

Charge-transfer (CT) chromophores are π-conjugated molecules decorated with electron-donor (D) and electron-acceptor (A) moieties (not to be confused with energy donor, $\mathcal{D}$, and energy acceptor, $\mathcal{A}$), to give polar (D-π-A), [11, 12, 13, 82] quadrupolar (D-π-A-π-D or A-π-D-π-A) [14, 82, 83, 84] or octupolar (A(-π-D)$_3$ or D(-π-A)$_3$) [28, 85, 86] molecular species. Low-energy optical spectra of CT chromophores are governed by charge resonance between D and A groups and have been successfully described using essential-state models (ESMs). ESMs account for CT degrees of freedom in terms of a minimal set of electronic states, corresponding to the main resonating structures of the CT chromophore at hand. In particular, two electronic states are used to describe dipolar dyes since they resonate between two main structures, D-π-A and D$^+$-π-A$^-$ (Fig.1.3, left panel);[11, 12, 13] three and four electronic states are used to model quadrupolar [87, 88] and octupolar [28, 87] CT dyes, respectively. Coupling between electrons and nuclei [12] as well as polar solvation effects [11] can be introduced straightforwardly in order to describe linear and non-linear optical spectra in solution. Moreover and crucially for RET, ESMs can be extended in order to treat interacting chromophores (Sect.1.4).[35, 37, 38, 39, 40, 41]

1.2.1 Essential two-state model for dipolar dyes

Polar (D-π-A) chromophores resonate between a neutral structure, D-π-A, and a zwitterionic structure, D$^+$-π-A$^-$. Accordingly, the relevant ESM is defined by two electronic states, $|N\rangle$ and $|Z\rangle$ (Fig.1.3, left panel).[11, 12] The two basis states are separated by $2z$ energy and mutually mixed by the CT integral, $-\tau$, leading to the following electronic Hamiltonian:

$$\hat{H}_{el} = \begin{pmatrix} 0 & -\tau \\ -\tau & 2z \end{pmatrix} = -\tau\hat{\sigma} + 2z\hat{\rho}, \tag{1.48}$$

where $\hat{\sigma} = |N\rangle\langle Z| + |Z\rangle\langle N|$ and $\hat{\rho} = |Z\rangle\langle Z|$ are the hopping and the ionicity operators, respectively. $\hat{H}_{el}$ can be easily diagonalized, thus leading to the eigenvalues $\mathcal{E}_G = z - \sqrt{z^2+\tau^2}$ and $\mathcal{E}_E = z + \sqrt{z^2+\tau^2}$ and eigenstates:

$$\begin{aligned} |G\rangle &= \sqrt{1-\rho}|N\rangle + \sqrt{\rho}|Z\rangle, \\ |E\rangle &= -\sqrt{\rho}|N\rangle + \sqrt{1-\rho}|Z\rangle, \end{aligned} \tag{1.49}$$

where $\rho = \langle G|\hat{\rho}|G\rangle$ and $1-\rho = \langle E|\hat{\rho}|E\rangle$ measure the degree of CT in the ground state and in the excited state, respectively, and ρ is fully defined by the model parameters as:

$$\rho = \frac{1}{2}\left(1 - \frac{z}{\sqrt{z^2+\tau^2}}\right). \tag{1.50}$$

In terms of ρ, the CT transition energy is:

$$\Delta\mathcal{E}_{CT} = \frac{\tau}{\sqrt{\rho(1-\rho)}}. \tag{1.51}$$

In order to study optical properties, an electric dipole moment operator must be defined and, following Mulliken, [89] it can be written as:

$$\hat{\mu} = \begin{pmatrix} 0 & 0 \\ 0 & \mu_0 \end{pmatrix} = \mu_0\hat{\rho}, \tag{1.52}$$

where μ_0 is the dipole moment associated with $|Z\rangle$, assumed to be much bigger than all the other matrix elements of $\hat{\mu}$. As a consequence, $\mu_0\rho$ is the chromophore permanent dipole moment, whereas $\mu_0(1-\rho)$ is the dipole moment in $|E\rangle$; the CT transition dipole moment is $\mu_{CT} = \langle G|\hat{\mu}|E\rangle = \mu_0\sqrt{\rho(1-\rho)}$.

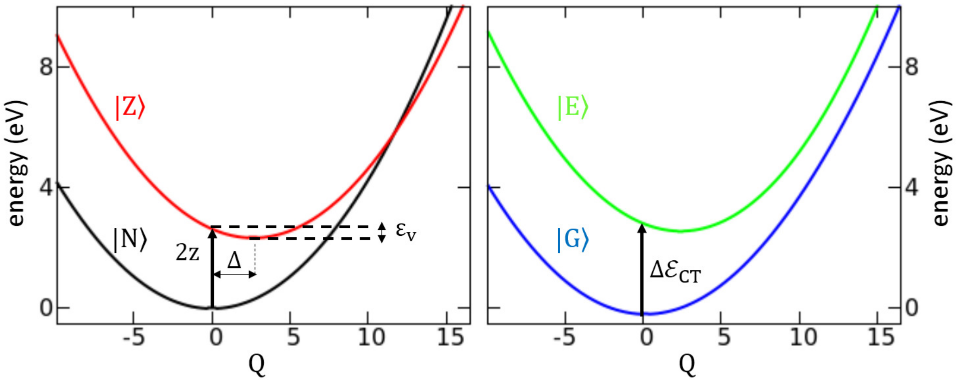

Figure 1.4: Potential energy curves associated with the diabatic (left panel) and adiabatic (right panel) states of DANS (model parameters in Tab.1.1, first line). Vibrational relaxation energy, ε_v, and potential energy curves minima displacement, Δ, are highlighted in the left panel.

To describe the shape of optical spectra of CT chromophores, electron-vibration coupling must be taken into account and to this end, a dimensionless effective molecular coordinate, $\hat{Q}$, and its conjugated momentum, $\hat{P}$, are introduced.[11, 12, 90, 41] We assume harmonic potential energy curves for the diabatic N and Z states (Fig.1.4, left panel). The electron-nuclear total Hamiltonian written on the diabatic basis reads:

$$\hat{H} \quad = \quad -\tau\hat{\sigma} + \left(2z - \sqrt{\hbar\omega_v\varepsilon_v}\hat{Q}\right)\hat{\rho} + \frac{\hbar\omega_v}{4}(\hat{P}^2 + \hat{Q}^2), \tag{1.53}$$

where ω_v is the vibrational frequency associated with $\hat{Q}$ and ε_v is the relevant vibrational relaxation energy:

$$\varepsilon_v \quad = \quad \frac{\hbar\omega_v}{4}\Delta^2, \tag{1.54}$$

where Δ is defined in Fig.1.4, left panel.

In the adiabatic approximation the nuclear kinetic energy is neglected. The resulting adiabatic Hamiltonian, $\hat{H}(Q)$, can be analytically diagonalized for different Q values, thus leading to the adiabatic states $|G(Q)\rangle$ and $|E(Q)\rangle$ shown in Figure 1.4, right panel.

In a non-adiabatic approach, electrons and nuclei are treated on the same footing and both $\hat{Q}$ and $\hat{P}$ are treated as quantum operators:[91, 92, 93, 41]

$$\hat{Q} = (\hat{a}^\dagger + \hat{a}), \tag{1.55}$$

$$\hat{P} = i(\hat{a}^\dagger - \hat{a}), \tag{1.56}$$

where $\hat{a}^\dagger$ and $\hat{a}$ are the bosonic creation and annihilation operators, respectively, and i is the imaginary unit. The Hamiltonian in Eq.1.53 is rewritten as:

$$\hat{H} \;=\; -\tau\hat{\sigma} + 2z\hat{\rho} - \sqrt{\hbar\omega_v\varepsilon_v}(\hat{a}^\dagger + \hat{a})\hat{\rho} + \hbar\omega_v\left(\hat{a}^\dagger\hat{a} + \frac{1}{2}\right). \tag{1.57}$$

The non-adiabatic vector space, $\mathcal{V}_{NA}$, is defined as the direct product of the two-dimensional electronic Hilbert space, $\mathcal{H}_{el}$, spanned by the two electronic states ($|N\rangle$ and $|Z\rangle$) times the ∞-dimensional Fock space, $\mathcal{F}$, spanned by the eigenstates of the harmonic oscillator associated with $\hat{Q}$:

$$\begin{aligned}\mathcal{V}_{NA} &= \mathcal{H}_{el} \otimes \mathcal{F} \\ &= \mathcal{H}_{el} \otimes \left(\bigoplus_{n=0}^{\infty} \mathcal{F}^n\right).\end{aligned} \tag{1.58}$$

The Hamiltonian matrix in Eq.1.57 is written on the basis set spanning $\mathcal{V}_{NA}$ vector space; however, in order to make the problem numerically tractable, $\mathcal{F}$ space is truncated to the m lowest vibrational excitations, thus leading to a $2m\times2m$ sparse Hamiltonian matrix that can be numerically diagonalized. Of course, m is chosen large enough as to reach convergence on relevant properties (typically, results for $m\sim$15-16 are shown in this Chapter).

The non-adiabatic eigenstates, $|\phi_k\rangle$, are neither electronic nor vibrational in nature, but are rather *vibronic* states, describing the coupled nuclear-electronic motion. Non-adiabatic steady-state absorption spectra can be calculated from $|\langle\phi_1|\hat{\mu}|\phi_k\rangle|^2$, for k=2,...,$2m$, where $\hat{\mu}$ is the dipole moment operator defined in Eq.1.52 and projected on the basis spanning $\mathcal{V}_{NA}$ vector space. Calculated absorption and fluorescence spectra for the two CT dipolar chromophores shown in Fig.1.3, right panel, namely DANS and Nile Red, are reported in Fig.1.5. Relevant model parameters are listed in Table 1.1. The non-adiabatic fluorescence spectra are calculated similarly, once the fluorescent state is properly singled out. To this aim, we look at the transition dipole moments from the ground state (indeed electronic transitions are more intense than vibrational ones) [88, 94, 93] or rather do some dissipative non-adiabatic dynamics for the optically excited system as it will be described below and recognize the fluorescent state as the quasi-stationary state.

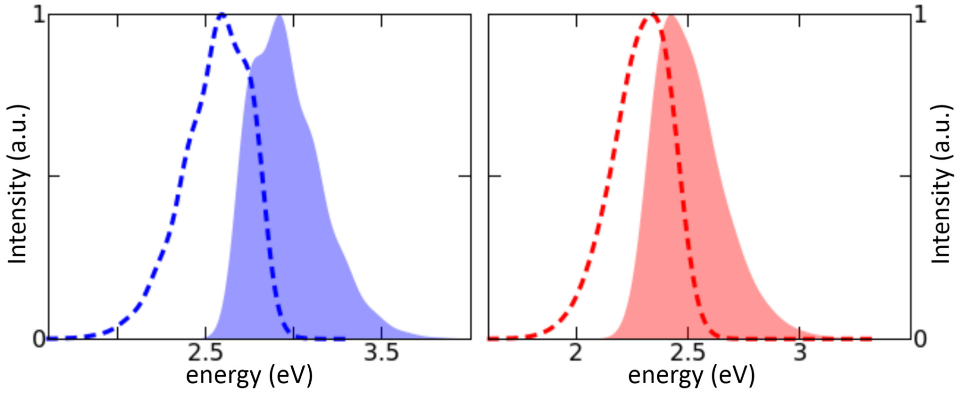

Figure 1.5: Calculated optical absorption (color filled area) and emission (dashed curve) spectra of DANS (left panel) and Nile Red (right panel) accounting for 15 vibrational states and neglecting polar solvation. A Gaussian bandshape, with half width at half maximum (HWHM) equal to 0.09 eV is assigned to each vibronic transition; values of the relevant molecular parameters are reported in Tab.1.1.

	$2z$	τ	ε_v	ω_v
DANS	2.64	0.72	0.3	0.17
Nile Red	1.76	0.95	0.33	0.14

Table 1.1: Essential-state parameters for the two dipolar dyes shown in Fig.1.3, right panel, namely DANS [41] and Nile Red [13]. All the quantities are in eV.

The model in Eq.1.57 can be naturally extended to account for solvation effects.[11, 90, 88, 93] The CT chromophore is assumed to fill a cavity inside the solvent, with the solvent being described as a dielectric continuum medium. The solvent will react to the presence of the polar solute through a reaction field, F_r.[95, 96] In the linear response limit, F_r is proportional to the solute electric dipole moment. The reaction field is described in terms of an electronic and an orientational component, $F_r = F_{el} + F_{or}$. At the equilibrium, the reaction field can thus be written as:

$$F_r = r_{el}\langle\hat{\mu}\rangle + r_{or}\langle\hat{\mu}\rangle, \tag{1.59}$$

where $\langle\hat{\mu}\rangle$ is the expectation value of the electric dipole operator defined in

Eq.1.52, while r_{el} and r_{or} are parameters defined by the solvent properties (mainly the dielectric constant and the refractive index) as well as by the geometry of the cavity filled by the solute.

The electronic component of the reaction field, the only effective contribution in non-polar solvents, is induced by the distortion of the solvent molecules electron density and consequently is a function of the solvent refractive index.[11] F_{el} corresponds to fast degrees of freedom, with typical frequencies falling in the UV region.[11, 97] In the antiadiabatic limit, [98] its effect is limited to a renormalization of the molecular parameters, τ and $2z$.[11] Because of the minor variability of the refractive index among common organic solvents, these renormalized parameters are assumed to be solvent-independent.[90]

In polar solvents the orientational component of the reaction field F_{or} comes into play due to the reorientation of the polar solvent molecules around the solute.[11] F_{or} is associated with slow degrees of freedom, with typical frequencies in the far-IR or microwave regions and can be treated in the adiabatic approximation.[11]

Describing the solvent as a continuum elastic medium, the solvation Hamiltonian can be written as:

$$\hat{H}_{solv} \quad = \quad -\hat{\mu}F_{or} + kF_{or}^2, \tag{1.60}$$

where the quadratic term accounts for the energy spent to create the reaction field and k is a force constant. Using the Hellmann-Feynman theorem, the elastic constant is found by imposing the equilibrium condition:

$$\left\langle \frac{\partial \hat{H}_{solv}}{\partial F_{or}} \right\rangle_{eq} = -\langle\hat{\mu}\rangle + 2kF_{or} = 0, \tag{1.61}$$

where remembering that $F_{or} = \langle\hat{\mu}\rangle r_{or}$, the elastic constant results $k = 1/(2r_{or})$. Consequently, Eq.1.60 can be recast as:[11, 90]

$$\hat{H}_{solv} \quad = \quad -\hat{\mu}F_{or} + \frac{1}{2r_{or}}F_{or}^2. \tag{1.62}$$

According to the solvation model in Eq.1.62, the orientational component of the reaction field is treated as an additional vibrational classical coordinate, whose frequency, ω_{or}, is much lower than the frequency of the molecular internal modes. The solvent vibrational relaxation energy is defined as:[11, 97]

$$\varepsilon_{or} = \frac{\mu_0^2 r_{or}}{2}. \tag{1.63}$$

Non-polar solvents have ε_{or}=0, whereas polar solvents have finite values of ε_{or}. Using Eq.1.63 and collapsing μ_0 into F_{or}, Eq.1.62 becomes:[92]

$$\hat{H}_{solv} = -\hat{\rho} F_{or} + \frac{1}{4\varepsilon_{or}} F_{or}^2, \tag{1.64}$$

where the orientational component of the reaction field has the dimensions of an energy.

For a molecule in a polar solvent the total Hamiltonian is the sum of the Hamiltonian in Eq.1.64 plus the molecular Hamiltonian in Eq.1.57. The total Hamiltonian is diagonalized for different values of F_{or}, thus defining the potential energy curves with respect to the orientational component of the reaction field (Fig.1.6, left panel).[92, 93] In polar solvents, thermal disorder creates a distribution of F_{or} values; as a consequence, the whole solute-solvent system can be described in terms of a canonical Boltzmann distribution of chromophores in equilibrium with the surrounding solvent local configuration (Fig.1.6, left panel).[90, 88] Relevant quantities, like optical spectra (Fig.1.6, right panel), are calculated as ensemble averages, summing on different F_{or} values and weigthing for the relevant Boltzmann distribution.[88, 94, 92] Indeed, the Boltzmann distribution used for absorption and fluorescence spectra is different. Absorption spectra are calculated using the ground state potential energy, while emission spectra are calculated mediating over the F_{or}-dependent energy of the fluorescent state.[93]

The model Hamiltonian in Eq.1.57 can be used for both the energy donor and the energy acceptor, but before facing RET and its dynamics, the dissipative dynamics of a single coherently excited chromophore is discussed.

1.3 Relaxation processes for one molecule

We consider a dipolar chromophore, impulsively excited from the ground state to a coherent state, $|\Psi^*\rangle$. The chromophore is described by the non-adiabatic Hamiltonian in Eq.1.57 and, in the dipole (long wavelength) ap-

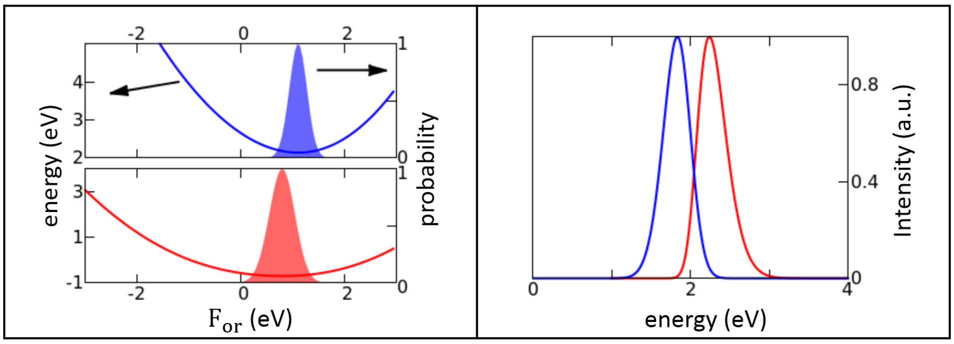

Figure 1.6: Modeling polar solvation. Left panel: potential energy curves as a function of the solvation coordinate calculated for the non-adiabatic DANS fluorescent state (blue curve) and Nile Red ground state (red curve); relevant Boltzmann distributions are superimposed as color filled areas. Calculation done for 5 vibrational states. Right panel: calculated DANS fluorescence (blue line) and Nile Red absorption (red line) optical spectra, accounting for polar solvation. Calculation done for 15 vibrational states. A Gaussian lineshape, with HWHM equal to 0.09 eV is assigned to each vibronic band. Essential-state model parameters are reported in Tab.1.1. Solvent polarity is defined by ε_{or}=0.7 eV. Temperature is set equal to 298 K.

proximation, the light-matter interaction term, $\hat{V}_{LM}(t)$, reads:

$$\hat{V}_{LM}(t) \quad = \quad -\hat{\mu}\vec{E}(t), \tag{1.65}$$

where $\hat{\mu}$ is the electric dipole operator defined in Eq.1.52. The impulsive excitation is described by an electric field: $\vec{E}(t) = \vec{E} \cdot \delta(0)$, where $\delta(0)$ is the Dirac-δ distribution. We assume that only the molecular ground state $|\phi_1\rangle$ is populated at the equilibrium and use the time-dependent perturbation theory to calculate the state after the perturbation as:

$$|\Psi^*(t=0)\rangle \propto \sum_{k=2}^{N} |\phi_k\rangle\langle\phi_k|\hat{\mu}|\phi_1\rangle, \tag{1.66}$$

where the sum runs over all the excited non-adiabatic eigenstates of the system.

For an isolated molecule, not interacting with the environment (i.e., $\hat{H}_I = 0$), the time evolution of the excited coherent state reads:

$$|\Psi^*(t)\rangle = e^{-\frac{i}{\hbar}\hat{H}t}|\Psi^*(0)\rangle \propto \sum_{k=2}^{N} \mu_{k1}|\phi_k\rangle e^{-\frac{i}{\hbar}E_k t}, \tag{1.67}$$

where $\hat{H}$ is the non-adiabatic Hamiltonian defined in Eq.1.57, E_k is the k-th eigenvalue, while $\mu_{k1} = \langle\phi_k|\hat{\mu}|\phi_1\rangle$ is the transition dipole moment. Of course, the total energy of the coherent state is conserved:

$$E^* \quad \propto \quad \sum_{k=2}^{N} |\mu_{k1}|^2 E_k. \tag{1.68}$$

When the coupling with the environment is switched on (i.e., $\hat{H}_I \neq 0$), the dye becomes an open quantum system and its dynamics is more complex since it can exchange energy with the surrounding. The time-evolution of the system will be calculated in the next two Subsections using either the quantum-classical hybrid approach discussed in Subsect.1.1.1 or Redfield equation introduced in Subsect.1.1.2.

1.3.1 Single molecule dynamics within the quantum-classical hybrid approach

Resuming the theory discussed in Subsect.1.1.1, in a quantum-classical hybrid approach the system of interest follows Schrödinger equation (Eq.1.13), while the environment follows either Hamilton's canonical (Eq.1.14) or Langevin stochastic (Eq.1.24) classical equations of motion; moreover, the environment feels the quantum average of the interaction energy in a self-consistent $\mathcal{SB}$ feedback process.

Here the system is a coherently excited dipolar dye, as described above, coupled to a bath described in terms of a chain of 20 classical particles connected by anharmonic springs.[53, 99] The anharmonicity is required to favour the cross-talk among classical degrees of freedom. Specifically, the potential of the classical system reads:

$$V_{\mathcal{B}} = \frac{\hbar\omega_b}{4}\sum_{i=1}^{20}\Big(\xi_i(t)-\xi_{i+1}(t)\Big)^2 + V_0\chi^4\sum_{i=1}^{20}\Big(\xi_i(t)-\xi_{i+1}(t)\Big)^4, \tag{1.69}$$

where ξ_i is the dimensionless coordinate associated with the i-th classical oscillator, ω_b is the bath frequency, V_0 has the dimensions of an energy and χ is the anharmonicity constant. Moreover, we set $\xi_i(t=0)$=0, $\forall$ i=1,..., 20. The first oscillator of the chain interacts with the CT chromophore through a bilinear interaction term:

$$\hat{H}_I(t) = -\beta\hat{Q}\xi_1(t), \tag{1.70}$$

where β is the $\mathcal{SB}$ coupling strength, $\hat{Q}$ is the dimensionless molecular vibrational coordinate and $\xi_1(t)$ is the coordinate associated with the chain oscillator number 1. We adopt fixed boundary conditions, introducing a fixed extra coordinate, $\xi_{21}(t)$=0. Finally the last mobile particle (number 20) is connected to a thermostat (Fig.1.7).

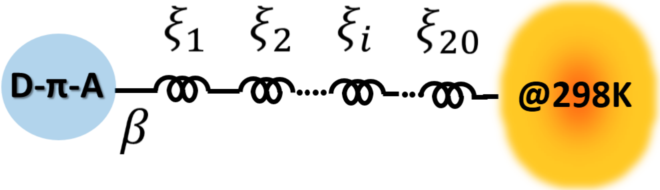

Figure 1.7: Sketch of a CT dipolar chromophore connected to a chain of 20 classical oscillators; the 20-th oscillator is in contact with a thermostat.

Following Eq.1.24, the coordinate associated with the i-th chain oscillator, $\xi_i(t)$, evolves in time according to the equation:

$$\begin{aligned}\frac{\hbar}{2\omega_b}\frac{d^2\xi_i}{dt^2} &= -\frac{\partial V_{\mathcal{B}}}{\partial \xi_i} + \beta\langle\hat{Q}\rangle\delta_{i,1} \\ &+\frac{\hbar}{2\omega_b}\Bigg(-\gamma\frac{d\xi_i}{dt} + 2\zeta\sqrt{\frac{\gamma k_b T\omega_b}{\hbar\Delta t}}\Bigg)\delta_{i,20}, \qquad (1.71)\end{aligned}$$

where the Kronecker delta, $\delta_{i,1}$, guarantees that only the first oscillator of the chain feels the quantum mechanically averaged force generated by the quantum-classical interaction term (Eq.1.15); moreover, the second line introduces thermal fluctuations and dissipation à la Langevin on the last oscillator of the chain, the one located at the maximum distance from the quantum system, to avoid energy flowing back to $\mathcal{S}$ (i.e., to avoid Poincaré recurrence).[53]

We use a time step of 0.06 fs. For each time step, Eq.1.71 is solved for each classical particle using Verlet method.[100, 101] Time-incremented coordinate, $\xi_1(t+\Delta t)$, is introduced into the $\mathcal{SB}$ interaction term in Eq.1.70 and a fourth-order Runge-Kutta algorithm [102] is used to propagate in time the wave function of the quantum system. Iterating these two steps, the mixed quantum-classical trajectory is calculated. Results obtained along these lines are shown in Figs.1.8 and 1.9 as magenta curves (black curves are the corresponding Redfield results discussed in the next Subsection). Specifically, the results are relevant to a dye described by molecular parameters in the first row of Table 1.1, and setting bath parameters as: ω_b=60 cm^{-1}, V_0=1 eV, χ=19. Dissipation and thermal fluctuations are defined by setting γ=1 ps^{-1} and T=298 K, while $\mathcal{SB}$ coupling strength is set to β=0.11 eV. Indeed, all parameters entering Eq.1.71 as well as the length of the chain must be chosen carefully in order to ensure a fast energy flow away from the quantum system.

Looking at panels a, d and e of Fig.1.8, the relaxation dynamics can be divided into two main phases. Initially, a fast internal conversion is observed towards the first vibrational state of the excited electronic state corresponding to the long-lived fluorescent state. Then, a slower relaxation is observed towards the ground state. Coherent oscillations are observed in the early dynamics, as clearly shown in panel b. The Fourier transform of $\langle\hat{Q}(t)\rangle$ has a peak at 0.174 eV, corresponding to a slightly higher frequency than the bare vibrational frequency, ω_v (Tab.1.1), in line with the vibrational

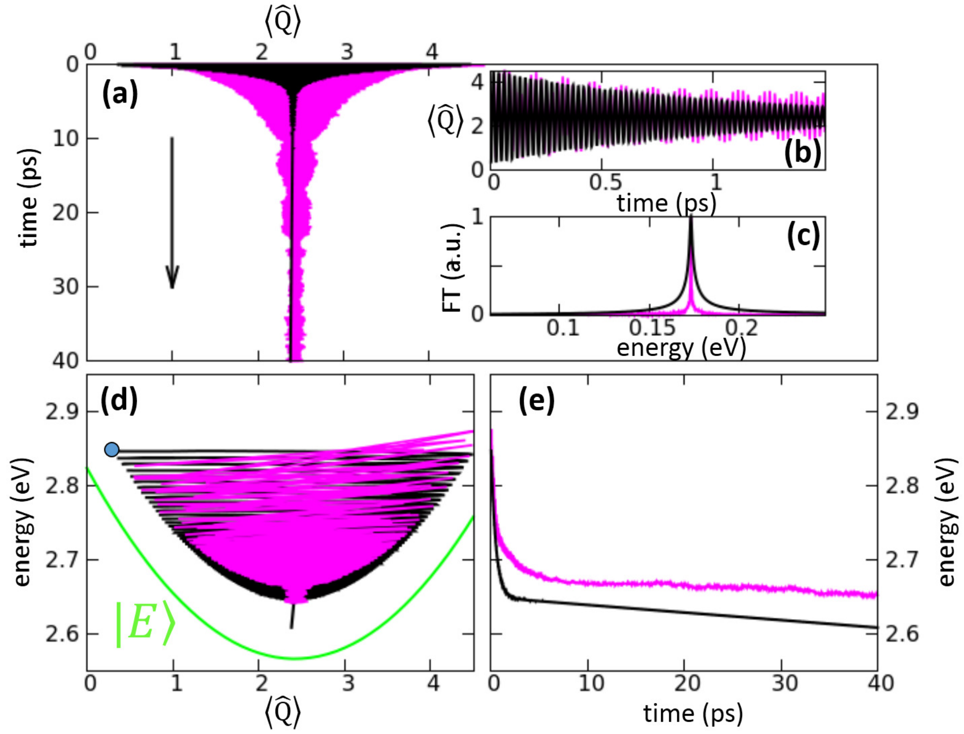

Figure 1.8: Decoherence and energy dissipation in a coherently excited CT dipolar chromophore. Results from quantum-classical hybrid dynamics (averaging 40 trajectories) and Redfield theory are shown as magenta and black curves, respectively. (a-b) Time-evolution of the average value of the molecular coordinate; (c) Fourier transform of the signal in panel b; (d) system energy evolution as a function of the average value of the molecular coordinate; the blue point highlights the evolution starting point. Adiabatic excited state potential energy curve is shown as a green line; (e) Time-dependence of the system energy. Calculations done for the molecular parameters reported in the first line of Table 1.1, as relevant to DANS molecule, and accounting for 15 vibrational states. All the other parameters are defined in the main text.

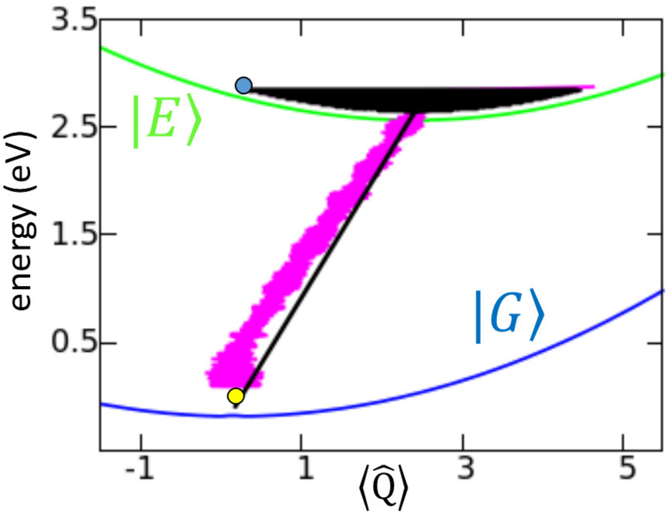

Figure 1.9: Relaxation towards the ground state of a coherently excited CT dipolar chromophore. System energy against the expectation value of the molecular coordinate; blue and yellow points highlight initial and final evolution points, respectively. Dynamics is $\sim$ 7 ns long. Both results from quantum-classical hybrid dynamics (averaging 40 trajectories) and Redfield theory are shown as magenta and black curves, respectively. Same parameters as in Fig.1.8.

hardening expected for the electronic excited state.

As time proceeds, $\mathcal{SB}$ correlations develop and after $\sim$ 1 ps the coherent motion is almost totally washed out, with the system entering an incoherent regime (panels a, b and d); the energy flow towards the bath slows down (panel e) and the system slowly starts relaxing towards the ground state (Fig.1.9).

1.3.2 Single molecule dynamics using Redfield equation

Here, we use the Redfield equation to describe the dynamics of a coherently excited CT dipolar chromophore as influenced by a quantum reservoir. The system is described by the non-adiabatic Hamiltonian in Eq.1.57 and at time zero the reduced density matrix is $\hat{\sigma}(0) = |\Psi^*\rangle\langle\Psi^*|$, where $|\Psi^*\rangle$ is the coherent state defined in Eq.1.66. The bath is described as a collection of quantum mechanical harmonic oscillators, the relevant Hamiltonian being:

$$\hat{H}_{\mathcal{B}} = \sum_i \hbar\omega_i \left(\hat{b}_i^\dagger \hat{b}_i + \frac{1}{2} \right), \tag{1.72}$$

where $\hat{b}_i^\dagger$ and $\hat{b}_i$ are the creation and destruction bosonic operators associated with the i-th bath oscillator, with frequency ω_i.

In analogy with Eq.1.70, the system-bath interaction Hamiltonian is bilinear in the molecular and bath coordinates:

$$\begin{aligned} \hat{H}_I &= \hat{Q} \sum_i g_i \hat{\xi}_i \\ &= \sum_i (g_i \hat{b}_i^\dagger \hat{a} + g_i^* \hat{b}_i \hat{a}^\dagger), \end{aligned} \tag{1.73}$$

where g_i^* is the complex conjugate of the coupling strength between the system and the i-th bath mode, the system bosonic operators $\hat{a}$ and $\hat{a}^\dagger$ being introduced in Eq.1.55.

To describe the dissipative dynamics of the reduced density matrix, we construct Redfield relaxation super-operator as in Eq.1.44. To this end, we evaluate the Fourier-Laplace transforms entering Eq.1.45. Rewriting the integrand in the first line of Eq.1.45 as:

$$\begin{aligned} \langle \hat{H}_{db}^I(0) \hat{H}_{ac}^I(-\tau) \rangle_b &= \sum_{i,i'} \left(g_i g_{i'}^* \langle d|\hat{a}|b\rangle \langle a|\hat{a}^\dagger|c\rangle \langle \hat{b}_i^\dagger \hat{b}_{i'}(-\tau) \rangle_b \right) + \\ &\quad + \sum_{i,i'} \left(g_i^* g_{i'} \langle d|\hat{a}^\dagger|b\rangle \langle a|\hat{a}|c\rangle \langle \hat{b}_i \hat{b}_{i'}^\dagger(-\tau) \rangle_b \right) \end{aligned} \tag{1.74}$$

and plugging this result into the Fourier-Laplace transform, we get:

$$\begin{aligned} \Gamma_{db,ac}^+ &= \frac{\langle d|\hat{a}|b\rangle \langle a|\hat{a}^\dagger|c\rangle}{\hbar^2} \int_0^\infty d\tau e^{-i\omega_{ac}\tau} \sum_{i,i'} \left(g_i g_{i'}^* \langle \hat{b}_i^\dagger(\tau) \hat{b}_{i'} \rangle_b \right) + \\ &\quad + \frac{\langle d|\hat{a}^\dagger|b\rangle \langle a|\hat{a}|c\rangle}{\hbar^2} \int_0^\infty d\tau e^{-i\omega_{ac}\tau} \sum_{i,i'} \left(g_i^* g_{i'} \langle \hat{b}_i(\tau) \hat{b}_{i'}^\dagger \rangle_b \right), \end{aligned} \tag{1.75}$$

where all terms involving the creation (or destruction) of two vibrational excitations are neglected and where the equalities $\langle \hat{b}_i^\dagger \hat{b}_{i'}(-\tau) \rangle_b = \langle \hat{b}_i^\dagger(\tau) \hat{b}_{i'} \rangle_b$ and $\langle \hat{b}_i \hat{b}_{i'}^\dagger(-\tau) \rangle_b = \langle \hat{b}_i(\tau) \hat{b}_{i'}^\dagger \rangle_b$ follow from the smoothness in time of the bath correlation functions;[103] indeed, as mentioned in Subsect.1.1.2, the state of the bath is time-non dependent, that is $[\hat{H}_{\mathcal{B}}, \hat{\rho}_b] = 0$.

After some algebra, the double summation at the first line of Eq.1.75 results:

$$\begin{aligned}\sum_{i,i'} g_i g^*_{i'} \langle \hat{b}^\dagger_i(\tau)\hat{b}_{i'}\rangle_b &= \sum_{i,i'} g_i g^*_{i'} Tr_b\{e^{\frac{i}{\hbar}\hat{H}_{\mathcal{B}}\tau}\hat{b}^\dagger_i e^{-\frac{i}{\hbar}\hat{H}_{\mathcal{B}}\tau}\hat{b}_{i'}\hat{\rho}_b\} \\ &= \sum_i |g_i|^2 e^{i\omega_i\tau}\langle \hat{n}(\omega_i)\rangle_b, \qquad (1.76)\end{aligned}$$

where the bosonic number operator associated with the i-th bath mode, $\hat{n}_i = \hat{b}^\dagger_i\hat{b}_i$, is introduced.

Analogously, for the double summation at the second line of Eq.1.75 one gets:

$$\sum_{i,i'} g^*_i g_{i'} \langle \hat{b}_i(\tau)\hat{b}^\dagger_{i'}\rangle_b = \sum_i |g_i|^2 e^{-i\omega_i\tau}\langle \hat{n}(\omega_i)+1\rangle_b. \qquad (1.77)$$

Introducing a simple form for the bath spectral density, $\mathcal{J}(\omega) = \sum_i |g_i|^2\delta(\omega-\omega_i)$, and using Eqs.1.76 and 1.77, Eq.1.75 can be further manipulated:

$$\begin{aligned}\Gamma^+_{db,ac} &= \frac{\langle d|\hat{a}|b\rangle\langle a|\hat{a}^\dagger|c\rangle}{\hbar^2}\int_0^\infty d\tau e^{-i\omega_{ac}\tau}\int_0^\infty d\omega\mathcal{J}(\omega)e^{i\omega\tau}\langle\hat{n}(\omega)\rangle_b \\ &+\frac{\langle d|\hat{a}^\dagger|b\rangle\langle a|\hat{a}|c\rangle}{\hbar^2}\int_0^\infty d\tau e^{-i\omega_{ac}\tau}\int_0^\infty d\omega\mathcal{J}(\omega)e^{-i\omega\tau}\langle\hat{n}(\omega)+1\rangle_b \\ &= \frac{\langle d|\hat{a}|b\rangle\langle a|\hat{a}^\dagger|c\rangle}{\hbar^2}\int_0^\infty d\omega\mathcal{J}(\omega)\langle\hat{n}(\omega)\rangle_b\int_0^\infty d\tau e^{-i(\omega_{ac}-\omega)\tau} \\ &+\frac{\langle d|\hat{a}^\dagger|b\rangle\langle a|\hat{a}|c\rangle}{\hbar^2}\int_0^\infty d\omega\mathcal{J}(\omega)\langle\hat{n}(\omega)+1\rangle_b\int_0^\infty d\tau e^{-i(\omega-\omega_{ca})\tau} \\ &= \frac{\langle d|\hat{a}|b\rangle\langle a|\hat{a}^\dagger|c\rangle}{\hbar^2}\int_0^\infty d\omega\mathcal{J}(\omega)\langle\hat{n}(\omega)\rangle_b\left[\pi\delta(\omega_{ac}-\omega)-\frac{i}{\omega-\omega_{ac}}\right] \quad (1.78) \\ &+\frac{\langle d|\hat{a}^\dagger|b\rangle\langle a|\hat{a}|c\rangle}{\hbar^2}\int_0^\infty d\omega\mathcal{J}(\omega)\langle\hat{n}(\omega)+1\rangle_b\left[\pi\delta(\omega-\omega_{ca})-\frac{i}{\omega-\omega_{ca}}\right],\end{aligned}$$

showing that the only surviving terms are those with the bath frequency in resonance with the system.

Neglecting the imaginary part of the equation [104] and calculating the frequency domain integrals, one gets:

$$\begin{aligned}\Gamma^+_{db,ac} &= \frac{\langle d|\hat{a}|b\rangle\langle a|\hat{a}^\dagger|c\rangle}{\hbar^2}\pi\mathcal{J}(\omega_{ac})\langle\hat{n}(\omega_{ac})\rangle_b + \\ &+\frac{\langle d|\hat{a}^\dagger|b\rangle\langle a|\hat{a}|c\rangle}{\hbar^2}\pi\mathcal{J}(\omega_{ca})\langle\hat{n}(\omega_{ca})+1\rangle_b, \qquad (1.79)\end{aligned}$$

where $\langle \hat{n}(\omega_{ac}) \rangle_b = (exp[\beta\hbar\omega_{ac}] - 1)^{-1}$ is the Bose-Einstein distribution function.

Assuming that the bath spectral density varies much slower than the Bose-Einstein distribution function, $\mathcal{J}(\omega)$ is put equal to the constant term $\hbar^2\gamma/\pi$, where γ becomes an effective system-bath coupling strength. In this way, Eq.1.79 becomes:

$$\Gamma^{+}_{db,ac} = \gamma\Big(\langle d|\hat{a}|b\rangle\langle a|\hat{a}^{\dagger}|c\rangle\langle \hat{n}(\omega_{ac})\rangle_b + \langle d|\hat{a}^{\dagger}|b\rangle\langle a|\hat{a}|c\rangle\langle \hat{n}(\omega_{ca}) + 1\rangle_b \Big). \quad (1.80)$$

Working in a similar way, the second line of Eq.1.45 can be written as:

$$\Gamma^{-}_{db,ac} = \gamma\Big(\langle d|\hat{a}|b\rangle\langle a|\hat{a}^{\dagger}|c\rangle\langle \hat{n}(\omega_{bd})\rangle_b + \langle d|\hat{a}^{\dagger}|b\rangle\langle a|\hat{a}|c\rangle\langle \hat{n}(\omega_{db}) + 1\rangle_b \Big). \quad (1.81)$$

The derived expressions for $\Gamma^{+}_{db,ac}$ and $\Gamma^{-}_{db,ac}$ describe an exchange of vibrational quanta between the system and the bath; more precisely, the reservoir can either absorb or emit one phonon from/to the system as long as the energy is conserved (Fig.1.10). To this end, the correct ordering of the indices entering Eqs.1.80 and 1.81 is fundamental, since a wrong order would lead to a violation of the detailed balance condition with the system not approaching the correct canonical equilibrium state.

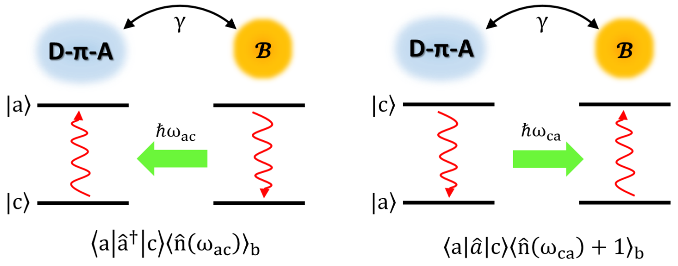

Figure 1.10: Sketch of the two processes described by $\Gamma^{+}_{db,ac}$ in Eq.1.80; on the left, the reservoir emits one vibrational quantum that is absorbed by the system and viceversa on the right. System and bath are coupled by the γ constant (see main text).

Redfield relaxation super-operator is a four-index tensor with N^4 elements, where N is the dimension of the system Hamiltonian; consequently, one can use Eqs.1.80 and 1.81 to calculate on the fly all $R_{ab,cd}$ elements entering Eq.1.43, with no need to store the whole relaxation super-operator in the computer memory, but only the system bosonic creation and destruction operators. Furthermore, the $O(N^4)$ multiplications required for a super-operator acting on a matrix are reduced to $O(N^3)$ operations as required for a matrix-matrix multiplication.[78] In this work, we solve Redfield equation using the Short-Iterative-Arnoldi algorithm (see Appendix B).

Results reported in Figs.1.8 and 1.9 as black curves are obtained solving Redfield equation (with Δt=1 fs as time step) for the coherently excited CT chromophore interacting with the harmonic quantum bath at 298 K. The system-bath coupling strength, γ, is set equal to 1 ps^{-1}, while the relevant molecular parameters are reported in Tab.1.1, first line.

The first (qualitative) difference with respect to the quantum-classical hybrid results shown as magenta lines in Figs.1.8 and 1.9 is that the time trajectory obtained using Redfield dynamics does not present random noise, having no stochastic term entering it. Indeed, the quantum-classical results were obtained by averaging over several (typically 40) Langevin different trajectories in order to reduce the noise, while a single trajectory is enough for the Redfield approach. Apart from this qualitative difference, the quantitative details of the calculated dynamics strongly depend on the specific adopted sets of parameters. As already mentioned in Subsect.1.3.1, in the quantum-classical hybrid approach the classical bath frequency, anharmonicity, thermal fluctuations and dimension (i.e., the number of classical oscillators) as well as the $\mathcal{SB}$ coupling, have to be carefully tuned in order to describe truly dissipative phenomena, with no energy flowing back to the quantum system. In the Redfield equation, the single parameter modeling dissipation, i.e. the effective $\mathcal{SB}$ coupling strength γ, was set in order to match quantum-classical hybrid results. In particular, the two different time regimes already observed within the quantum-classical hybrid approach are well reproduced; exchanging vibrational quanta with the bath, the system rapidly reaches the first vibrational state of the electronic excited state (panels d and e) and then starts its slow path towards the electronic ground state (Fig.1.9). The early-stage coherent motion (panel b) is analyzed through its Fourier transform (panel c) which shows a single peak centered at 0.174 eV, thus reproducing the quantum-classical hybrid result. The system-bath correlations wash the coherent motion out within the first ~2-3 ps (panel a). Having reproduced with the Redfield approach the main results of the quantum-classical dynamical calculation, we have not attempted further fine tuning of the hybrid approach parameters for a more detailed match.

Solving Redfield equation of motion can be rather time consuming. Indeed, the $O(N^3)$ scalar multiplications required by Eq.1.43 can be easily parallelized on modern multi-core memory-shared machines (for example, by means of the *OpenMP* routines); moreover, the secular approximation discussed at the end of Subsect.1.1.2 is typically assumed in order to drastically reduce the number of relevant $R_{ab,cd}$ relaxation components entering calculations. In this sense, the Bloch model can be even more attractive, since only the populations require numerical evaluation of Eq.1.46 (see Appendix C). However, if several non-secular terms enter the dynamics, the Bloch model as well as the secular approximation may lead to wrong results.[78, 80, 81]

Results obtained within Redfield equation and the Bloch model are reported in Fig.1.11; the system is the coherently excited dipolar chromophore already studied in Figs.1.8 and 1.9. By removing all non-secular terms and keeping the $R_{aa,cc}$ and $R_{ab,ab}$ relaxation tensor components only, the Bloch model only describes population transfer and coherence relaxation phenomena. Consequently, the faster decay of the excited state coherence observed in panel a for the Bloch model respect to the Redfield approach is hardly surprising; indeed, Redfield equation can count on other processes that can make coherence stronger, namely populations changing into coherences ($R_{aa,cd}$) as well as coherence transfer ($R_{ab,cd}$). Moreover, the early-time oscillations superimposed to the time-evolution of the system energy and of some populations (panels b and d) are completely lost using the Bloch model (panels c and e), this being a clear signature of the population-coherence coupling. Once the coherences are relaxed, the effect of population-coherence coupling becomes negligible and the long-term dynamics is properly described by both Bloch model and Redfield equation of motion.

Having become familiar with the quantum-classical hybrid approach and with Redfield equation on a single molecule, the following Section is devoted to the real-time simulation of the RET phenomenon between two interacting CT dipolar chromophores.

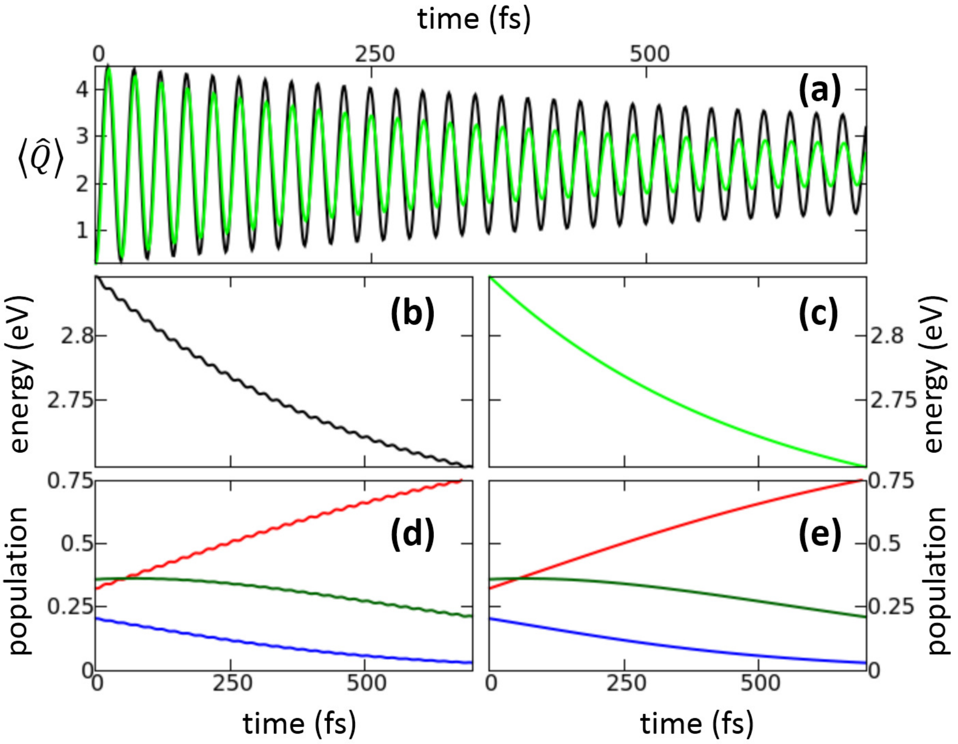

Figure 1.11: Signatures of population-coherence coupling. (a) Time-dependence of the average value of the molecular coordinate calculated in the Redfield approach (black curve) and the Bloch model (green curve). (b-c) Time-evolution of the system energy using Redfield equation and the Bloch model, respectively. (d-e) $\sigma_{16,16}(t)$ (red curve), $\sigma_{17,17}(t)$ (dark-green curve), $\sigma_{18,18}(t)$ (blue curve), as relevant to the initially mainly populated states, using Redfield equation and the Bloch model, respectively. Calculations done considering 15 vibrational states. Same parameters as in Fig.1.8.

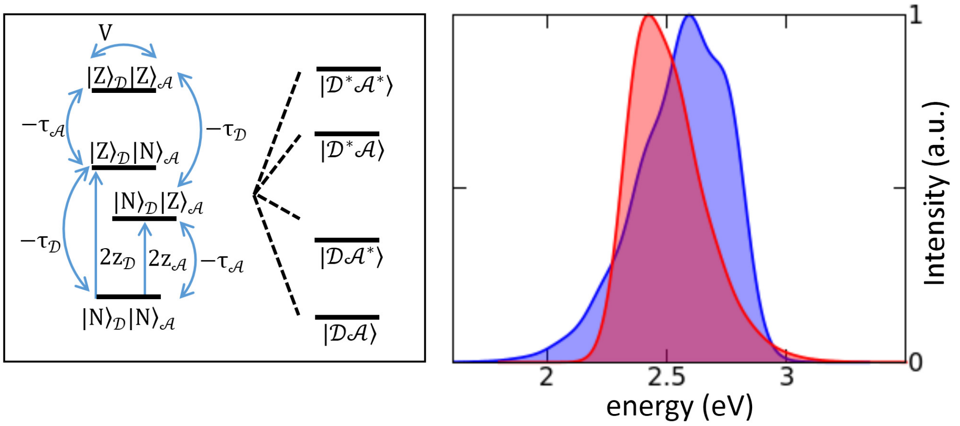

Figure 1.12: Setting the stage for RET. Left panel: sketch of the four-states model used to describe two interacting D-π-A molecules. Right panel: non-adiabatic DANS emission (blue filled curve) and Nile Red absorption (red filled curve) spectra; calculation done on the two isolated molecules accounting for 15 vibrational states and neglecting the effect of polar solvation. A Gaussian bandshape, with half width at half maximum (HWHM) equal to 0.09 eV is assigned to each vibronic transition. Relevant molecular parameters are reported in Tab.1.1.

1.4 RET: a non-adiabatic dynamical perspective

We now consider RET between an energy donor, $\mathcal{D}$, and an energy acceptor, $\mathcal{A}$, both described as polar dyes, using the two-state model in Eq.1.48.

The diabatic basis states for the RET pair are the direct product of the basis states of the isolated dyes:

$$\begin{aligned} |N_{\mathcal{D}}N_{\mathcal{A}}\rangle &= |N\rangle_{\mathcal{D}} \otimes |N\rangle_{\mathcal{A}}, \\ |Z_{\mathcal{D}}N_{\mathcal{A}}\rangle &= |Z\rangle_{\mathcal{D}} \otimes |N\rangle_{\mathcal{A}}, \\ |N_{\mathcal{D}}Z_{\mathcal{A}}\rangle &= |N\rangle_{\mathcal{D}} \otimes |Z\rangle_{\mathcal{A}}, \\ |Z_{\mathcal{D}}Z_{\mathcal{A}}\rangle &= |Z\rangle_{\mathcal{D}} \otimes |Z\rangle_{\mathcal{A}}, \end{aligned} \tag{1.82}$$

where $|N\rangle_{\mathcal{D}(\mathcal{A})}$ is the neutral state of the energy donor (energy acceptor), while $|Z\rangle_{\mathcal{D}(\mathcal{A})}$ is the relevant zwitterionic state. The electronic Hamiltonian can be written as the sum of the two single-molecule Hamiltonians plus a small coupling term, accounting for the electrostatic interaction between the two molecules in the zwitterionic state (V):

$$\hat{H}_{el}^{\mathcal{DA}} = \begin{pmatrix} 0 & -\tau_{\mathcal{D}} & -\tau_{\mathcal{A}} & 0 \\ -\tau_{\mathcal{D}} & 2z_{\mathcal{D}} & 0 & -\tau_{\mathcal{A}} \\ -\tau_{\mathcal{A}} & 0 & 2z_{\mathcal{A}} & -\tau_{\mathcal{D}} \\ 0 & -\tau_{\mathcal{A}} & -\tau_{\mathcal{D}} & 2z_{\mathcal{D}} + 2z_{\mathcal{A}} + V \end{pmatrix}, \tag{1.83}$$

where $2z_{\mathcal{D}}$ and $2z_{\mathcal{A}}$ are the energies associated with the energy donor and energy acceptor zwitterionic states, respectively, while $\tau_{\mathcal{D}}$ and $\tau_{\mathcal{A}}$ are the relevant CT integrals (Fig.1.12, left panel). In this work the energy donor-energy acceptor interaction energy is set equal to 0.08 eV. Numerical diagonalization of $\hat{H}_{el}^{\mathcal{DA}}$ leads to the perturbed states $|\mathcal{DA}\rangle$, $|\mathcal{DA}^*\rangle$, $|\mathcal{D}^*\mathcal{A}\rangle$, $|\mathcal{D}^*\mathcal{A}^*\rangle$, where the star is used for the excited species (Fig.1.12, left panel).

A dimensionless coordinate and its conjugated momentum can be associated with both the energy donor and the energy acceptor in order to linearly modulate their excitation energy. Neglecting nuclear motion (i.e. adopting the adiabatic approximation), the electronic problem is diagonalized for different molecular geometries, thus getting the Potential Energy Surfaces, PES (Fig.1.13).

However, in order to treat the electronic and nuclear degrees of freedom on the same footing, quantum coordinate, $\hat{Q}_{\mathcal{D}(\mathcal{A})} = (\hat{a}^{\dagger}_{\mathcal{D}(\mathcal{A})} + \hat{a}_{\mathcal{D}(\mathcal{A})})$ and its conjugated momentum, $\hat{P}_{\mathcal{D}(\mathcal{A})} = i(\hat{a}^{\dagger}_{\mathcal{D}(\mathcal{A})} - \hat{a}_{\mathcal{D}(\mathcal{A})})$ are introduced; consequently, the donor-acceptor non-adiabatic Hamiltonian can be written as:

$$\begin{aligned} \hat{H}_{\mathcal{DA}} = {} & \hat{H}_{el}^{\mathcal{DA}} + \\ & -\sqrt{\hbar\omega_v^{\mathcal{D}}\varepsilon_{\mathcal{D}}}(\hat{a}^{\dagger}_{\mathcal{D}} + \hat{a}_{\mathcal{D}})|Z_{\mathcal{D}}N_{\mathcal{A}}\rangle\langle Z_{\mathcal{D}}N_{\mathcal{A}}| + \\ & -\sqrt{\hbar\omega_v^{\mathcal{A}}\varepsilon_{\mathcal{A}}}(\hat{a}^{\dagger}_{\mathcal{A}} + \hat{a}_{\mathcal{A}})|N_{\mathcal{D}}Z_{\mathcal{A}}\rangle\langle N_{\mathcal{D}}Z_{\mathcal{A}}| + \\ & -\sqrt{\hbar\omega_v^{\mathcal{D}}\varepsilon_{\mathcal{D}}}(\hat{a}^{\dagger}_{\mathcal{D}} + \hat{a}_{\mathcal{D}})|Z_{\mathcal{D}}Z_{\mathcal{A}}\rangle\langle Z_{\mathcal{D}}Z_{\mathcal{A}}| + \\ & -\sqrt{\hbar\omega_v^{\mathcal{A}}\varepsilon_{\mathcal{A}}}(\hat{a}^{\dagger}_{\mathcal{A}} + \hat{a}_{\mathcal{A}})|Z_{\mathcal{D}}Z_{\mathcal{A}}\rangle\langle Z_{\mathcal{D}}Z_{\mathcal{A}}| + \\ & +\hbar\omega_v^{\mathcal{D}}\left(\hat{a}^{\dagger}_{\mathcal{D}}\hat{a}_{\mathcal{D}} + \frac{1}{2}\right) + \hbar\omega_v^{\mathcal{A}}\left(\hat{a}^{\dagger}_{\mathcal{A}}\hat{a}_{\mathcal{A}} + \frac{1}{2}\right), \end{aligned} \tag{1.84}$$

where $\omega_v^{\mathcal{D}}$ and $\omega_v^{\mathcal{A}}$ are the vibrational frequencies associated with $\hat{Q}_{\mathcal{D}}$ and $\hat{Q}_{\mathcal{A}}$, respectively, whereas $\varepsilon_{\mathcal{D}}$ and $\varepsilon_{\mathcal{A}}$ are the relevant vibrational relaxation energies. Adopting the strategy discussed in Sect.1.2.1, Eq.1.84 is written

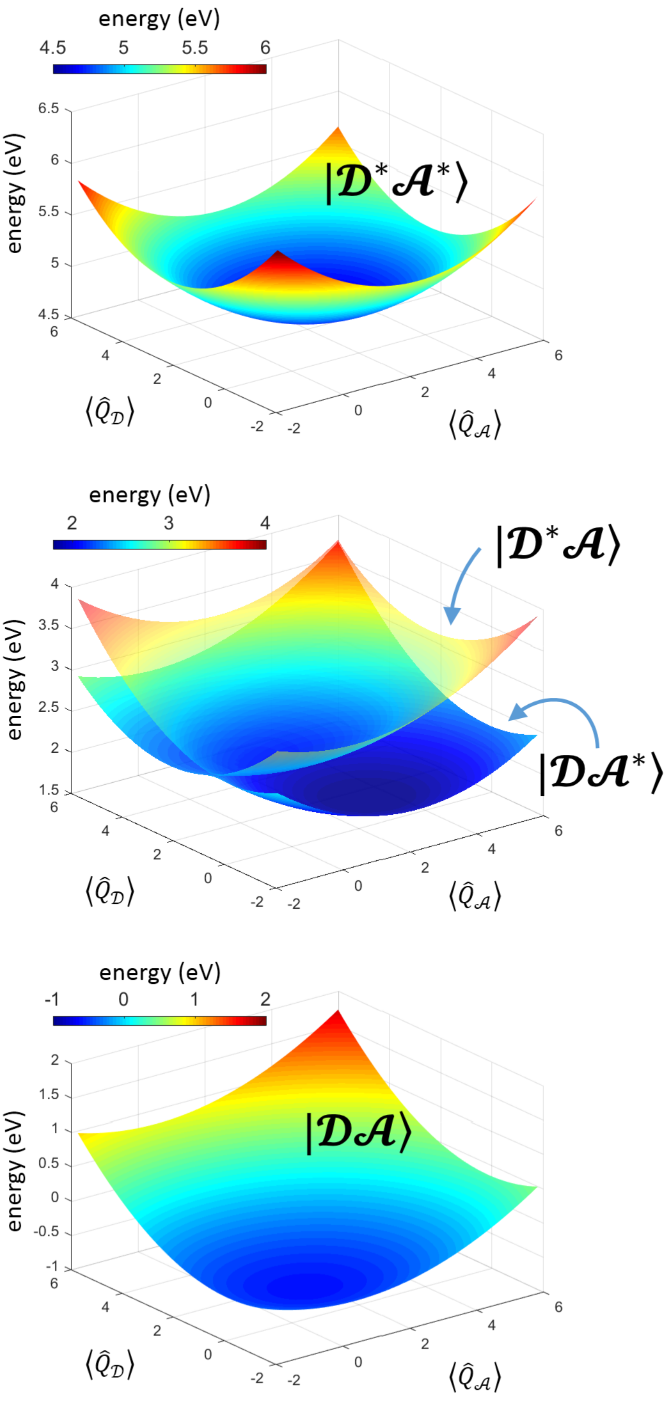

Figure 1.13: Adiabatic Potential Energy Surfaces (PES) calculated for the energy donor-energy acceptor system (V=0.08 eV). Parameters used are reported in Tab.1.1.

on the non-adiabatic vector space defined as the direct product of $\mathcal{DA}$ 4-fold Hilbert space, $\mathcal{H}_{\mathcal{DA}}$, times the two Fock spaces, $\mathcal{F}$ and $\mathcal{F}$', associated with the molecular coordinates:

$$\begin{aligned} \mathcal{V}_{NA}^{\mathcal{DA}} &= \mathcal{H}_{\mathcal{DA}} \otimes \mathcal{F} \otimes \mathcal{F}' \\ &= \mathcal{H}_{\mathcal{DA}} \otimes \left(\bigoplus_{i=0}^{\infty} \mathcal{F}^i \right) \otimes \left(\bigoplus_{i=0}^{\infty} \mathcal{F}^i \right)'. \end{aligned} \tag{1.85}$$

In order to make the problem numerically tractable and to reach convergence on properties of interest, the two Fock spaces are truncated in order to have 16 vibrational excitations at the most. As a result, the non-adiabatic Hamiltonian is a 544×544 sparse matrix.

All parameters entering Eq.1.84 are reported in Tab.1.1, with DANS molecule acting as the energy donor towards Nile Red, the energy acceptor. The spectral overlap between DANS emission and Nile Red absorption is shown in Fig.1.12, right panel.

A coherent excitation drives DANS out of equilibrium; therefore, in order to describe the transfer of the excitation energy from DANS to Nile Red, relaxation phenomena must be accounted for and to this end, the coupling of the system to the environment is required. In the following two Subsections, DANS-Nile Red coupled dissipative dynamics is studied using the quantum-classical hybrid approach (Subsect.1.4.1) and Redfield equation for the system reduced density matrix (Subsect.1.4.2).

1.4.1 RET: quantum-classical hybrid approach

Following the quantum-classical hybrid approach adopted for a single molecule in Subsect.1.3.1, the energy donor and the energy acceptor are coupled to a reservoir described as a chain of classical anharmonic oscillators; more precisely, 10 classical particles connected through anharmonic springs are used for the energy-donor, whereas 20 particles are linked to the energy acceptor. The longer chain used for the energy acceptor is instrumental in avoiding recurrence. The relevant reservoir potential functions are defined as:

$$\begin{aligned} V_{\mathcal{D}}^{\mathcal{B}} &= \frac{\hbar\omega_b}{4} \sum_{i=1}^{10} \Big(\xi_i(t) - \xi_{i+1}(t) \Big)^2 + V_0 \chi^4 \sum_{i=1}^{10} \Big(\xi_i(t) - \xi_{i+1}(t) \Big)^4, \\ V_{\mathcal{A}}^{\mathcal{B}} &= \frac{\hbar\omega_b'}{4} \sum_{i=1}^{20} \Big(\xi_i'(t) - \xi_{i+1}'(t) \Big)^2 + V_0' \chi'^4 \sum_{i=1}^{20} \Big(\xi_i'(t) - \xi_{i+1}'(t) \Big)^4 \end{aligned} \tag{1.86}$$

where ξ_i is the dimensionless coordinate associated with the i-th classical oscillator, ω_b is the relevant vibrational frequency, while $V_0\chi^4$ defines the anharmonicity strength; unprimed quantities refer to the energy donor, whereas primed ones are used for the energy acceptor. We set $\xi_i(t=0)$=0, $\forall$ i=1,..., 10 and $\xi'_i(t=0)$=0, $\forall$ i=1,..., 20. Fixed boundary conditions are adopted linking the last oscillator of both chains to a static extracoordinate, namely $\xi_{11}(t)$=0 and $\xi'_{21}(t)$=0.

In analogy to Eq.1.70, the coupling between each reservoir and the relevant quantum system is modeled as a term bilinear in the quantum and the classical coordinates; the interaction Hamiltonian thus reads:

$$\hat{H}_I(t) \quad = \quad -\beta\hat{Q}_{\mathcal{D}}\xi_1(t) - \beta'\hat{Q}_{\mathcal{A}}\xi'_1(t), \tag{1.87}$$

where β and β' are the system-bath interaction strengths, while $\xi_1(t)$ and $\xi'_1(t)$ are the coordinates of the first oscillator of each chain. As sketched in Fig.1.14, the last oscillator of both chains is connected to a thermostat.

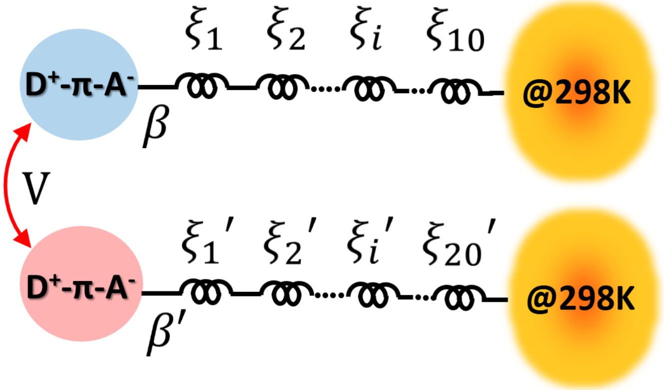

Figure 1.14: Sketch of the energy donor-energy acceptor system connected to two different classical oscillator chains. The last oscillator of each chain is in contact with a thermostat. The RET partners are described in terms of two CT dipolar chromophores, interacting with the interaction energy, V.

The classical bath coordinates evolve in time according to the equations:

$$\begin{aligned}\frac{\hbar}{2\omega_b}\frac{d^2\xi_i}{dt^2} \quad &= \quad -\frac{\partial V_{\mathcal{D}}^{\mathcal{B}}}{\partial\xi_i} + \beta\langle\hat{Q}_{\mathcal{D}}\rangle\delta_{i,1} \\ &\quad + \frac{\hbar}{2\omega_b}\left(-\gamma\frac{d\xi_i}{dt} + 2\zeta\sqrt{\frac{\gamma k_b T\omega_b}{\hbar\Delta t}}\right)\delta_{i,10},\end{aligned} \tag{1.88}$$

$$\begin{aligned}\frac{\hbar}{2\omega_b'}\frac{d^2\xi_i'}{dt^2} &= -\frac{\partial V_{\mathcal{A}}^{\mathcal{B}}}{\partial \xi_i'} + \beta'\langle \hat{Q}_{\mathcal{A}}\rangle\delta_{i,1} \\ &\quad + \frac{\hbar}{2\omega_b'}\left(-\gamma'\frac{d\xi_i'}{dt} + 2\zeta'\sqrt{\frac{\gamma' k_b T\omega_b'}{\hbar\Delta t}}\right)\delta_{i,20}, \end{aligned} \tag{1.89}$$

where the first and the second equations are related to the classical chain of the energy donor and of the energy acceptor, respectively. In order to describe energy dissipation and thermal fluctuations, the relevant static friction coefficients, γ and γ', are introduced together with two uncorrelated Gaussian random numbers (with zero mean and unit width), ζ and ζ'.

At each time-step, Verlet algorithm is used to evolve all the classical coordinates; newly obtained $\xi_1(t+\Delta t)$ and $\xi_1'(t+\Delta t)$ are put into Eq.1.87 and fourth-order Runge-Kutta algorithm is used to propagate in time the energy donor-energy acceptor total wave function. The same time-step, Δt=0.09 fs, is used for both classical and quantum dynamics.

In Fig.1.15, quantum-classical hybrid results for the energy donor-energy acceptor couple are shown as magenta curves (black curves represent Redfield results and they will be discussed in the next Subsection) and are obtained for ω_b=ω_b'=60 cm^{-1}, V_0=V_0'=1 eV, χ=32, χ'=4, β=0.28 eV, β'=0.1 eV, γ=γ'=5 fs^{-1}, averaging 40 different Langevin trajectories.

At time zero, a coherent state is created on the energy donor; consequently, the system starts evolving, the average value of the donor coordinate, $\langle \hat{Q}_{\mathcal{D}}\rangle$, clearly showing coherent oscillations (panel c and its inset). The relevant Fourier transform peaks at 0.173 eV (panel d), being the vibrational energy relevant to the $|\mathcal{D}^*\mathcal{A}\rangle$ potential energy surface. On the contrary, no early-stage dynamics is observed looking at the expectation value of the acceptor coordinate, $\langle \hat{Q}_{\mathcal{A}}\rangle$ (inset in panel e).

The interaction with the environment rapidly destroys the coherence (panel c), while the system relaxes to the lowest vibrational state of the donor electronic excited state (panels a and b). After ~1 ps, the energy starts flowing to the energy acceptor, the average value of $\hat{Q}_{\mathcal{A}}$ showing an overall displacement together with very weak oscillations (panel e); the relevant Fourier transform (panel f) peaks at ~0.14 eV, being the vibrational energy associated with the energy acceptor excited PES.

This view is further confirmed looking at the time evolution of state populations in Fig.1.16, left panel; initially, the excitation is mainly localized

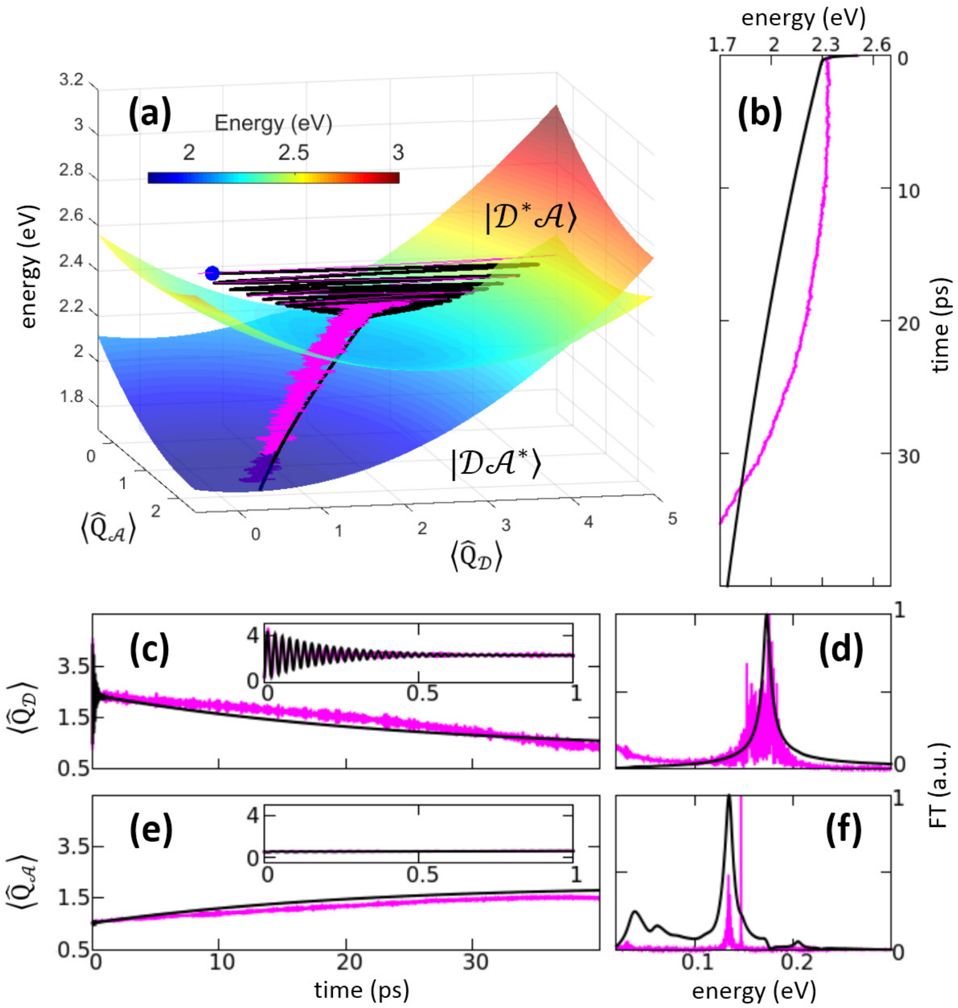

Figure 1.15: Energy transfer between CT dipolar chromophores. Results from the quantum-classical hybrid approach and Redfield equation are shown as magenta and black curves, respectively. (a) System energy evolution as a function of energy donor and energy acceptor coordinates; the blue dot marks the starting point of the time-evolution. Adiabatic PES's relevant to $|\mathcal{D}^*\mathcal{A}\rangle$ and $|\mathcal{D}\mathcal{A}^*\rangle$ are also shown; (b) System energy as a function of time; (c) Expectation value of the energy donor coordinate as a function of time. The inset shows an enlargement of the early-stage dynamics. (d) Fourier transform of the signal in panel c; (e) Average value of the energy acceptor coordinate as a function of time. The inset is an enlargement of the early-time dynamics; (f) Fourier transform of the signal in panel e. Calculations done for the molecular parameters shown in Tab.1.1, where DANS is the energy donor and Nile Red the energy acceptor. The maximum number of vibrational excitations is set to 16. Other parameters are defined in the main text.

on the energy donor and after ∼ 1 ps, population slowly starts flowing towards the excited energy acceptor; after ∼ 27.5 ps, the excitation is mainly localized on the energy acceptor.

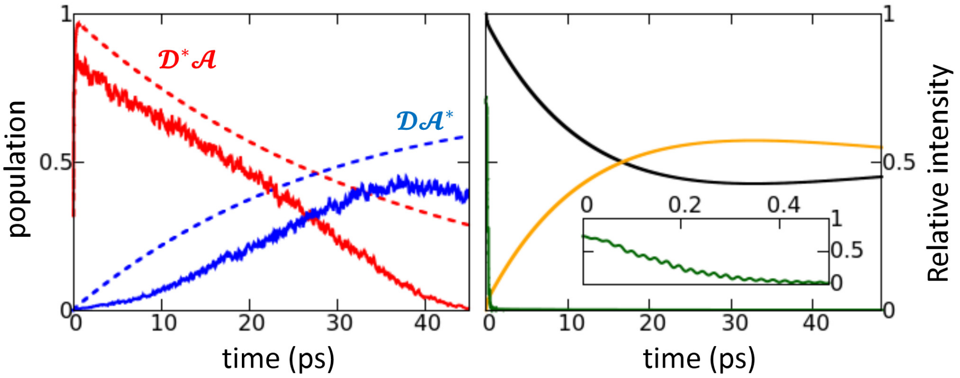

Figure 1.16: Energy transfer between CT dipolar chromophores. Left panel: time evolution of the populations of the two states mostly involved in the RET process, namely state number 143 (red lines) and state number 130 (blue lines) using the quantum-classical hybrid approach (continuous lines) and the full Redfield equation (dashed lines). Right panel: time dependency of purity (black line), linear entropy (orange line) and coherence (dark-green line) using full Redfield equation; the inset is an enlargement of the early-stage time-dependency of coherence. Calculations done imposing a maximum number of 16 vibrational excitations. Same model parameters used in Fig.1.15.

1.4.2 RET: Redfield equation

Following the approach adopted for a single molecule in Subsect.1.3.2, a bath of quantum harmonic oscillators is coupled to the system; the classical bath coordinates introduced in the previous Subsection now become quantum operators:

$$\xi_i, \xi_i' \rightarrow \hat{\xi}_i = (\hat{b}_i^\dagger + \hat{b}_i), \tag{1.90}$$

where, unlike the previous Subsection, both the energy donor and the energy acceptor are assumed to interact with the same environment.

The interaction Hamiltonian is written as:

$$\begin{aligned}\hat{H}_I &= (\hat{Q}_{\mathcal{D}} + \hat{Q}_{\mathcal{A}}) \sum_i g_i \hat{\xi}_i \\ &= \sum_i \Big[g_i \hat{b}_i^\dagger (\hat{a}_{\mathcal{D}} + \hat{a}_{\mathcal{A}}) + g_i^* \hat{b}_i (\hat{a}_{\mathcal{D}}^\dagger + \hat{a}_{\mathcal{A}}^\dagger) \Big], \qquad (1.91)\end{aligned}$$

where g_i^* is the complex conjugate of the system-bath interaction strength.

Following the steps discussed in Sect.1.3.2, Redfield relaxation tensor component is obtained:

$$\begin{aligned}\Gamma^{+}_{db,ac} &= \gamma \Big[\langle d|\hat{a}_{\mathcal{D}}|b\rangle\langle a|\hat{a}_{\mathcal{D}}^\dagger|c\rangle\langle \hat{n}(\omega_{ac})\rangle_b + \langle d|\hat{a}_{\mathcal{D}}^\dagger|b\rangle\langle a|\hat{a}_{\mathcal{D}}|c\rangle\langle \hat{n}(\omega_{ca})+1\rangle_b \\ &+ \langle d|\hat{a}_{\mathcal{A}}|b\rangle\langle a|\hat{a}_{\mathcal{A}}^\dagger|c\rangle\langle \hat{n}(\omega_{ac})\rangle_b + \langle d|\hat{a}_{\mathcal{A}}^\dagger|b\rangle\langle a|\hat{a}_{\mathcal{A}}|c\rangle\langle \hat{n}(\omega_{ca})+1\rangle_b \\ &+ \langle d|\hat{a}_{\mathcal{D}}|b\rangle\langle a|\hat{a}_{\mathcal{A}}^\dagger|c\rangle\langle \hat{n}(\omega_{ac})\rangle_b + \langle d|\hat{a}_{\mathcal{D}}^\dagger|b\rangle\langle a|\hat{a}_{\mathcal{A}}|c\rangle\langle \hat{n}(\omega_{ca})+1\rangle_b \\ &+ \langle d|\hat{a}_{\mathcal{A}}|b\rangle\langle a|\hat{a}_{\mathcal{D}}^\dagger|c\rangle\langle \hat{n}(\omega_{ac})\rangle_b + \langle d|\hat{a}_{\mathcal{A}}^\dagger|b\rangle\langle a|\hat{a}_{\mathcal{D}}|c\rangle\langle \hat{n}(\omega_{ca})+1\rangle_b \Big],\end{aligned}$$

where the system creation and annihilation operators are written on $\hat{H}_{\mathcal{DA}}$ non-adiabatic eigenstates. For the sake of simplicity, the system-bath coupling strength, γ, is assumed to be the same for both the energy donor and the energy acceptor. All terms containing $\langle \hat{n}(\omega_{ca})+1\rangle_b$, i.e. the Bose-Einstein distribution increased by one, describe system emission of one vibrational quantum that is absorbed by the bath. All other terms describe the system absorption of one phonon that is emitted by the reservoir (Fig.1.17). Furthermore, the complementary component, $\Gamma^{-}_{db,ac}$, reads:

$$\begin{aligned}\Gamma^{-}_{db,ac} &= \gamma \Big[\langle d|\hat{a}_{\mathcal{D}}|b\rangle\langle a|\hat{a}_{\mathcal{D}}^\dagger|c\rangle\langle \hat{n}(\omega_{bd})\rangle_b + \langle d|\hat{a}_{\mathcal{D}}^\dagger|b\rangle\langle a|\hat{a}_{\mathcal{D}}|c\rangle\langle \hat{n}(\omega_{db})+1\rangle_b \\ &+ \langle d|\hat{a}_{\mathcal{A}}|b\rangle\langle a|\hat{a}_{\mathcal{A}}^\dagger|c\rangle\langle \hat{n}(\omega_{bd})\rangle_b + \langle d|\hat{a}_{\mathcal{A}}^\dagger|b\rangle\langle a|\hat{a}_{\mathcal{A}}|c\rangle\langle \hat{n}(\omega_{db})+1\rangle_b \\ &+ \langle d|\hat{a}_{\mathcal{D}}|b\rangle\langle a|\hat{a}_{\mathcal{A}}^\dagger|c\rangle\langle \hat{n}(\omega_{bd})\rangle_b + \langle d|\hat{a}_{\mathcal{D}}^\dagger|b\rangle\langle a|\hat{a}_{\mathcal{A}}|c\rangle\langle \hat{n}(\omega_{db})+1\rangle_b \\ &+ \langle d|\hat{a}_{\mathcal{A}}|b\rangle\langle a|\hat{a}_{\mathcal{D}}^\dagger|c\rangle\langle \hat{n}(\omega_{bd})\rangle_b + \langle d|\hat{a}_{\mathcal{A}}^\dagger|b\rangle\langle a|\hat{a}_{\mathcal{D}}|c\rangle\langle \hat{n}(\omega_{db})+1\rangle_b \Big].\end{aligned}$$

Plugging these expressions into Eq.1.44, Redfield dissipative dynamics can be calculated for the RET pair. Results obtained with a time step Δt=1.5 fs and a system-bath coupling constant γ=5 ps^{-1}, are shown in Fig.1.15 as black curves.

In order to help the discussion, some auxiliary quantities can be defined, namely the purity, the linear entropy and the coherence.[81] The purity of a quantum state is defined as:

$$p(t) = Tr\{\hat{\sigma}^2(t)\}, \qquad (1.92)$$

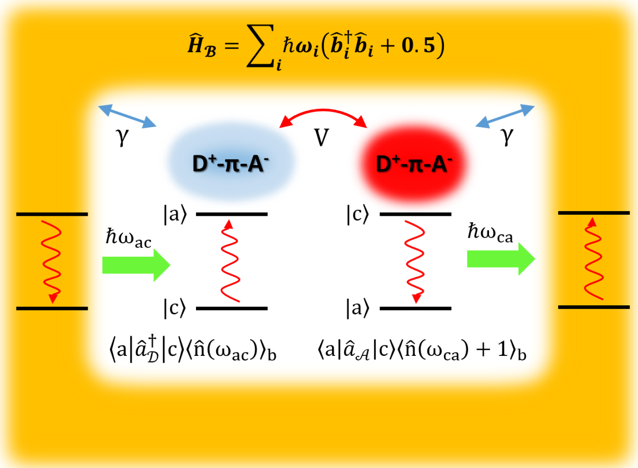

Figure 1.17: Sketch of two possible processes described by $\Gamma^{+}_{db,ac}$. Blue halo is used for the energy donor, red halo is used for the energy acceptor, orange halo is used for the environment. On the left, a vibrational quantum is emitted by the reservoir and it is absorbed by the energy donor; on the right, the reservoir absorbs one phonon emitted by the energy acceptor.

where $p \in [\frac{1}{N}, 1]$, with $p = 1/N$ for a completely mixed state and $p = 1$ for a pure state. Linear entropy, $S_l(t)$, represents another measure of the purity of a quantum state, being defined as:

$$S_l(t) = Tr\{\hat{\sigma}(t) - \hat{\sigma}^2(t)\} = 1 - Tr\{\hat{\sigma}^2(t)\} = 1 - p(t), \tag{1.93}$$

where $S_l \in [0, 1 - \frac{1}{N}]$; consequently, S_l=0 for a pure quantum state. Finally, the coherence of the quantum state can be defined as:

$$C(t) \;\;=\;\; p(t) - \sum_i \sigma^2_{ii}(t). \tag{1.94}$$

In Fig.1.16, right panel, time-dependency of these three quantities is shown as relevant to the energy donor-energy acceptor dynamics shown in Fig.1.15.

The coherent perturbation prepares the energy donor in a pure state, with no entropy and coherence equal to ∼0.72. As time proceeds, the energy donor starts being entangled with the environment, the coherence oscillating behaviour (with vibrational energy equal to 0.173 eV) rapidly goes to zero (see the inset in the right panel in Fig.1.16) and the linear entropy increases;

the system is relaxing towards the first vibrational state of the $|\mathcal{D}^*\mathcal{A}\rangle$ Potential Energy Surface. After ∼33 ps, purity reaches a minimum and then starts growing again; the excitation energy is now mainly localized on the energy acceptor and relaxation of the system towards the first vibrational state of the $|\mathcal{D}\mathcal{A}^*\rangle$ Potential Energy Surface starts. This analysis is further confirmed by the time-evolution of the relevant populations in Fig.1.16, left panel.

One last note concerning the numerical implementation is in order. As mentioned at the end of Sect.1.4, the dimension of the two Fock spaces associated with the two molecular coordinates is truncated in order to describe 16 vibrational excitations at the most; this ensures convergence of properties of interest and makes the dimension of the system as large as 544; consequently, solving Redfield equation (Eq.1.43) requires $O(544^3)$ scalar multiplications for each time step. However, some approximations can be adopted in order to speed the calculations up.

At time zero the reduced density matrix is prepared in a coherent state and, as time proceeds, the system relaxes. As a consequence, those states that are too high in energy respect to the coherent state will never see their population growing and can be safely neglected.

As already observed in Fig.1.11, the secular approximation and the Bloch model are expected to fail in describing the early-stage dynamics of the coherent state, where population-coherence as well as coherence-coherence transfer phenomena are of great importance. Moreover, the presence of two vibrational modes in the model in Eq.1.84 leads to several quasi-degenerate states and to several non-secular components. Consequently, neither the Bloch model nor the secular approximation can be used. In these conditions, the computationally expensive full Redfield equation is approximated by the pseudo non-secular algorithm [81] described at the end of Subsect.1.1.2, keeping only those $R_{ab,cd}$ non-secular terms that satisfy the condition $|\omega_{ab} - \omega_{cd}| \leq \alpha$, where α is a fixed threshold.

In Fig.1.18, results obtained for the energy donor-energy acceptor system using full Redfield equation, the pseudo non-secular algorithm (with α=0.01 eV) and the Bloch model are shown. In the upper panel, the coherent oscillations of the molecular coordinate obtained within the Bloch model damp faster than those calculated using full Redfield equation and ruinously diverge after ∼200 fs. Indeed, the divergence is fixed accounting for the most important non-secular terms; using the pseudo non-secular algorithm with α=0.01 eV, thus accounting for the 0.006% of the total relaxation super-operator, results well match those obtained using full Redfield equation; moreover, moving to α=0.2 eV, thus accounting for the 0.12% of the full relaxation tensor, the early-time oscillations of the system energy (lower panel) are also perfectly reproduced (results for α=0.2 eV completely overlap full Redfield results and are not shown). Being a good compromise between physical accuracy and computational efficiency, the pseudo non-secular approach with α=0.01 eV was used to obtain Redfield results shown in Fig.1.15.

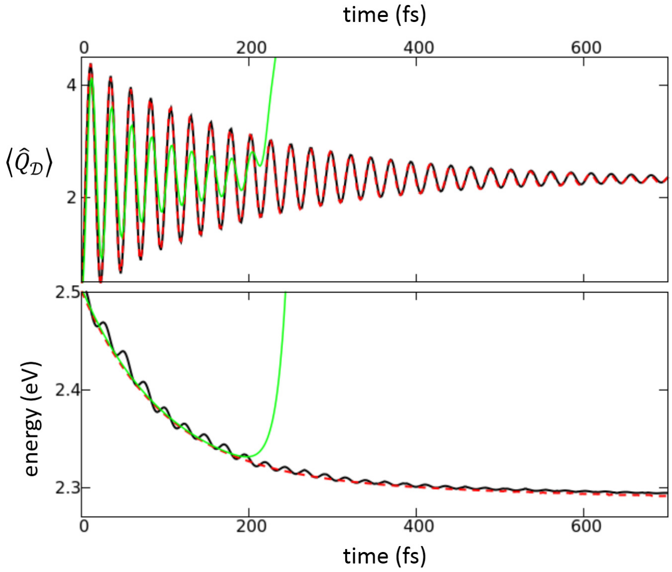

Figure 1.18: The prominent role of non-secular terms in the multicomponent energy donor-energy acceptor system. Early-stage dynamics of $\langle \hat{Q}_{\mathcal{D}} \rangle$ (upper panel) and of the system energy (lower panel). Continuous black curve: results from full Redfield equation; dashed red curve: results from the pseudo non-secular algorithm with α=0.01 eV; continuous green curve: results from the Bloch model. Calculations done accounting for 16 vibrational excitations at the most. Same model parameters used in Fig.1.15.

1.5 The effect of polar solvent

Once the coherent state on the energy donor has been created, internal conversion leads to vibrational relaxation within few hundreds of femtoseconds. In polar solvents, the solvent relaxation dynamics is typically much slower and starts once the vibrational degrees of freedom are fully relaxed. The solvent reaches the excited-state distribution after a few picoseconds and, depending on the relative velocity of the processes, the energy transfer to the acceptor may occur after the solvent relaxation (slow RET) or during the solvent relaxation (fast RET).[105, 106] In order to fully describe solvent effects on RET, a dynamical calculation accounting for both system and solvent degrees of freedom is required. Leaving this to a future work, the present discussion is focused on just two limits, namely the limit of frozen solvent and that of fast solvent.

If the solvent relaxation time, τ_s, is introduced, then the limit of frozen solvent corresponds to $\tau_{RET} \ll \tau_s$. Within this limit, RET occurs with a rate that reflects the average ground state solvent distribution. Consequently, this limit is successfully described within Förster model. On the contrary, if the solvent relaxation is fast (i.e., $\tau_s \rightarrow 0$), then the solvation degrees of freedom rapidly rearrange in response to the fields generated by the excited state dipole of the donor and the ground state dipole of the acceptor; consequently, the solvent distribution is calculated on the donor excited state and the acceptor ground state potential energy curves in Fig.1.6, left panel. In this limit, the fastest channels dominate the RET process, Förster theory breaks down and a theoretical description based on density matrix (like Redfield equation) can be used.

In a RET system, two reaction fields must be introduced, as relevant to the energy donor and to the energy acceptor, as follows:

$$\hat{H}_{solv}^{\mathcal{DA}} = -\hat{\rho}_{\mathcal{D}} F_{or}^{\mathcal{D}} - \hat{\rho}_{\mathcal{A}} F_{or}^{\mathcal{A}} + \frac{1}{4\varepsilon_{or}} \left(F_{or}^{\mathcal{D}} \right)^2 + \frac{1}{4\varepsilon_{or}} \left(F_{or}^{\mathcal{A}} \right)^2, \qquad (1.95)$$

where $\hat{\rho}_{\mathcal{D}(\mathcal{A})}$ is the ionicity operator associated with the energy donor (energy acceptor), while ε_{or} is the solvent orientational relaxation energy, that is set equal for the two species for the sake of simplicity. Summing Eq.1.95 to the non-adiabatic Hamiltonian in Eq.1.84, the solute-solvent interaction is described in terms of a $F_{or}^{\mathcal{D}(\mathcal{A})}$-linearly dependent electronic energy $2z$, that is $2z\left(F_{or}^{\mathcal{D}(\mathcal{A})}\right) = 2z_{\mathcal{D}(\mathcal{A})} - F_{or}^{\mathcal{D}(\mathcal{A})}$. Consequently, both the degree of CT, $\rho_{\mathcal{D}(\mathcal{A})}$, in Eq.1.50, and the CT transition energy, $\Delta\mathcal{E}_{CT}^{\mathcal{D}(\mathcal{A})}$, in Eq.1.51, become $F_{or}^{\mathcal{D}(\mathcal{A})}$-dependent functions.

Here, using full Redfield equation (Eq.1.43), RET process is studied in the limit of fast solvent. As observed in Fig.1.15, panel e, the energy acceptor vibrational coordinate shows no appreciable displacement and the relevant vibrational relaxation energy, $\varepsilon_{\mathcal{A}}$, can be safely set equal to zero; consequently, the electronic parameter $2z_{\mathcal{A}}$ is renormalized to 0.88 eV in order to have proper spectral overlap between the energy donor emission and energy acceptor absorption spectral bands.

It is useful to define the acceptor population operator, $\hat{A}$, as:[76, 77]

$$\hat{A} \;=\; |\mathcal{A}^*\rangle\langle\mathcal{A}^*|, \tag{1.96}$$

where, remembering Eq.1.49, the energy acceptor excited state reads:

$$|\mathcal{A}^*\rangle \;=\; -\sqrt{\rho(F_{or}^{\mathcal{A}})}|N\rangle_{\mathcal{A}} + \sqrt{1-\rho(F_{or}^{\mathcal{A}})}|Z\rangle_{\mathcal{A}}. \tag{1.97}$$

Consequently, Eq.1.96 can be rewritten in matrix form as:

$$\hat{A} = \begin{pmatrix} \rho(F_{or}^{\mathcal{A}}) & 0 & u & 0 \\ 0 & \rho(F_{or}^{\mathcal{A}}) & 0 & u \\ u & 0 & 1-\rho(F_{or}^{\mathcal{A}}) & 0 \\ 0 & u & 0 & 1-\rho(F_{or}^{\mathcal{A}}) \end{pmatrix}, \tag{1.98}$$

where $u = -\sqrt{\rho(F_{or}^{\mathcal{A}})(1-\rho(F_{or}^{\mathcal{A}}))}$ and $\rho(F_{or}^{\mathcal{A}}) = \rho(2z(F_{or}^{\mathcal{A}}))$. The time-dependent population probability of the state $|\mathcal{A}^*\rangle$ is further defined as:

$$P_{\mathcal{A}^*}(t) \;=\; Tr\{\hat{\sigma}(t)\hat{A}\}. \tag{1.99}$$

We follow the RET progress by monitoring the evolution of $P_{\mathcal{A}^*}(t)$.

Figure 1.19, right panel, shows the population dynamics of the acceptor excited state calculated for five different points in the $F_{or}^{\mathcal{D}^*}$, $F_{or}^{\mathcal{A}}$ reaction field grid (left panel). The complementary quantity relevant to the energy donor, $P_{\mathcal{D}^*}(t)$, is obtained as $1 - P_{\mathcal{A}^*}(t)$ and is not shown.

The velocity as well as the nature of RET drastically change in the different points in the grid. For example, setting $F_{or}^{\mathcal{D}^*}$=0.87 eV and $F_{or}^{\mathcal{A}}$=0.49 eV, as relevant to the magenta dot in the reaction field grid, the energy is

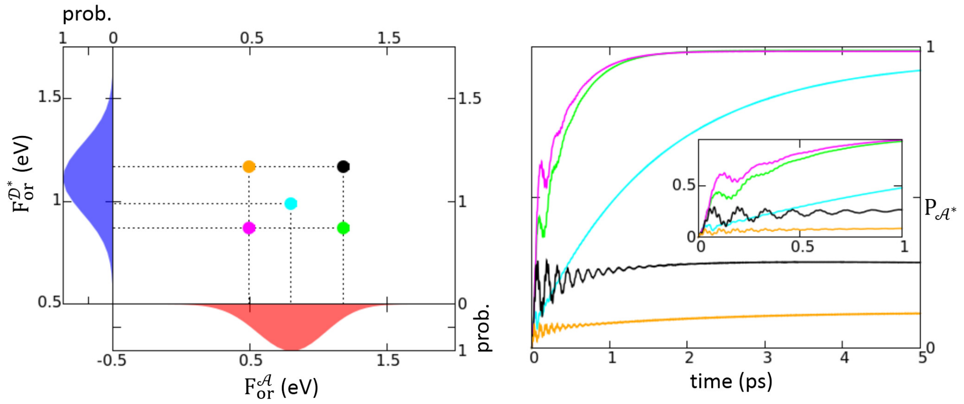

Figure 1.19: Polar solvation influencing RET dynamics. Left panel: $F_{or}^{\mathcal{D}^*}$, $F_{or}^{\mathcal{A}}$ reaction field grid together with the relevant Boltzmann distributions (see Fig.1.6, left panel); Right panel: time dependence of $P_{\mathcal{A}^*}$ calculated using full Redfield equation for five different points in the $F_{or}^{\mathcal{D}^*}$, $F_{or}^{\mathcal{A}}$ grid. The line color matches the relevant dot color in the grid. The inset shows an enlargement of the first 1 ps dynamics. Calculation done accounting for 15 vibrational states, setting $\varepsilon_{\mathcal{A}}$=0 and $2z_{\mathcal{A}}$=0.88 eV. Other molecular parameters are reported in Tab.1.1, while γ=10 ps^{-1}, ε_{or}=0.7 eV and T=298 K. Integration time step, Δt=1 fs.

completely transferred to the acceptor after ~2 ps. However, the electronic coherences, clearly visible as $P_{\mathcal{A}^*}$ low-frequency oscillations superimposed to high-frequency (vibrational) ones, [77] show how the excitation energy is initially bouncing more than three times (see the enlargement in the right panel) between the energy donor and the energy acceptor. The frequency of the electronic oscillations is ~0.023 eV and is connected to the energy donor-energy acceptor interaction energy, V;[77] high-frequency oscillations are induced by the energy donor vibrational coordinate and peaks at 0.174 eV. Increasing the $F_{or}^{\mathcal{D}^*}$ to 1.17 eV, while keeping $F_{or}^{\mathcal{A}}$=0.49 eV (orange dot in the grid), makes RET slower, with the acceptor population ~0.1 after 5 ps. Furthermore, $P_{\mathcal{A}^*}$ motion is electronically incoherent, low-frequency oscillations being almost completely washed out (see also the enlargement in the right panel).

1.6 Conclusions

In this Chapter, two fully dynamical approaches to Resonance Energy Transfer were presented. In Sect.1.3, a coherently excited CT dipolar chromophore was coupled to the environment. The relevant dissipative dynamics was attacked both through a quantum-classical hybrid approach in Subsect.1.3.1 and using Redfield equation in Subsect.1.3.2, obtaining comparable results (see Figs.1.8 and 1.9). Within the hybrid approach, the driven non-adiabatic system was coupled to a bath of classical anharmonic oscillators connected to a thermostat and a numerical integration of the coupled quantum-classical equations of motion defined hybrid dissipative trajectories. On the other hand, using the reduced density matrix formalism and connecting the system to a quantum environment, Redfield equation described the system dissipative dynamics with no explicit treatment of the bath degrees of freedom.

In Sect.1.4, two interacting CT dipolar chromophores coupled to the environment were used to simulate RET in the time-domain. The initially coherent motion of the driven energy donor was rapidly washed out by the growing system-environment correlations and excitation energy was incoherently transferred to the energy acceptor. Results obtained within the quantum-classical hybrid approach well compared with those obtained using Redfield equation (Fig.1.15).

Preliminary results on the effect of polar solvation on RET dynamics are presented in Sect.1.5. Considering the limit of fast solvation and using Redfield equation, the polar solvent influenced the velocity as well as the vibronic coherent nature of the RET process. In the future, this work will be extended to properly discuss the coupled solute-solvent dissipative dynamics and its effects on RET.

Appendix A

Proof of Eq.1.37

Here we want to verify the relation reported in Eq.1.37:

$$\mathcal{P}\mathcal{L}_I e^{-\frac{i}{\hbar}\mathcal{Q}(\mathcal{L}_\mathcal{S}+\mathcal{L}_\mathcal{B})\mathcal{Q}\tau}\mathcal{L}_I \quad = \quad \mathcal{P}\mathcal{L}_I e^{-\frac{i}{\hbar}(\mathcal{L}_\mathcal{S}+\mathcal{L}_\mathcal{B})\tau}\mathcal{L}_I. \tag{A.1}$$

Using Eqs.1.31 and 1.33, the following equalities can be written:

$$\mathcal{Q}\mathcal{L}_\mathcal{S}\mathcal{Q} = \mathcal{Q}\mathcal{L}_\mathcal{S}, \quad \mathcal{Q}\mathcal{L}_\mathcal{B}\mathcal{Q} = \mathcal{Q}\mathcal{L}_\mathcal{B}. \tag{A.2}$$

Consequently, the left-hand side of Eq.A.1 can be recast as:

$$\mathcal{P}\mathcal{L}_I e^{-\frac{i}{\hbar}\mathcal{Q}(\mathcal{L}_\mathcal{S}+\mathcal{L}_\mathcal{B})\mathcal{Q}\tau}\mathcal{L}_I \quad = \quad \mathcal{P}\mathcal{L}_I e^{-\frac{i}{\hbar}\mathcal{Q}(\mathcal{L}_\mathcal{S}+\mathcal{L}_\mathcal{B})\tau}\mathcal{L}_I. \tag{A.3}$$

Defining $\mathcal{L}_0 = \mathcal{L}_\mathcal{S} + \mathcal{L}_\mathcal{B}$ and taking the exponential power series expansion of the right-hand side of Eq.A.3, we get:

$$\mathcal{P}\mathcal{L}_I e^{-\frac{i}{\hbar}\mathcal{Q}\mathcal{L}_0\tau}\mathcal{L}_I \quad = \quad \mathcal{P}\mathcal{L}_I\left[1 - \frac{i}{\hbar}\mathcal{Q}\mathcal{L}_0\tau + \frac{1}{2}\left(\frac{i}{\hbar}\right)^2\mathcal{Q}\mathcal{L}_0^2\tau^2 + ...\right]\mathcal{L}_I, \tag{A.4}$$

where we used the idempotency of the projection super-operator, $\mathcal{Q}^2 = \mathcal{Q}$.

Using $\mathcal{Q} = 1 - \mathcal{P}$ (Eq.1.31) and remembering that $\mathcal{P}\mathcal{L}_I\mathcal{P}$=0 (Eq.1.34), Eq.A.4 becomes:

$$\begin{aligned}\mathcal{P}\mathcal{L}_I e^{-\frac{i}{\hbar}\mathcal{Q}\mathcal{L}_0\tau}\mathcal{L}_I \quad &= \quad \mathcal{P}\mathcal{L}_I\left[1 - \frac{i}{\hbar}\mathcal{L}_0\tau + \frac{1}{2}\left(\frac{i}{\hbar}\right)^2\mathcal{L}_0^2\tau^2 + ...\right]\mathcal{L}_I \\ &= \quad \mathcal{P}\mathcal{L}_I e^{-\frac{i}{\hbar}\mathcal{L}_0\tau}\mathcal{L}_I.\end{aligned} \tag{A.5}$$

Appendix B

Short-Iterative-Arnoldi algorithm

The $\hat{\sigma}(t)$ time-evolution is obtained through integration of Eq.1.43. If N is the dimension of the relevant basis, one has to solve a system of N^2 coupled linear differential equations. To this end, it is useful to move to Liouville space, where conventional matrices become N^2-long vectors (to do this, matrices can be row-wise turned into a single vector) and super-operators become $N^2 \times N^2$ matrices. Along these lines, Eq.1.43 can be rewritten in the Liouville space as:

$$\frac{d}{dt}|\sigma(t)\rangle\rangle \quad = \quad \hat{\mathcal{L}}\ |\sigma(t)\rangle\rangle, \tag{B.1}$$

where the Liouvillian generic matrix element reads:[78]

$$\mathcal{L}_{i,j} \quad = \quad -i\omega_{i,j}\delta_{i,j} + R_{i,j}, \quad \forall\ i,j = 1, ..., N^2 \tag{B.2}$$

and $\delta_{i,j}$ is Kronecker delta symbol defined in Liouville space.

Working in the Liouville space, we use the Dirac-type double-bracket notation for conventional matrices and we put the hat on conventional super-operators. As a result, Eq.B.1 is isomorphous with the time-dependent Schrödinger equation and all the numerical techniques commonly used to integrate the latter can be used to solve the former.

The formal solution of Eq.B.1 is:

$$|\sigma(t)\rangle\rangle \quad = \quad e^{\hat{\mathcal{L}}t}|\sigma(0)\rangle\rangle. \tag{B.3}$$

Diagonalizing the Liouvillian, Eq. B.3 can be recast as:

$$|\sigma(t)\rangle\rangle \quad = \quad \hat{U} e^{\hat{\Lambda} t} \hat{U}^{-1} |\sigma(0)\rangle\rangle, \tag{B.4}$$

where $\hat{\Lambda}$ is the diagonalized Liouvillian and $\hat{U}$ is the eigenvector matrix.

Full diagonalization of the Liouvillian $N^2 \times N^2$ matrix can be avoided using the Short-Iterative-Arnoldi (SIA) method, a generalization of the Lanczos algorithm for the case of asymmetric matrices. In the SIA method, a n-dimensional Krylov space, spanned by the orthonormal basis $\{|\sigma\rangle\rangle, \hat{\mathcal{L}}|\sigma\rangle\rangle, ..., \hat{\mathcal{L}}^{n-1}|\sigma\rangle\rangle\}$, is built in order to evaluate $|\sigma(t+\Delta t)\rangle\rangle \simeq exp(\hat{\mathcal{L}}\Delta t)|\sigma(t)\rangle\rangle$. In this work, a fresh Krylov space is built at each time step (its typical dimension being 20).

The building-up process of Krylov space $\{|\rho_j\rangle\rangle; j = 0, ..., n-1\}$ starts normalizing $|\sigma(t)\rangle\rangle$:

$$|\rho_0\rangle\rangle \quad \equiv \quad \frac{|\sigma(t)\rangle\rangle}{\sqrt{\langle\langle\sigma(t)|\sigma(t)\rangle\rangle}}, \tag{B.5}$$

where $\sqrt{\langle\langle\sigma(t)|\sigma(t)\rangle\rangle} \equiv \sqrt{Tr(\hat{\sigma}(t)^\dagger \hat{\sigma}(t))}$ is the Frobenius norm of the system reduced density matrix, $||\ |\sigma(t)\rangle\rangle\ ||_F$. Then the following steps are recursively repeated $n-1$ times:[78, 107]

$$\begin{aligned}
|\rho'_j\rangle\rangle &= \hat{\mathcal{L}}|\rho_j\rangle\rangle; \\
h_{i,j} &= \langle\langle\rho_i|\rho'_j\rangle\rangle, \ i = 0, ..., j; \\
|\rho''_j\rangle\rangle &= |\rho'_j\rangle\rangle - \sum_{i=0}^{j} h_{i,j}|\rho_i\rangle\rangle; \\
h_{j+1,j} &= \sqrt{\langle\langle\rho''_j|\rho''_j\rangle\rangle}; \\
|\rho_{j+1}\rangle\rangle &= \frac{|\rho''_j\rangle\rangle}{h_{j+1,j}},
\end{aligned}$$

where $\hat{h} = \hat{V}^\dagger \hat{\mathcal{L}} \hat{V}$ ($\hat{V}$ contains in its columns Krylov basis vectors, $|\rho_j\rangle\rangle$) is an upper Hessenberg matrix, thus making easier solving the eigenvalue problem $\hat{h}\hat{W} = \hat{W}\hat{\Lambda}$.

Finally, the time-evolved $|\sigma(t)\rangle\rangle$ is calculated as:

$$\begin{aligned}
|\sigma(t+\Delta t)\rangle\rangle &\simeq \hat{V} e^{\hat{h}\Delta t} \hat{V}^\dagger |\rho_0\rangle\rangle \\
&\simeq \hat{V}(\hat{W} e^{\hat{\Lambda}\Delta t} \hat{W}^{-1})(\hat{V}^\dagger |\rho_0\rangle\rangle) \\
&\simeq \sum_{i=0}^{n-1} |\rho_i\rangle\rangle c_i(t), \qquad \text{(B.6)}
\end{aligned}$$

where

$$c_i(t) \equiv \sqrt{\langle\langle\sigma(t)|\sigma(t)\rangle\rangle}(\hat{W}e^{\hat{\Lambda}\Delta t}\hat{W}^{-1})\langle\langle\rho_i|\rho_0\rangle\rangle. \qquad \text{(B.7)}$$

Appendix C

Solving the Pauli master equation

Within the Bloch model, populations dynamics is totally decoupled from the coherences dynamics and only the former needs to be numerically evaluated. The equation of motion governing populations dynamics is the Pauli master equation (Eq.1.46). The Pauli master equation can be rewritten in a simple vector-matrix form:

$$\frac{d}{dt}p_a(t) \quad = \quad \sum_c r_{a,c} p_c(t), \tag{C.1}$$

where a shorthand notation for the reduced density matrix populations, $p_a = \sigma_{aa}$, and for the relaxation super-operator elements, $r_{a,c} = R_{aa,cc}$, are introduced. Consequently, Eq.C.1 is an ordinary differential equation:

$$\frac{d}{dt}\vec{p}(t) = r\ \vec{p}(t), \tag{C.2}$$

where $\vec{p}(t)$ is the N-dimensional vector containing the reduced density matrix populations and r is the $N \times N$ matrix containing the relaxation super-operator terms governing the transfer of populations.

The solution of Eq.C.2 is of the form:

$$\vec{p}(t) \quad = \quad \sum_{i=1}^{N} \left(c_i \vec{v}_i e^{\lambda_i t} \right), \tag{C.3}$$

where c_i is a constant and λ_i is the eigenvalue associated with the i-th r matrix eigenvector, $\vec{v}_i$. As a result, if r is time non-dependent, within the

Bloch model populations can be propagated in time diagonalizing just once the r matrix and calculating the c_i constants on the basis of the initial conditions.

Chapter 2

Electron transfer and emergent phenomena

In this Chapter, a new family of molecular materials is proposed, based on the interplay of intra- and intermolecular electron transfers. Charge Transfer (CT) governs the physics of the so-called CT crystals, where strongly correlated electrons are delocalized on soft lattices.[108, 109, 48, 31] These materials show a huge variety of phenomena ranging from multistability and phase transitions [110] to structural and electronic instabilities, [111] to charge-ordering, [112] etc. As far as conductivity properties are concerned, CT crystals span the whole range of possibilities, going from insulators and semiconductors to metals and superconductors.[19, 20] Ferroelectricity has been proved and it is largely studied in different families of insulating CT crystals.[113, 21, 114]

On the other hand, Intramolecular Electron Transfer (IET) [11, 12, 13, 88, 28, 14, 115] is of crucial importance for different families of chromophores (Sect.1.2) and conjugated polymers used within organic light emitting diodes (OLED), organic and hybrid solar cells as well as in biomedical imaging, nanofabrication, etc.[116, 117, 118, 119, 120, 121, 122] The huge sensitivity of these systems to external stimuli (mainly light and temperature) and to the surrounding medium (like the solvent polarity) reflects their large non-linear response and can be used in order to induce the intriguing phenomenon of multistability.[123, 124, 125, 126]

A careful molecular and supramolecular design of molecular materials showing both CT and IET degrees of freedom is fundamental in order to reach new functionalities and applications. Recently, [125, 126, 127] a new CT chromophore was synthesized, with the electron donor group (D) being TTF (tetrathiafulvalene) and the electron acceptor group (A) being the PTM (polychlorotriphenylmethyl) radical ($R^\bullet$); the two moieties are connected through a vinylene π-bridge, thus leading to a D-π-$R^\bullet$ molecular structure (Fig.2.1). The conjugation offered by the π-bridge is poor

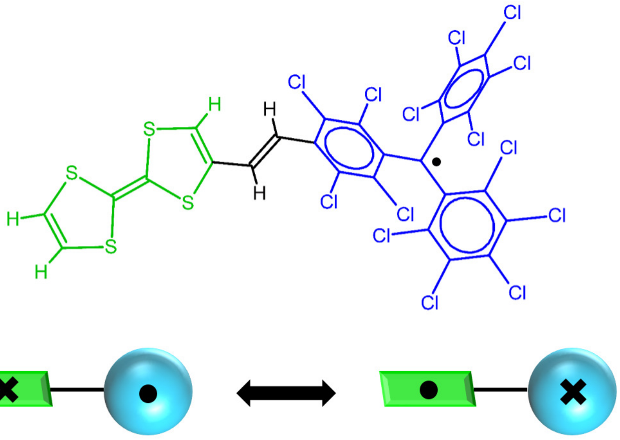

$$D - \pi - R^\bullet \leftrightarrow D^{+\bullet} - \pi - R^-$$

Figure 2.1: Molecular structure of the tetrathiafulvalene-polychlorotriphenylmethyl radical, TTF-PTM, CT dipolar chromophore and sketch of its two main resonance structures. Dot represents an unpaired electron, whereas cross stands for the double occupation.

and the system shows bistability already at the molecular level; in low-polarity solvents the molecule is in the neutral state, TTF-$PTM^\bullet$, while in highly polar solvents it turns into a zwitterionic state, $TTF^{+\bullet}$-PTM^- (Fig.2.1).[125, 126, 127] Interestingly, in highly polar solvents (like DMF), thanks to the well-known tendency of $TTF^{+\bullet}$ to dimerize, $(TTF^{+\bullet}\text{-}PTM^-)_2$ dimers are observed. This dimer is the first example of a system showing both CT and IET degrees of freedom and it was described combining the essential-state model for CT dipolar chromophores together with the Hubbard model, typically used to attack $(TTF^{+\bullet})_2$ dimers.[128]

TTF takes part in both segregated and mixed stack CT crystals.[129]

The prototype of mixed stack CT crystals is TTF-CA, with CA standing for chloranil, where the electron donor (TTF) alternates with the electron acceptor (CA) in a ...DADADA... motif. The overlap between D and A adjacent frontier orbitals causes a partial CT and consequently electron delocalization along the molecular stack, thus leading to fractional charges, $\ldots D^{\rho+}A^{\rho-}D^{\rho+}A^{\rho-}D^{\rho+}A^{\rho-}\ldots$.

TTF-CA presents a typical phase transition, the Neutral-Ionic Transition (NIT), where the average charge on D and A molecular sites, ρ, grows from $\sim$0.2 (neutral phase) to $\sim$0.7 (ionic phase).[24, 25, 130, 108] NIT can be induced either lowering temperature or increasing the external pressure or using light. This phase transition is always accompanied by a structural instability that leads to lattice dimerization [108, 26] and finally causes ferroelectricity.[27]

Here, we propose a new kind of mixed stack CT crystal where D-π-R$^\bullet$ molecules alternate with A units to define a ...DADADA... supramolecular motif, where each D is decorated with an organic radical, R$^\bullet$, as sketched in Fig.2.2.

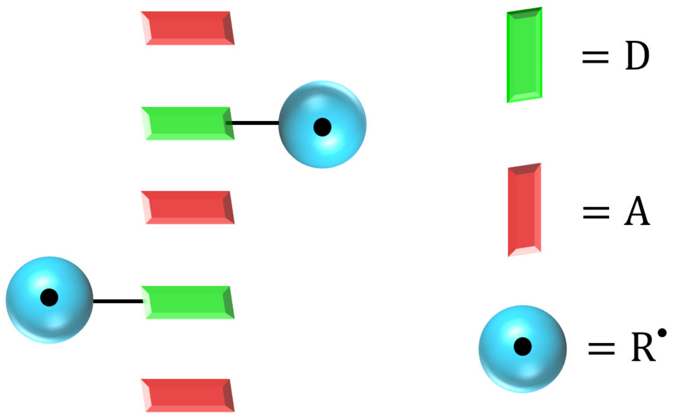

Figure 2.2: Sketch of an hypothetical structure of the decorated D(-π-R$^\bullet$)A mixed stack CT crystal.

In segregated-stack CT crystals, whose prototype is TTF-TCNQ (TCNQ = tetracyanoquinodimethane), electrons are delocalized along D stacks and A stacks, both kinds of stacks being partly filled because of a partial CT from D to A molecular units. TTF-TCNQ is the prototypical synthetic metal, where the partial CT between the two molecular stacks creates partially filled electronic bands and finally leads to metallic behaviour.[19, 131] More recently, starting from the MPTTF-PTM dyad (Fig.2.3, panel a), a novel single-component segregated stack CT crystal was synthesized (Fig.2.3, panel b).[132] Showing a monodimensional stacking of MPTTF units (electron donor), each of them being decorated with a segregating PTM organic radical (electron acceptor), this crystal combines for the first time IET with CT in the solid state, thus becoming a good candidate for future organic electronics. Moreover, magnetism as induced by the unpaired spins on radical moieties can make decorated segregated stacks attractive for spintronics too.[133]

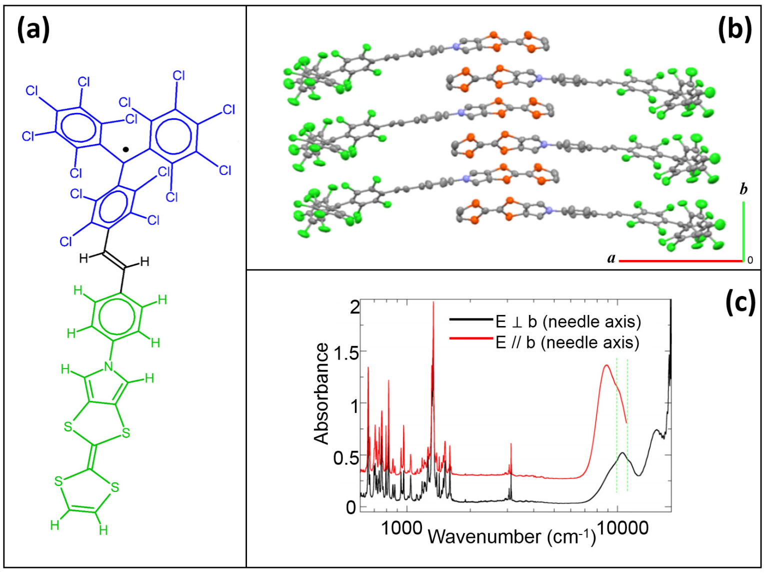

Figure 2.3: The MPTTF-PTM (monopyrrolotetrathiafulvalene-polychlorotriphenylmethyl radical) CT dyad. (a) Sketch of the molecular structure of MPTTF-PTM. (b) Ball-and-stick crystallographic structure of MPTTF-PTM crystal showing its monodimensional herringbone structure (atom color legend: sulfur in orange, carbon in grey, chlorine in green, nitrogen in blue). (c) Experimental polarized absorption spectra of the MPTTF-PTM crystal in panel b. Adapted from Ref.[132].

Putting IET and CT degrees of freedom together, both the decorated mixed stack in Fig.2.2 and the segregated stack MPTTF-PTM in Fig.2.3, panel b, show new emergent phenomena with intrinsic multifunctionality.

More precisely, the mixed stack structure sketched in Fig.2.2 could be the springboard to get innovative molecular multiferroics. In fact, in the ionic phase, ...$D^{+\bullet}A^{-\bullet}D^{+\bullet}A^{-\bullet}D^{+\bullet}A^{-\bullet}$..., mixed stack CT crystals show antiferromagnetic arrangement of neighboring spins. The same kind of magnetic correlations is observed within each $D^{+\bullet}$-π-$R^{\bullet}$ unit. As a result, if the main stack is in the ionic phase, a ferrimagnetic ordering of the spins is expected, one spin out of three per cell being unpaired, thus resulting in a finite macroscopic magnetization. Furthermore, the magnetic ordering is expected to coexist with the ferroelectric order as induced by the stack distortion, thus leading to a multiferroic organic material.

The neutral radicals MPTTF-PTM$^{\bullet}$ constituting the segregated stack CT crystal in Fig.2.3, panel b, can turn into a zwitterionic, MPTTF$^{+\bullet}$-PTM^{-}, state thanks to intramolecular electron transfer, thus leading to a reduction of the on-site electron-electron repulsion and to a potentially metallic phase along the MPTTF stack. Indeed, analyzing the experimental absorption spectra polarized along the MPTTF-PTM stacking direction and normally to it (Fig.2.3, panel c), the bands at $\sim$ 10000 cm^{-1} could be signatures of a weak intermolecular interaction.

In the first part of the Chapter, the theoretical modeling of the decorated mixed stack CT crystal is presented. In Section 2.1.1, the model Hamiltonian used to describe the novel decorated mixed stack CT crystal is presented; in Section 2.1.2 the numerical techniques used to attack the problem are discussed. Sections 2.1.3 and 2.1.4 are devoted to discuss results obtained for regular and dimerized chains, respectively. The second part of the Chapter is fully devoted to the theoretical description of the decorated segregated stack and its spectroscopic properties. The model Hamiltonian is introduced in Section 2.2.1, whereas calculated polarized electronic absorption spectra are reported in Section 2.2.2.

2.1 Decorated mixed stack

2.1.1 The model Hamiltonian

The D-π-$R^{\bullet}$ molecular unit is a CT dipolar ("push-pull") chromophore, where the electron donor group (D) is connected to the electron acceptor group ($R^\bullet$) through a conjugated π-bridge.[11, 12, 13, 123, 125, 127] The dyad can be described in terms of the essential two-state model overviewed in Sect.1.2.1. Summarizing the theory behind this model, CT dipolar dyes resonate between two main resonance structures, a neutral one and a zwitterionic one. An essential two-state model describes the chromophore electronic degrees of freedom in terms of just two electronic states, a neutral one, $|\mathrm{D}\text{-}\pi\text{-}\mathrm{R}^\bullet\rangle$, and a charge-separated one, $|\mathrm{D}^{+\bullet}\text{-}\pi\text{-}\mathrm{R}^-\rangle$. On this basis set, the Hamiltonian matrix is the 2×2 matrix in Eq.1.48, defined by two parameters, $2z$, the energy difference between $|\mathrm{D}\text{-}\pi\text{-}\mathrm{R}^\bullet\rangle$ and $|\mathrm{D}^{+\bullet}\text{-}\pi\text{-}\mathrm{R}^-\rangle$ states, and τ, the (opposite of) the mixing matrix element.

In a mixed stack CT crystal the electrons are delocalized along the stack thus creating a quasi monodimensional system, where the inter-stack electrostatic interactions can be treated at the mean-field level.[30] The model typically used to describe the electrons along the stack is the Hubbard model modified in order to account for the different nature of molecular sites.[26, 46, 31, 47] The minimal Hamiltonian reads:

$$\begin{aligned} \hat{H} &= \Delta\sum_i(-1)^i\hat{n}_i \\ &+U\sum_i \hat{n}_{i,\uparrow}\hat{n}_{i,\downarrow} \\ &-t\sum_{i,\sigma}(\hat{c}^\dagger_{i,\sigma}\hat{c}_{i+1,\sigma}+H.c.), \end{aligned} \tag{2.1}$$

where the sums run on the stack molecular sites, with odd (even) i values used for electron donor (acceptor) molecular units, and on the two electronic spin polarizations. The operators $\hat{c}_{i,\sigma}$, $\hat{c}^\dagger_{i,\sigma}$ are the annihilation and creation fermionic operators, i.e. they destroy and create, respectively, one electron with spin σ on the i-th molecular site. The fermionic number operator, $\hat{n}_i = \hat{n}_{i,\uparrow}+\hat{n}_{i,\downarrow} = \sum_\sigma \hat{c}^\dagger_{i,\sigma}\hat{c}_{i,\sigma}$, counts the total number of electrons on the i-th site. 2Δ is the energy difference between the site orbitals on D and A, the Hubbard U measures the on-site electron-electron electrostatic repulsion, assumed to be the same for both D and A. Finally, the third line of the equation represents electron delocalization along the stack with t being the electronic hopping integral.

In order to reduce the total number of parameters entering Eq.2.1 as well as the basis dimension, the reduced basis approximation is introduced, neglecting all the states having doubly charged molecular sites, namely D^{2+} and A^{2-}. This corresponds to impose the large correlation limit, $U, \Delta \to \infty$ with a finite energy difference 2Γ=2Δ-U.[134, 108, 30, 47]

The model Hamiltonian for the D(-π-R$^\bullet$)A decorated mixed stack CT crystal combines the essential two-state model for CT dipolar chromophores with the Hubbard model for mixed stack CT crystals in Eq.2.1. The decorated Hubbard model reads:

$$\begin{aligned}
\hat{H} \;=\; & \sum_i (\varepsilon_A \hat{n}_{i,A} + \varepsilon_D \hat{n}_{i,D} + \varepsilon_R \hat{n}_{i,R}) \\
& + \sum_i (U_A \hat{n}_{i,A,\uparrow}\hat{n}_{i,A,\downarrow} + U_D \hat{n}_{i,D,\uparrow}\hat{n}_{i,D,\downarrow} + U_R \hat{n}_{i,R,\uparrow}\hat{n}_{i,R,\downarrow}) \\
& - t(1+\delta) \sum_{i,\sigma} (\hat{c}^\dagger_{i,A,\sigma}\hat{c}_{i,D,\sigma} + H.c.) \\
& - t(1-\delta) \sum_{i,\sigma} (\hat{c}^\dagger_{i,D,\sigma}\hat{c}_{i+1,A,\sigma} + H.c.) \\
& - \tau \sum_{i,\sigma} (\hat{c}^\dagger_{i,D,\sigma}\hat{c}_{i,R,\sigma} + H.c.) + N_c t^2 \frac{\delta^2}{2\varepsilon_d},
\end{aligned} \tag{2.2}$$

where i runs over the N_c unit cells, whereas σ on spin polarizations; the first line accounts for on-site energies; the second line accounts for the repulsion between two electrons on the same molecular site. The subsequent two lines describe the hopping of electrons between adjacent sites along the stack with alternating, $t(1+\delta)$ and $t(1-\delta)$, hopping integrals describing dimerization. In the last line of the equation, the τ-term accounts for D-π-R$^\bullet$ intramolecular electron transfer, whereas the last term describes the lattice distortion elastic energy, with ε_d being the relevant lattice relaxation energy.[26, 46, 31, 47]

Long-range intra and interchain electrostatic interactions are important in conventional mixed stack CT crystals and they are usually treated at the mean-field level.[135, 30, 47] Indeed, results obtained using the decorated Hamiltonian in Eq.2.2, neglect long-range Coulomb interactions, but represent the starting point for a mean-field treatment. However, we did not extend our study to this point, the relevant parameter space being already very complex.

Two auxiliary quantities are introduced, namely 2Γ=$\varepsilon_A-\varepsilon_D-U_D$, being the energy required for the DA→$D^{+\bullet}A^{-\bullet}$ process, and $2z$=$\varepsilon_R-\varepsilon_D-U_D+U_R$, being the energetic cost for the intramolecular process D-π-R$^\bullet$ $\rightarrow$D$^{+\bullet}$-π-R$^-$.

2.1.2 Numerical approach

The unit cell of the decorated mixed stack counts three site orbitals and three electrons and if N_c is the number of unit cells, the problem describes N=3N_c electrons on N sites.

Weakly interacting electrons (i.e., $U/t \ll 1$) can be treated within the monoelectronic approximation as an ensemble of independent particles, using the Hartree-Fock approximation. The system Hamiltonian can be written as the sum of N single-particle Hamiltonians, whereas the system total wave function can be approximated as an antisymmetrized product of N monoelectronic wave functions each of them obtained diagonalizing the relevant single-particle Hamiltonian. As a consequence, the problem reduces to the diagonalization of the monoelectronic Hamiltonian with dimension $N \times N$. When dealing with crystals, the translational symmetry reduces the problem to the diagonalization of N_C Hamiltonians with dimension N/N_C.

For strongly correlated electrons (i.e., $U/t \gg 1$), the monoelectronic approximation breaks down and the single-particle picture discussed above must be extended in order to account for electron-electron interactions, ideally by means of a full configuration interaction (full-CI) calculation. Using a full-CI, all the possible configurations obtained by distributing N electrons among N crystal orbitals are allowed to interact. The resulting full-CI basis dimension makes the calculation unfeasible for large-size systems.

A different approach to strongly correlated electronic systems is possible, namely the exact diagonalization of the Hamiltonian written on the real-space basis (RS-ED). Within the RS-ED approach the Hamiltonian matrix is written on the Hilbert space spanned by the complete set of Slater determinants obtained by distributing N electrons among N site-orbitals. Four electronic states are possible for each molecular site, namely $|\uparrow\downarrow\rangle$, $|\uparrow\rangle$, $|\downarrow\rangle$, $|0\rangle$, corresponding to the doubly occupied, singly occupied (with up and down spin) and empty site, respectively. Increasing the chain length, the basis dimension exponentially increases according to the expression $2N(2N-1)...(2N-N+1)/N!$, thus reaching the same dimension of a full-CI calculation. However, the RS-ED approach has two main advantages over the full-CI. First of all, within the real-space basis, site energies and on-site Coulomb repulsions enter the Hamiltonian diagonal part, whereas electronic kinetic energy contributes to the off-diagonal terms;[136] the resulting Hamiltonian is a sparse matrix, with off-diagonal terms smaller in magnitude (large correlation limit) than diagonal ones, and efficient diagonalization routines can be used. Secondly, a reduced basis can be easily defined neglecting all those electronic configurations that are too high in energy. Specifically, states including either A^{2-} or R^{+} are expected to poorly contribute to the ground state because of their high energy and can be easily neglected.

A further reduction of the problem dimension can be achieved by exploiting the spin symmetry;[137] to this end, two auxiliary operators can be introduced, namely $\hat{S}^2$ and $\hat{S}_z$, in order to define the square modulus and the z-component, respectively, of the total spin. $\hat{S}^2$ eigenstates are defined by the quantum number S=0, 0.5, 1, 1.5,... and for each S value, $2S+1$ eigenvalues of $\hat{S}_z$ are defined, namely S_z=$-S$, $-(S-1)$,..., $S-1$, S. The Hamiltonian in Eq.2.2 commutes with both $\hat{S}^2$ and $\hat{S}_z$, thus having a common set of eigenstates. Real-space basis functions are eigenstates of $\hat{S}_z$ and through the Diagrammatic Valence Bond (DVB) approach, they are combined to become $\hat{S}^2$ eigenstates as well.[136, 138] Because of the non-orthogonal nature of the Valence Bond basis as well as the rather complicated treatment of $S \neq 0$ spin spaces within the DVB approach, real-space functions are used in this study, thus working in different S_z spin spaces.

2.1.2.1 Bit representation

Each real-space basis function can be represented as an integer number, exploiting its binary (bit) representation.[136] Indeed, the information on the occupation of each molecular site can be stored in a compact way using two bits (Fig.2.4). Specifically, 00 and 11 represent an empty and a doubly occupied site, respectively, while 01 (10) represent a molecular site with a spin up (down). Numbering different sites, each real-space basis function, $|k\rangle$, is fully described by the integer k that corresponds to the binary number with $2N$ digits, where bits number $2p-2$ and $2p-1$ are associated with site $p=1,...,N$.

The real-space basis functions are built by checking all the integers up to 2^{2N} and keeping only those that represent a correct state in the relevant S_z

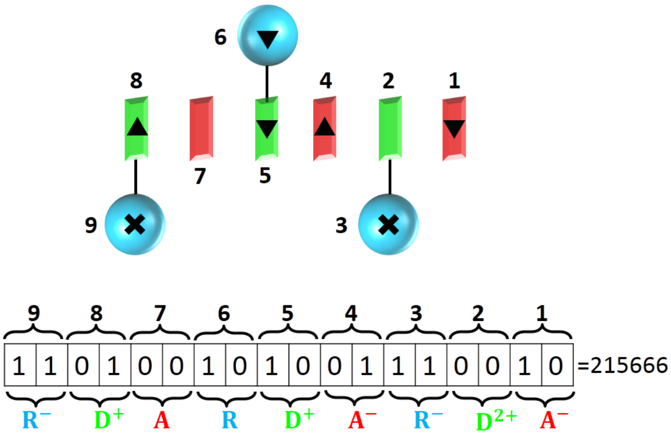

Figure 2.4: Bit representation of a 9-membered chain fragment of the decorated mixed stack discussed in this Section. Cross marks a doubly occupied molecular site, whereas triangle up (down) marks a site with a spin up (down).

spin space; to this end, the number of electrons must be equal to N, while the difference between the number of spins up and spins down must be equal to $2S_z$. By sorting the resulting integers in ascending order, efficient search algorithms, like the binary search, can be used.

2.1.2.2 Reduced basis

Using the real-space basis, the problem can be simplified by adopting a reduced basis. Within mixed stack CT crystals, states containing doubly charged sites, D^{2+} and A^{2-}, are usually neglected.[134, 108, 30, 47] In this work, A^{2-} states are neglected, while D^{2+} states are maintained accessible in order to properly describe antiferromagnetic correlations within the $D^{+\bullet}$-π-$R^{\bullet}$ dyad. Moreover, being $R^{\bullet}$ an electron acceptor, states having R^{+} sites are neglected being too high in energy. The resulting reduced basis corresponds to the $U_R, U_A \to \infty$ limit, while keeping finite 2Γ and $2z$. As far as U_D is concerned, the $U_D/t \gg 1$ limit is considered. Table 2.1 reports the number of states entering the complete as well as reduced basis within different spin spaces and for different chain lengths.

number of sites (number of cells, N_c)	S_z	complete basis	reduced basis
6(2)	0	400	144
	1	225	90
	2	36	20
	3	1	1
9(3)	0.5	15876	3276
	1.5	7056	1689
	2.5	1296	420
	3.5	81	42
	4.5	1	1
12(4)	0	853776	97320
	1	627264	75672
	2	245025	35082
	3	48400	9256
	4	4356	1260
	5	144	72
	6	1	1
15(5)	0.5	41409225	2686310
	1.5	25050025	1781880
	2.5	9018009	772156
	3.5	1863225	211310
	4.5	207025	34345
	5.5	11025	2970
	6.5	225	110
	7.5	1	1
18(6)	0	2363904400	85287420
	1	1914762564	71806956
	2	1012766976	42666936
	3	344622096	17644761
	4	73410624	4950036
	5	9363600	903240
	6	665856	100136
	7	23409	6006
	8	324	156
	9	1	1

Table 2.1: Dimension of the relevant spin spaces for different lengths of the decorated mixed stack. Dimension of the reduced basis is also shown.

2.1.2.3 Writing the Hamiltonian matrix

We calculate, for each spin subspace, the (real and symmetric) Hamiltonian matrix. Calculation of the relevant matrix elements starts from writing each real-space state, $|k\rangle$, in the Fock space as:

$$|k\rangle \quad = \quad \prod_{i=1}^{2N} \hat{c}_i^\dagger |0\rangle, \tag{2.3}$$

where i runs on the $2N$ spin-orbitals of a N sites chain and $|0\rangle$ is the state with no electrons present. The configuration reported in Fig.2.4 can be written as:

$$|\underbrace{01}_{1}\underbrace{00}_{2}\underbrace{11}_{3}\underbrace{10}_{4}\underbrace{01}_{5}\underbrace{01}_{6}\underbrace{00}_{7}\underbrace{10}_{8}\underbrace{11}_{9}\rangle = \hat{c}_{1,\beta}^\dagger \hat{c}_{3,\alpha}^\dagger \hat{c}_{3,\beta}^\dagger \hat{c}_{4,\alpha}^\dagger \hat{c}_{5,\beta}^\dagger \hat{c}_{6,\beta}^\dagger \hat{c}_{8,\alpha}^\dagger \hat{c}_{9,\alpha}^\dagger \hat{c}_{9,\beta}^\dagger |0\rangle. \tag{2.4}$$

Terms entering the first two lines of Eq.2.2, namely site energy and on-site electronic repulsion, are diagonal within the real-space basis and are calculated simply counting the number of electrons along the N molecular sites. Using the binary representation, this corresponds with counting the number of digits “1” entering the relevant binary number.

The remaining off-diagonal terms entering Eq.2.2 describe inter and intramolecular electron transfer, thus mixing different basis functions within the same spin space. We illustrate the process for some of the transfer terms operating on the configuration in Eq.2.4. Starting from the term that transfers an electron from site number five to site number four (D-A intra cell hopping):

$$t\hat{c}_{4,\beta}^\dagger \hat{c}_{5,\beta} |010011\underbrace{10}_{4}\underbrace{01}_{5}01001011\rangle = t|010011\underbrace{11}_{4}\underbrace{00}_{5}01001011\rangle. \tag{2.5}$$

Analogously, the electron can hop between two different cells:

$$t\hat{c}_{7,\beta}^\dagger \hat{c}_{5,\beta} |01001110\underbrace{01}_{5}01\underbrace{00}_{7}1011\rangle = -t|01001110\underbrace{00}_{5}01\underbrace{01}_{7}1011\rangle, \tag{2.6}$$

where the electron is transferred from site number five to site number seven. Crucially, the different sign entering the two matrix elements calculated above reflects the fermionic anticommutation rules:

$$\{\hat{c}_i, \hat{c}_j\} \quad = \quad 0,$$

$$\begin{aligned}\{\hat{c}_i^\dagger, \hat{c}_j^\dagger\} &= 0, \\ \{\hat{c}_i, \hat{c}_j^\dagger\} &= \delta_{i,j}, \end{aligned} \tag{2.7}$$

where in the third line $\delta_{i,j}$ is the Kronecker delta. When the electron is moved along the chain, an even (odd) number of electrons between the starting and the final positions makes the relevant matrix element positive (negative). Using the Born-von Kàrmàn periodic boundary conditions (PBC), the following equalities can be written as well:

$$\begin{aligned} t\hat{c}_{8,\beta}^\dagger \hat{c}_{1,\beta} |\underbrace{01}_{1}001110010100\underbrace{10}_{8}11\rangle &= t|\underbrace{00}_{1}001110010100\underbrace{11}_{8}11\rangle, \\ t\hat{c}_{1,\beta}^\dagger \hat{c}_{8,\beta} |\underbrace{01}_{1}001110010100\underbrace{10}_{8}11\rangle &= 0, \end{aligned} \tag{2.8}$$

where in the first line the electron moves between last unit cell D site and first unit cell A site, whereas the second line follows from the $\hat{c}_i|0\rangle = 0$, $\forall$ i.

The Hamiltonian matrix is sparse: having imposed the PBC, N sites form N nearest neighbor bonds and the electron transfer creates either 0 or 1 or 2 new configurations for each bond. As a consequence, it is convenient to store in the computer memory only the non-zero elements of either the upper or lower triangle of the matrix. Different recipes can be used to this aim, being all based on the main idea to collect the non-zero elements within an array and using some auxiliary arrays in order to keep track of their position within the original matrix. The simplest, but not highly efficient, format is the so-called coordinate format where the non-zero elements and the relevant row/column indexes are stored in three different arrays. In this work, the compressed sparse row (CSR) format in the 3-array variation is used.[139] Using this format, non-zero elements are located by checking one row at a time and are stored within the *value* array, while the relevant column indexes are stored within the *column* array. The third array, *row*, keeps track of the index the first non-zero element of each row has within the *value* array. Actually, because the matrix is symmetric, we only store its upper triangle, so that the array *row* contains the indexes the originally diagonal terms have within the *value* array. Moreover, *row* last term is equal to the number of non-zero elements increased by one. For the sake of clarity, the CSR format in the 3-array variation for the symmetric matrix,

A, reads:

$$A \;=\; \begin{pmatrix} 3 & 0 & 1 & 0 & 3 & 0 \\ 0 & 7 & 0 & 6 & 0 & 0 \\ 1 & 0 & 0 & 2 & 0 & 0 \\ 0 & 6 & 2 & 7 & 0 & 0 \\ 3 & 0 & 0 & 0 & 9 & 0 \\ 0 & 0 & 0 & 0 & 0 & 1 \end{pmatrix},$$

$$value = \begin{pmatrix} 3 & 1 & 3 & 7 & 6 & 0 & 2 & 7 & 9 & 1 \end{pmatrix},$$

$$column = \begin{pmatrix} 1 & 3 & 5 & 2 & 4 & 3 & 4 & 4 & 5 & 6 \end{pmatrix},$$

$$row = \begin{pmatrix} 1 & 4 & 6 & 8 & 9 & 10 & 11 \end{pmatrix}.$$

In the matrix dense format, the A matrix requires the storage of 36 double precision numbers. Moving to the coordinate format, three different arrays, each with 10 elements (10 is the number of non-zero elements in the upper triangle of A, where a zero on the diagonal is considered as a non-zero element), are used. Using the CSR format in the 3-array variation, the *row* array contains just 7 integers. The small advantage highlighted here dramatically increases when moving to larger sparse matrixes.

Calculation of the off-diagonal terms entering Eq.2.2 becomes lengthy for systems with $N_c > 3$. Consequently, in order not to repeat the calculations for different sets of parameters, the off-diagonal terms of the Hamiltonian are divided into four parts that are calculated separately:

1. D-A intra cell hopping, that is the third line in Eq.2.2;
2. D-A inter cell hopping, expressed by the fourth line in Eq.2.2;
3. D-A hopping due to the PBC, i.e. $-t(1-\delta)\sum_\sigma(\hat{c}^\dagger_{N_c,D,\sigma}\hat{c}_{1,A,\sigma} + H.c.)$;
4. D-π-R$^\bullet$ intramolecular hopping, that is the fifth line in Eq.2.2.

The Hamiltonian elements entering these four parts are calculated just once for different N_c and S_z values and consequently stored in the computer memory. The total off-diagonal Hamiltonian is finally obtained summing the four different parts with the relevant t, δ and τ values.

2.1.2.4 Diagonalization

Diagonalization of large matrixes requires a huge amount of machine memory. Using the matrix dense format, the calculation of eigenvalues and eigenvectors requires at least two matrixes as big as the matrix to diagonalize and an additional working area whose dimension depends on the algorithm. A reduction of the required computer memory can be achieved when looking only for a subset of eigenvalues and relevant eigenvectors. Anyhow, storing the matrix in the dense format needs a large amount of memory. To be specific, $2{\cdot}10^9$ double precision real numbers can be stored within the 16GBytes memory of a good workstation. This means that the biggest matrix that can be stored in the computer memory is as large as 44721×44721. As a result, diagonalization of the Hamiltonian matrix for $N_c > 3$ would be impossible (see Tab.2.1).

Fortunately, larger size systems can be attacked using very efficient diagonalization routines for sparse matrixes from ARPACK library.[140] Using the Reverse Communication Interface, ARPACK routines never directly operate on the target matrix, turning the control to the calling program whenever a matrix operation (like a matrix-vector multiplication) is required. Consequently, ARPACK routines can deal with any matrix storage format. The algorithm used is the Implicitly Restarted Arnoldi Method (IRAM) that boils down to the Lanczos algorithm (IRLM) for the hermitian matrix in Eq.2.2. Both algorithms are based on the construction of a Krylov space, $\{|v\rangle, \hat{H}|v\rangle, ..., \hat{H}^{n-1}|v\rangle\}$, where $|v\rangle$ is a random array and n is typically set to 14-32 (see Appendix B). The Hamiltonian is further written on the Krylov space and is diagonalized to get Ritz eigenvalues. For large enough n values, the resulting n Ritz eigenvalues approximate the extreme $\hat{H}$ eigenvalues.

2.1.2.5 Symmetrized basis

Adopting Born-von Kàrmàn PBC, crystal translational symmetry maps into rotational symmetry, with a C_{N_c} symmetry axis. For the sake of clarity, the action of a C_2 axis on the electronic configuration reported in Fig.2.5 can be studied. Using the second quantization formalism previously introduced, the electronic configuration on the left reads:

$$|110010001110\rangle \quad = \quad \hat{c}^{\dagger}_{1,\alpha}\hat{c}^{\dagger}_{1,\beta}\hat{c}^{\dagger}_{3,\alpha}\hat{c}^{\dagger}_{5,\alpha}\hat{c}^{\dagger}_{5,\beta}\hat{c}^{\dagger}_{6,\alpha}|0\rangle \qquad (2.9)$$

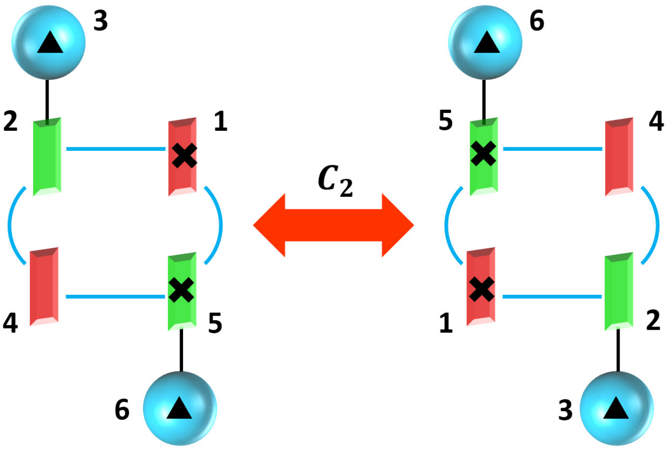

Figure 2.5: Periodic boundary conditions in the decorated mixed stack CT crystal. Sketch of a two-cell long chain closed into a ring together with its symmetrical one respect to a C_2 axis normal to the ring plane. Cross marks a doubly occupied molecular site, while triangle up marks a site with a spin up.

and using a C_2 axis operator on it, results:

$$\begin{aligned}\hat{C}_2|110010001110\rangle &= \hat{c}^\dagger_{5,\alpha}\hat{c}^\dagger_{5,\beta}\hat{c}^\dagger_{6,\alpha}\hat{c}^\dagger_{1,\alpha}\hat{c}^\dagger_{1,\beta}\hat{c}^\dagger_{3,\alpha}|0\rangle \\ &= -\hat{c}^\dagger_{1,\alpha}\hat{c}^\dagger_{1,\beta}\hat{c}^\dagger_{3,\alpha}\hat{c}^\dagger_{5,\alpha}\hat{c}^\dagger_{5,\beta}\hat{c}^\dagger_{6,\alpha}|0\rangle \\ &= -|110010001110\rangle. \end{aligned} \tag{2.10}$$

Consequently, the relevant totally symmetric real-space basis function reads:

$$\mathcal{S}_A = \frac{1}{\sqrt{2}}\Big(|110010001110\rangle - |110010001110\rangle\Big) = 0, \tag{2.11}$$

where the index A refers to the totally symmetric irreducible representation within the C_2 point group. On the other hand, the real-space basis function projected on the totally antisymmetric space, B, reads:

$$\mathcal{S}_B = |110010001110\rangle. \tag{2.12}$$

Summing up, adopting the PBC, if a diagram rotates, the i-th unit cell becomes the $(i+1)$-th cell and the last one becomes the first one. Consequently, the fermionic operators relevant to the electrons in the last unit cell have to jump over all the others. For an odd number of unit cells, the number of electrons, $N = 3N_c$, is odd as well and the phase of the fermionic wave function is always preserved, $|\vec{k}| = 0$ being the only relevant wave vector sector. On the contrary, if N_c is even, the wave function phase changes when an odd number of electrons are contained within the last unit cell (see Eq.2.10) and different $|\vec{k}|$ values must be considered (see Eqs.2.11 and 2.12).

2.1.3 Regular decorated mixed stack

In this Section, adopting the reduced basis presented in Sect.2.1.2.2 and setting U_D=10 eV, results obtained in a large region of the $(2\Gamma, 2z)$ plane are discussed. Moreover, the intermolecular D-A hopping integral, t, is set to the characteristic TTF-CA value, 0.21 eV, [141, 142] whereas the D-π-R$^\bullet$ intramolecular hopping integral, τ, is set to 0.4 eV. However, results for different U_D, t and τ values will be discussed as well.

The $(2\Gamma, 2z)$ plane can be divided into three different regions (marked as N, Z and I in Fig.2.6) according to the charge distribution in the lowest energy configuration (accounting for t=τ=0):

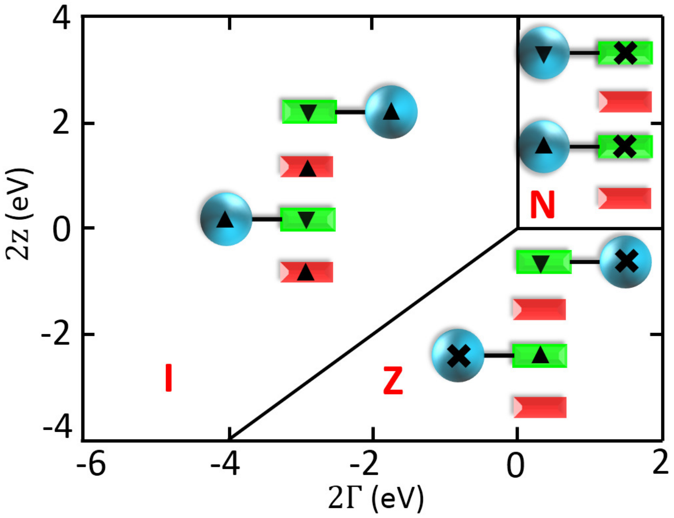

Figure 2.6: The phase diagram of the decorated mixed stack CT crystal. Sketch of the relevant electronic configurations is overlapped. Cross marks a doubly occupied molecular site, while triangle up (down) marks a site with a spin up (down).

N. For positive 2Γ and $2z$ values, the decorated mixed stack is governed by neutral D, A and $R^{\bullet}$ molecular sites. The unpaired spins on $R^{\bullet}$ can not communicate, thus leading to a paramagnetic phase;

Z. For $2z < 0 \wedge 2\Gamma > 2z$, the system is dominated by D-π-$R^{\bullet}$ $\rightarrow D^{+\bullet}$-π-R^{-} intramolecular electron transfer, with A sites staying empty. No communication is present between the unpaired spins on D sites and the phase is paramagnetic;

I. For $2z > 2\Gamma \wedge 2\Gamma < 0$, intermolecular electron transfer, D(-π-$R^{\bullet}$)A$\rightarrow D^{+\bullet}$(-π-$R^{\bullet}$)$A^{-\bullet}$, is favoured, every molecular site presenting an unpaired electron.

The N-I, N-Z, I-Z phase boundaries are expected at 2Γ=0 , $2z$=0 , $2z$=2Γ, respectively, in agreement with Fig.2.6.

The I phase is the fundamental one for the work presented in this Section, in fact the antiferromagnetic arrangement of neighboring spins along the D-A stack potentially induces an overall ferrimagnetic order, with a resulting ferromagnetic locking of the unpaired spins on $R^{\bullet}$ sites. The I phase only survives in the strong correlation limit, which is not captured in the Hartree-Fock treatment of electronic correlations.[46] Therefore, we use the RS-ED approach discussed in Sect.2.1.2 to calculate fully correlated eigenstates of the single-chain Hamiltonian in Eq.2.2 for finite size rings with an even number of cells, up to N_c=6.

2.1.3.1 Magnetic order

To verify the presence of ferrimagnetic correlations within the I phase, we calculate the energies of the states with different spin multiplicity. Figure 2.7 shows the energy gap, $\Delta E_{S.-F.}$, between the lowest singlet state (S=0) and the lowest state with S=$N_c/2$, as a function of both 2Γ and $2z$. In a large region of the I phase, the state with S=$N_c/2$ is considerably lower in energy than the lowest singlet state and, as a result, $\Delta E_{S.-F.}$ is large and positive (energy difference is reported in Kelvin). Consequently, within this region the decorated mixed stack can present ferrimagnetic ordering up to ambient temperature. On the contrary, $\Delta E_{S.-F.}$ completely vanishes in the N and Z phases, denoting the paramagnetic nature of the stack within these two phases, with unpaired spins on either $R^\bullet$ (N phase) or $D^{+\bullet}$ (Z phase) units not communicating.

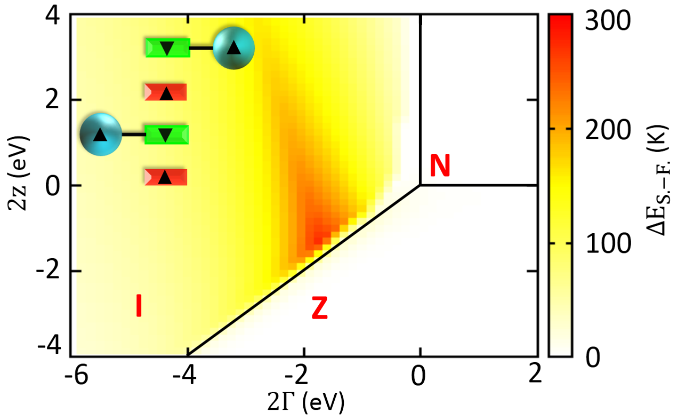

Figure 2.7: $\Delta E_{S.-F.}$ in the (2Γ,$2z$) plane for the decorated non-dimerized chain with N_c=4, that is the energy difference (in Kelvin) between the lowest singlet state and the lowest quintet state (S=2). The phase diagram from Fig.2.6 is overlapped together with a sketch of the dominant electronic configuration within the I phase.

The calculation of the map in Fig.2.7 becomes extremely time-consuming for large N_c values. Consequently, in order to compare $\Delta E_{S.-F.}$ for increasing N_c values, we show sections of the map for fixed 2Γ and $2z$ values. Figure 2.8 shows, for decorated stacks with N_c=4, 6, different sections of the energy gap between the lowest singlet state and the relevant lowest state with high spin multiplicity (i.e., S=2, 3 for N_c=4, 6, respectively). Left panel shows $\Delta E_{S.-F.}$ sections as a function of the intermolecular ionization energy, 2Γ, for two different values of $2z$, whereas the right panel presents $\Delta E_{S.-F.}$ as a function of the intramolecular D-π-$R^\bullet$ $\rightarrow D^{+\bullet}$-π-R^- energy, $2z$, for two different values of 2Γ. These results confirm the existence of the ferrimagnetic phase for increasing chain lengths within a large region of the I phase. Moreover, Figure 2.9 shows sizeable nearest-neighbor $R^\bullet$ spin correlation function:

$$C_{RR} = \frac{1}{N_c} Tr\left\{\hat{\rho}\sum_{i=1}^{N_c}\hat{S}_{z,R,i}\hat{S}_{z,R,i+1}\right\}, \tag{2.13}$$

where $\hat{S}_{z,R,i}$ measures the z-component of the $R^\bullet$ spin in the i-th unit cell,

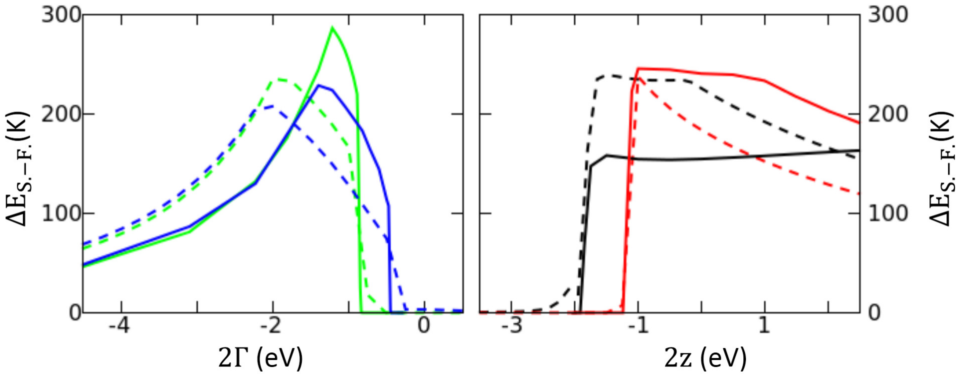

Figure 2.8: Finite size effects on $\Delta E_{S.-F.}$. The energy difference $\Delta E_{S.-F.}$ is reported as a function of 2Γ (left) and of $2z$ (right) for N_c=4 (dashed lines) and 6 (continuous lines). Different sections are calculated for $2z$ equal to -0.5 eV (green curve), 0.5 eV (blue curve) and for 2Γ equal to -2 eV (black curve), -1.4 eV (red curve). Results obtained for τ=0.4 eV, t=0.21 eV, U_D=10 eV.

whereas $\hat{\rho}$ is the quantum Boltzmann distribution:

$$\hat{\rho} \quad = \quad \frac{e^{-\beta\hat{H}}}{Tr\left\{e^{-\beta\hat{H}}\right\}}, \tag{2.14}$$

where the trace operations in both Eqs.2.13 and 2.14 are over the complete set of eigenstates of the Hamiltonian in Eq.2.2. Indeed, results shown in Fig.2.9 at 10 K, 50 K, 80 K, are obtained truncating the trace to the first few eigenstates, higher ones being not appreciably populated at relevant temperatures.

Large and finite $\Delta E_{S.-F.}$ values in the I phase are accompanied by ferromagnetic correlations between unpaired spins on adjacent R$^\bullet$ units, C_{RR} amounting to a significant fraction of the limiting value, C_{RR}=0.25.

Applying an external magnetic field, B, the following interaction term enters the Hamiltonian in Eq.2.2:

$$\hat{H}_z \quad = \quad -BN_c\hat{M}_z, \tag{2.15}$$

where $\hat{M}_z$=$(\sum_{i=1}^{N_c}\hat{S}_{z,R,i})/N_c$ is the z-component of the magnetization operator, $\hat{\vec{M}}$. In Figure 2.10, on the left, the expectation value of the magnetization along z, M_z=$Tr\{\hat{\rho}\hat{M}_z\}$, is shown against the magnetic field for

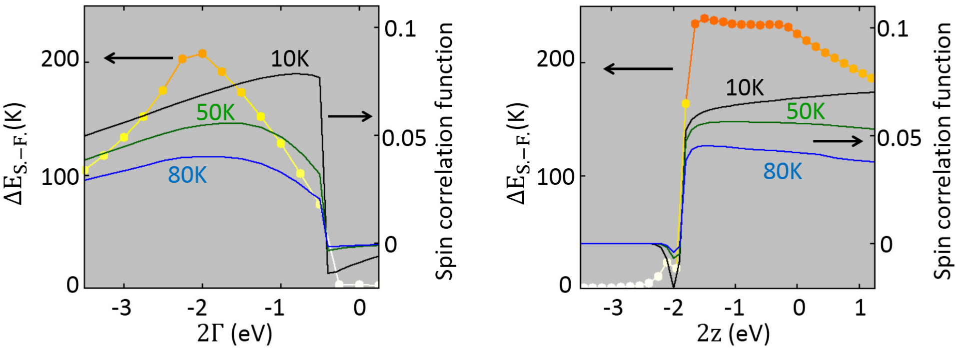

Figure 2.9: Nearest-neighbor R$^\bullet$ spin correlation functions as a function of 2Γ, setting $2z$=0.5 eV (left panel) and as a function of $2z$, setting 2Γ=-2 eV (right panel) for a ring with N_c=4; different colors (black, green, blue) refer to different temperatures. Relevant $\Delta E_{S.-F.}$ is also shown as a colored dotted line. Calculations done for the same parameters used in Fig.2.8.

three different temperatures, namely 10 K, 50 K and 80 K. As soon as B is switched on, M_z becomes finite, with the steep slope observed at B=0 at 10 K gradually reducing while going up in temperature.

Inside the decorated mixed stack CT crystal, three-dimensional interchain interactions can be written as:

$$\hat{H}_\alpha = -\frac{1}{2}\sum_{i,j}\alpha_{i,j}\hat{S}_{z,R,i}\hat{S}_{z,R,j}, \tag{2.16}$$

where the indexes i and j run over all the R$^\bullet$ units in the crystal, $\alpha_{i,j}$ being the relevant coupling strengths. Eq.2.16 drastically simplifies when limiting the interaction to nearest neighbor R$^\bullet$ spins:

$$\hat{H}_\alpha = -\frac{\alpha}{2}\sum_{\langle i,j\rangle}\hat{S}_{z,R,i}\hat{S}_{z,R,j}, \tag{2.17}$$

where $\alpha > 0$ is assumed to be the same for all R$^\bullet$ sites. Introducing the statistical fluctuation of the z-component of R$^\bullet$ spin, $\delta\hat{S}_{z,R,i} = \hat{S}_{z,R,i} - \langle\hat{S}_{z,R,i}\rangle$, and neglecting the product of the two fluctuation terms (i.e., adopting the mean-field approximation), Eq.2.17 becomes:

$$\begin{aligned}\hat{H}_\alpha &\simeq -\frac{\alpha}{2}\sum_{\langle i,j\rangle}\langle\hat{S}_{z,R,i}\rangle\langle\hat{S}_{z,R,j}\rangle - \alpha N_c M_z\sum_i \delta\hat{S}_{z,R,i} \\ &\simeq \frac{\alpha}{2}N_c^2 M_z^2 - \alpha N_c M_z\sum_i \hat{S}_{z,R,i}. \end{aligned}\tag{2.18}$$

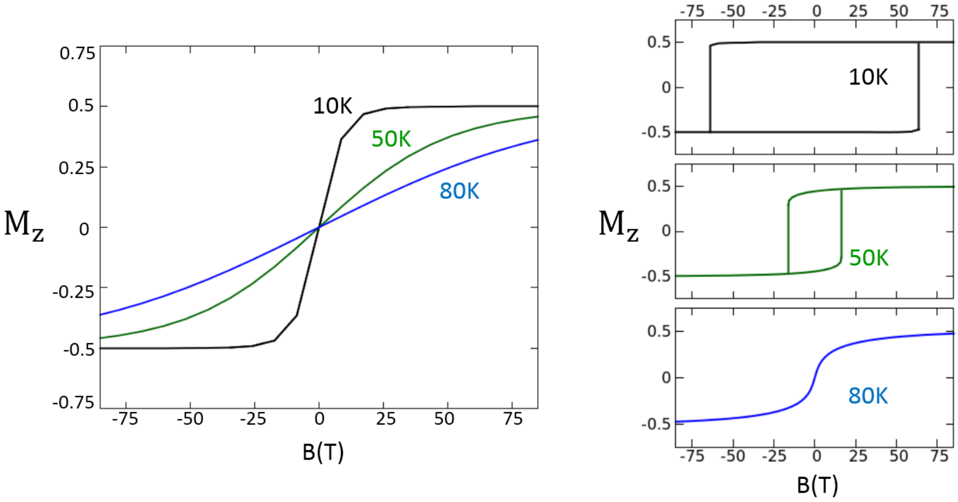

Figure 2.10: Magnetization as a function of an externally applied magnetic field (in Tesla) for three different temperatures, for a ring with N_c=4. Calculations done by setting 2Γ=-2 eV and $2z$=0.5 eV, for the same parameters used in Fig.2.8. On the right, relevant hysteresis loops obtained accounting for interchain interactions at the mean-field level, by setting α=5 meV.

Combining Eq.2.15 with Eq.2.18, one gets:

$$\hat{H}_z + \hat{H}_\alpha \simeq -B' \sum_i \hat{S}_{z,R,i} + \frac{\alpha}{2} N_c^2 M_z^2, \tag{2.19}$$

where $B' = B + \alpha N_c M_z$ is the effective magnetic field felt by the i-th R$^\bullet$ spin.[143] As a result, magnetic hysteresis loops in Fig.2.10 appear by introducing the mean-field correction to the magnetic field, that is substituting B in Eq.2.15 with $B' - \alpha N_c M_z$. For a small mean-field interchain interaction, α=5 meV, a large loop is obtained at 10 K and disappears while approaching 80 K.

Finally, the three panels in Fig.2.11 show the effect of varying t, τ and U_D on $\Delta E_{S.-F.}$. The dashed blue line already shown in Fig.2.8, left panel, is reported here in order to compare previous results with those obtained for different t, τ and U_D values. In particular, the maximum value of $\Delta E_{S.-F.}$ dramatically increases when reducing the on-site D repulsion, whereas an increment of U_D determines a reduction of the stabilization of the ferrimagnetic phase, with the maximum of $\Delta E_{S.-F.}$ moving deep into the I phase.

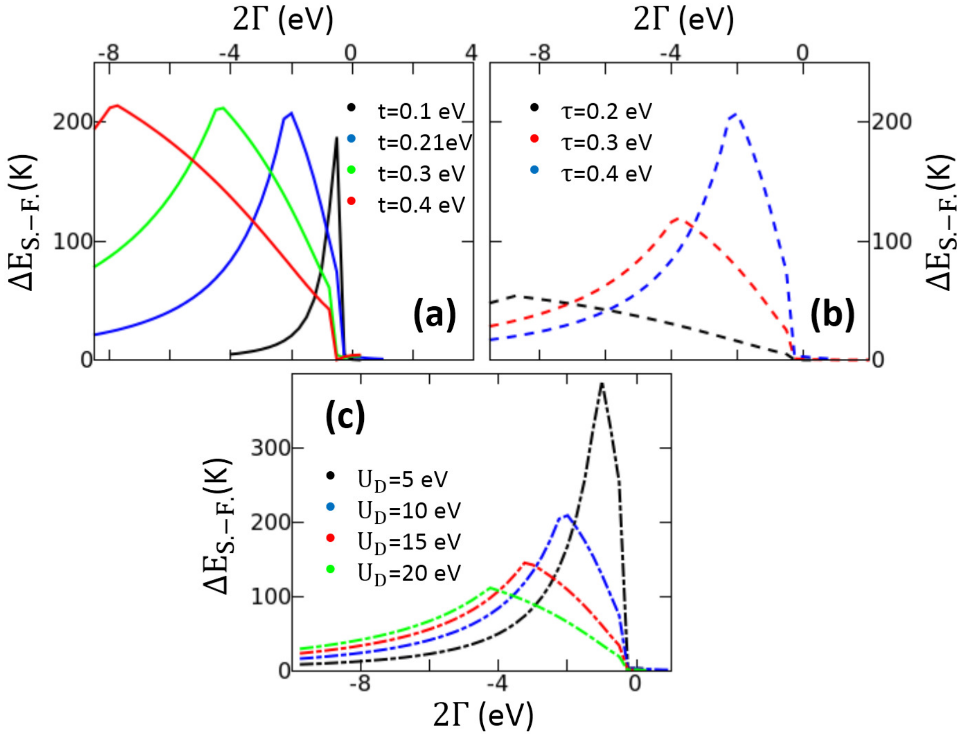

Figure 2.11: $\Delta E_{S.-F.}$ dependence on model parameters for a decorated mixed stack with N_c=4. (a) Energy difference between the lowest singlet state and the lowest quintet state as a function of 2Γ, setting $2z$=0.5 eV, τ=0.4 eV, U_D=10 eV and varying t. (b) $\Delta E_{S.-F.}$ vs 2Γ, setting $2z$=0.5 eV, t=0.21 eV, U_D=10 eV, for different τ values. (c) $\Delta E_{S.-F.}$ as a function of 2Γ, setting $2z$=0.5 eV, t=0.21 eV, τ=0.4 eV and varying U_D.

Similarly, the τ hopping value plays a fundamental role in stabilizing the ferrimagnetic correlations along the decorated stack, with modest τ values largely reducing $\Delta E_{S.-F.}$. As a consequence, it is important to design D-π-R$^\bullet$ dyads where the D and the R$^\bullet$ moieties are strongly conjugated. Indeed, the actual estimate of the τ hopping integral for the TTF-PTM$^\bullet$ dyad, introduced at the beginning of the Chapter, is ~0.1 eV, [125, 127] too small for achieving ferrimagnetic order, $\Delta E_{S.-F.}$ reducing to ~1 K. Finally, increasing the intermolecular t hopping one moves the maximum of $\Delta E_{S.-F.}$ away from the N-I phase boundary, deep into the I phase. On the contrary, a smaller t value reduces $\Delta E_{S.-F.}$ to a sharp peak close to the N-I interface together with an overall reduction of the ferrimagnetic stability region in the (2Γ,$2z$) plane.

2.1.3.2 Wave function delocalization

Because of strong correlations (i.e., $U/t \gg 1$), electrons are strongly bound to the molecular sites in large portions of the phase diagram shown in Fig.2.6. However, a partial electronic delocalization can be expected at the phase boundaries. To check this hypothesis, we calculate the modulus of the following complex quantity:[144, 145]

$$Z = Tr\{\hat{\rho} e^{i\frac{2\pi}{N_c}\hat{\mu}}\}, \tag{2.20}$$

where i is the imaginary unity and $\hat{\mu}$ is the component of the electric dipole moment operator along a regular open-boundary chain:

$$\hat{\mu} = \sum_{j=1}^{N_c} \Big[(2j-1)(\hat{\rho}_R + \hat{\rho}_D) + 2j\hat{\rho}_A\Big], \tag{2.21}$$

where $\hat{\rho}_{i,R} = 1 - \hat{n}_{i,R}$, $\hat{\rho}_{i,D} = 2 - \hat{n}_{i,D}$, $\hat{\rho}_{i,A} = -\hat{n}_{i,A}$, are the ionicity operators relevant to the i-th unit cell that measure the net charges on $\mathrm{R}^\bullet$, D and A molecular sites, respectively. The operator in Eq.2.21 is expressed in $e \cdot a$=1 units, a being the D-A distance, and the representative matrix is diagonal on the real-space basis, showing integer eigenvalues. It is important to notice that $\hat{\mu}$ in Eq.2.21 depends on the chosen reference system, whereas the complex quantity Z is fully independent of it, being defined modulo 2π. As it will be discussed in Sect.2.1.4, the imaginary part of the natural logarithm of Z gives the electronic polarization of a many-body quantum system with PBC.[49, 108, 142]

The modulus of Z is typically non-zero, its reciprocal being proportional to the delocalization of the wave function. As a consequence, $|Z|$ is expected to go to zero in systems having delocalized electrons. In Fig.2.12, $|Z|$ behavior at the three phase boundaries is shown. At the N-I interface (panel b), the system shows a metallic behavior. Similarly, a delocalized electronic state is observed while crossing the I-Z phase boundary (panel c), demonstrating that the electron transfer between A and R units induces an electron delocalization along the whole chain. On the other hand, the D-π-$\mathrm{R}^\bullet$ →$\mathrm{D}^{+\bullet}$-π-R^- intramolecular electron transfer takes place with no

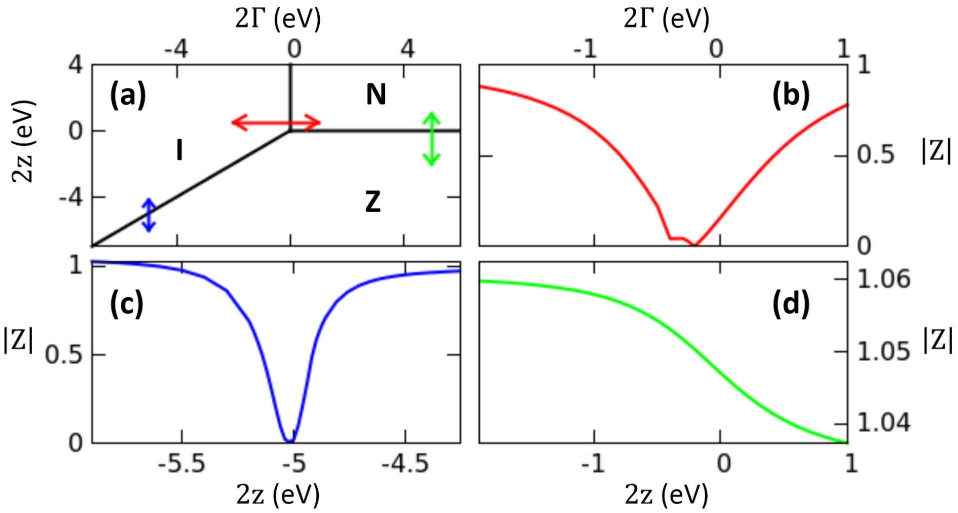

Figure 2.12: Wave function delocalization in a ring with N_c=4 (12 sites). (a) Phase diagram from Fig.2.6. (b) Modulus of Z against 2Γ for $2z$=0.5 eV. (c) $|Z|$ as a function of $2z$ for 2Γ=-5 eV. (d) $2z$-dependence of $|Z|$ having set 2Γ=5 eV. Double-head arrows in panel a highlight the energy ranges spanned within panels b, c and d (the same color is used for the arrow and the relevant $|Z|$ curve). Calculations done at 10 K, for the same parameters used in Fig.2.8.

wave function delocalization, $|Z|$ being finite across the whole N-Z interface (panel d).

2.1.4 Soft lattices

Strongly correlated electronic systems show complex phase diagrams with several electronic instabilities governed by competitive interactions.[146] These instabilities come with lattice deformations governed by the electron-vibration coupling. Within monodimensional metallic systems (i.e., setting Hubbard U=0), Peierls transition is the fundamental electron-lattice instability, the electron-vibration coupling being at the origin of the spontaneous lattice distorsion. On the other hand, strongly correlated systems (i.e., the $U \to \infty$ limit) boil down to Heisenberg antiferromagnets and undergo spin-Peierls transition occurring at lower temperatures.

Mixed stack CT crystals face the so-called generalized-Peierls transition.[108, 47, 26, 31, 142] Systems with a strongly ionic ground state turn into a spin chain, showing spin-Peierls transition with very low critical temperatures. Approaching the Neutral-Ionic phase boundary, charge degrees of freedom come into action together with increasing transition temperatures. At the Neutral-Ionic interface (if the phase transition is a continuous one) the system becomes metallic, thus showing a classical Peierls transition with transition temperatures that can be higher than the ambient temperature. Mixed stack dimerization has several practical consequences. In particular, regular mixed stack presents an inversion center on each molecular site that is lost in dimerized systems [108, 26] making them potentially ferroelectric.[108] Indeed, the actual crystal ferroelectricity depends on the relative orientation of different stacks. Anyhow, ferroelectric behaviour was confirmed in several mixed stack CT crystals, thus leading to molecular ferroelectric materials.[27, 113, 110, 21, 114]

The N and I phases of the decorated mixed stack (see Fig.2.6) correspond to the typical neutral and ionic phases of the mixed stack CT crystals. Therefore, the I phase is expected to show a lattice instability that, together with the ferrimagnetic correlations discussed in Sect.2.1.3, would lead to a multiferroic phase.

2.1.4.1 Electron-phonon coupling

Stack dimerization is governed by a zone-center lattice mode, corresponding to the in-phase displacement of all electron donor molecules against the fixed acceptor molecules (of course, what really matters is the relative displacement of the two sublattices). The dimerization mode induces an asymmetric modulation of the inter and intra-cell t hopping integrals. Assuming the Su-Schrieffer-Heeger linear dependence of t on the lattice displacement, [147] dimerization enters the Hamiltonian through a slow variable, namely the dimerization amplitude, δ, as already expressed by the third and fourth lines in Eq.2.2.[49, 31, 47, 142]

The energetic cost for the lattice distortion is expressed using an elastic term (last term in Eq.2.2), that summed to the electronic energy, $\mathcal{E}_{el}$, gives the system total energy, $\mathcal{E}_{tot}$:

$$\mathcal{E}_{tot} = \mathcal{E}_{el} + N_c t^2 \frac{\delta^2}{2\varepsilon_d}. \tag{2.22}$$

Systems with strong electron-phonon coupling have large ε_d values, thus describing soft lattices that can be easily deformed, whereas stiff lattices are described in terms of small ε_d values. Results shown in this Section are obtained by setting ε_d=0.04 eV, in line with typical values for mixed stack CT crystals.[26, 31, 47]

In the N phase (ρ <0.5) as well as in the $\rho \rightarrow 1$ limit, the regular stack is stable, while close to the N-I interface the stack becomes unstable towards dimerization, the inversion symmetry is lost and a double minimum appears in the ground state total energy. This is shown in Fig.2.13, panel a, where $\mathcal{E}_{tot}$ is reported against δ for 2Γ=-0.368 eV $\wedge$ $2z$=0.5 eV. The two equivalent minima determine the equilibrium dimerization amplitude, δ_{eq}, whereas the barrier heigth gives an estimate of the dimerization stability temperature, T_d.[26, 142] In Fig.2.13, panel b, the equilibrium dimerization amplitude, δ_{eq}, calculated for the ground state of rings with N=12, 18 is shown as a function of 2Γ, having set $2z$=0.5 eV, and further confirms the scenario mentioned above: a non-zero δ_{eq} is obtained near to the N-I interface, with δ_{eq} reaching values as large as $\simeq$0.18, while δ_{eq}=0 is observed for both $2\Gamma > 0 \wedge 2\Gamma \ll 0$. The 2Γ-dependence of the dimerization temperature, T_d, for a ring with N_c=6 is reported in Fig.2.13, panel c, as a blue filled curve (relevant results for a ring with N_c=4 are also shown as a blue dotted curve). In the same panel, the orange area marks the stability region of the ferrimagnetic correlations; more precisely, results calculated with and without the electron-phonon coupling are shown as continuous and dashed orange curves, respectively (results for a ring with N_c=4 are reported as dotted and dash-dotted orange curves, respectively). The small, but not negligible lattice dimerization (Fig.2.13, panel b) is not strong enough to completely break the ferrimagnetic order down. Indeed, even if $\Delta E_{S.-F.}$ calculated for the equilibrium dimerization amplitude is reduced with respect to that relevant to the regular stack, a region with a ferrimagnetic dimerized stack survives (green area in panel c), thus pointing to a potentially multiferroic phase showing both ferrimagnetic and ferroelectric orders.

To demonstrate ferroelectric behavior, we calculate the polarization, P. The electric polarization within a system with PBC is defined in terms of the Berry phase. More precisely, using the complex quantity Z defined in

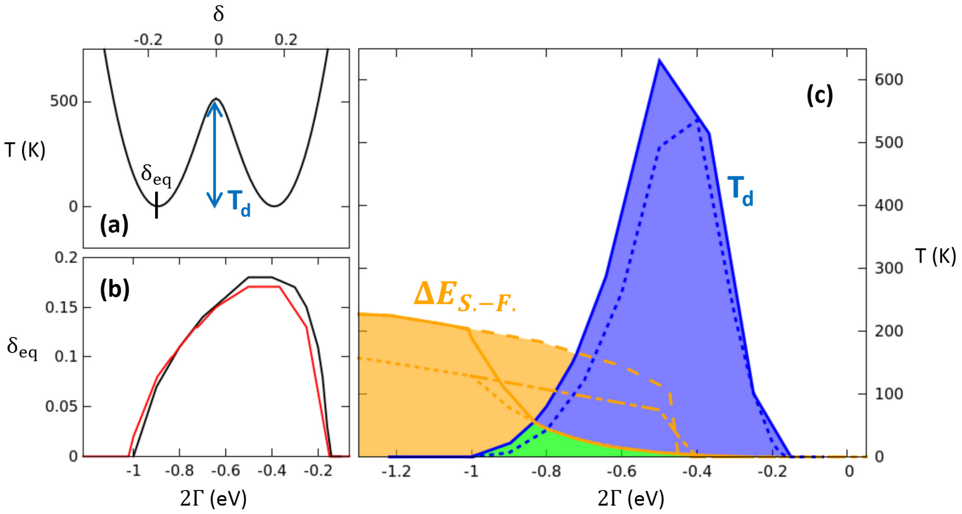

Figure 2.13: The effect of the electron-phonon coupling. (a) Ground state total energy, $\mathcal{E}_{tot}$, in Kelvin as a function of the dimerization amplitude, δ, for a ring with N_c=6, setting 2Γ=-0.368 eV $\wedge$ $2z$=0.5 eV. (b) Equilibrium dimerization amplitude against 2Γ, having set $2z$=0.5 eV, for rings with N_c=4 (black curve) and 6 (red curve). (c) Dimerization temperature against 2Γ for a ring with N_c=6 (blue filled curve) and 4 (blue dotted curve), together with $\Delta E_{S.-F.}$ for a ring with N_c=6 (orange continuous and dashed curves, for soft and stiff lattices, respectively) and 4 (orange dotted and dash-dotted curves, for soft and stiff lattices, respectively). Calculations done for the same parameters used in Fig.2.8.

Eq.2.20, P reads:[49, 108, 142]

$$P \quad = \quad \frac{1}{2\pi} Tr\Big\{\hat{\rho}\Big(Im[log(Z)]\Big)\Big\}, \tag{2.23}$$

where $\hat{\rho}$ was defined in Eq.2.14, while the modulus of Z as a function of 2Γ for a dimerized stack is shown in Fig.2.14, left panel. The electric dipole moment in Eq.2.21 can be redefined in order to account for the finite dimerization amplitude:[49]

$$\hat{\mu} \quad = \quad \sum_{j=1}^{N_c} \left[\left(2j - 1 + \frac{\delta_{eq}}{2\tilde{\alpha}}\right)(\hat{\rho}_R + \hat{\rho}_D) + \left(2j - \frac{\delta_{eq}}{2\tilde{\alpha}}\right)\hat{\rho}_A\right], \tag{2.24}$$

where $\tilde{\alpha} = a\sqrt{K\varepsilon_d}/t$, with K being the dimerization mode force constant, while all the other quantities were defined in Subsect.2.1.3.2. Results at 10

K shown in Fig.2.14 are obtained setting $\tilde{\alpha}$=5, as relevant to CT crystal TTF-CA.[49]

Experimentally, it is not possible to measure the absolute value of the electric polarization, but rather its variations. This is consistent with the definition of P given in Eq.2.23 as the imaginary part of the natural logarithm of the complex quantity Z, that is a periodic function with period equal to one. Within Fortran programming language the principal value logarithm of a complex number is used; more precisely, if $c \in \mathbb{C}$, then $log(c) = log|c| + i\ arg(c)$, where $-\pi < arg(c) \leq \pi$. Consequently, from Eq.2.23 follows $P \in\ ]\text{-}0.5, 0.5]$ as also shown in Fig.2.14, right panel. As expected, for $2\Gamma <$ -1 eV $\vee$ $2\Gamma > 0$, no electric response is observed, the stack being regular (δ_{eq}=0) and with a trivial Berry phase (i.e., equal to 0 or π). On the other hand, close to the N-I crossover, the stack dimerizes ($\delta_{eq} \neq$0) and the inversion symmetry is lost. As a result, the geometrical phase gets non-trivial values and a finite P appears. The maximum P value (i.e., ±0.5) is reached close to the N-I phase boundary, corresponding to a dimensional value of $\sim$ 14 μC/cm^2, that is more than one order of magnitude larger than the experimentally observed value for CT crystal TTF-BA (BA=bromanil).[23]

2.2 Decorated segregated stack

2.2.1 The model

The MPTTF-PTM molecule (Fig.2.3, panel a) is a prototypical CT dipolar chromophore, with the D group (MPTTF) connected through a π-conjugated bridge to the electron acceptor, R$^\bullet$, group (PTM).[132] Consequently, MPTTF-PTM physics is well captured within an essential two-state model (Sect.1.2.1), simply accounting for HOMO on D and LUMO on R$^\bullet$ sites. Indeed, having 3 valence electrons, the dyad can assume two states, and the relevant Hamiltonian matrix reads:

$$\begin{aligned}\hat{h} &= \varepsilon_D \hat{n}_D + \varepsilon_R \hat{n}_R \\ &\quad + U_D \hat{n}_{D,\uparrow} \hat{n}_{D,\downarrow} + U_R \hat{n}_{R,\uparrow} \hat{n}_{R,\downarrow} \\ &\quad - \tau \sum_\sigma (\hat{c}^\dagger_{D,\sigma} \hat{c}_{R,\sigma} + H.c.), \end{aligned} \tag{2.25}$$

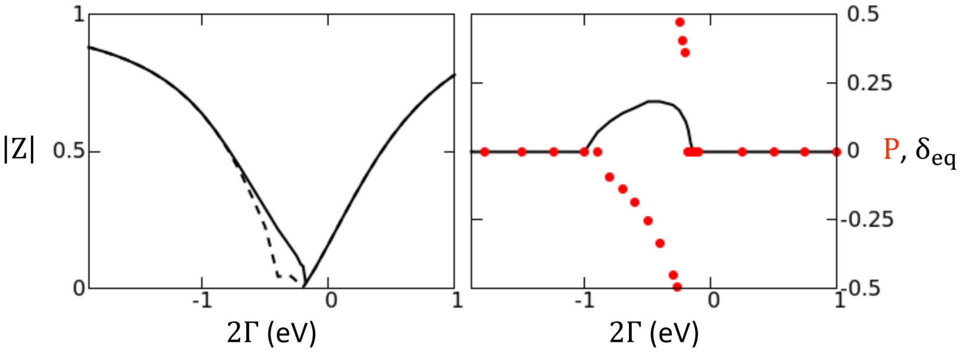

Figure 2.14: Electron delocalization and electric polarization in a dimerized stack. Left panel: 2Γ-dependence of the modulus of the complex quantity Z defined in Eq.2.20 for a dimerized stack (continuous black curve) and for a regular chain (dashed black curve). Right panel: Electric polarization, P, (red filled dots) and equilibrium dimerization amplitude, δ_{eq}, (black curve) as a function of 2Γ. Calculations performed at 10 K for a ring with N_c=4, setting $2z$=0.5 eV. Same parameters used in Fig.2.8.

where ε_D and ε_R are the D and R$^\bullet$ site energies, respectively, while U_D and U_R are the relevant on-site Coulomb repulsion energies. The electron delocalization determined by the IET process is described by the third line of the expression. It is useful to introduce the auxiliary quantity $2z{=}\varepsilon_R - \varepsilon_D - U_D + U_R$, measuring the energy involved in the IET process, D-π-R$^\bullet$ →D$^{+\bullet}$-π-R$^-$. The MPTTF-PTM segregated stack crystal in Fig.2.3, panel b, combines IET with CT.[132] Focusing on the D and R$^\bullet$ frontier orbitals of a N-membered single stack, the problem consists in distributing $3N$ electrons on $2N$ sites. The stack is described in terms of a modified Hubbard model, thus accounting for different site energies, and reads:

$$\hat{H}_{stack} = \sum_i \hat{h}_i - t\sum_{i,\sigma}(\hat{c}^\dagger_{i,D,\sigma}\hat{c}_{i+1,D,\sigma} + H.c.), \tag{2.26}$$

where i runs over the N molecules constituting the stack, $\hat{h}_i$ being the i-th single dyad Hamiltonian introduced in Eq.2.25, whereas σ runs on the two possible spin polarizations. The t hopping term accounts for the electron delocalization along the monodimensional stack. Periodic boundary conditions are adopted.

Following the numerical approach discussed in Sect.2.1.2, the stack Hamiltonian is written on the real-space basis set, each basis function being an electronic configuration written in the bit representation. Because of CT degrees of freedom, several electronic configurations are possible, thus leading to a huge number of basis states. Working in the ($\varepsilon_D - \varepsilon_R$, U_R)$\rightarrow \infty$ limit, in analogy to Sect.2.1.2.2, the number of relevant states can be reduced neglecting all those configurations with R^+ sites.

Exploiting spin symmetry, the Hamiltonian can be diagonalized within different S_z spin sectors. Working with an even number of dyads (typically, N=4, 6), S_z=0 is the only significant spin space, its reduced dimension dramatically increasing from 594 to 31730, while moving from N=4 to 6. Adopting the CSR format in the 3-array variation, very efficient diagonalization routines from ARPACK library can be used to attack the problem.

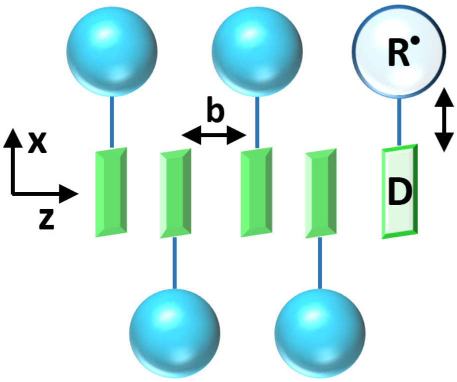

Figure 2.15: Sketch of the decorated segregated stack. Both the intermolecular, b, and intramolecular, a, effective distances are set equal to 3.7 Å as relevant to MPTTF-PTM crystal reported in Fig.2.3, panel b.[132]

The Hamiltonian eigenvalues and eigenvectors can be used to calculate the electronic spectra for D-π-R$^\bullet$ chains with N=4, 6, accounting for an electric field polarized along z and x axes (Fig.2.15), considering both ionic ($2z$<0) and neutral ($2z$>0) stacks. The x-component of the electric dipole operator, $\hat{\mu}_x$, is not affected by periodic boundary conditions and reads:

$$\hat{\mu}_x = a \sum_j (-1)^j \hat{\rho}_{j,R}, \tag{2.27}$$

where the sum runs over the N dyads, $\hat{\rho}_{j,R} = 1 - \hat{n}_{j,R}$ is R$^\bullet$ ionicity operator, while a is set equal to 3.7 Å as relevant to MPTTF-PTM effective bond length (Fig.2.15).[132] The alternating sign in the expression accounts for the radical relative orientation along the stack, where x axis origin is put on MPTTF fragment.

The z-component of the electric dipole operator, $\hat{\mu}_z$, can be defined only for an open chain and reads:

$$\hat{\mu}_z = b \sum_j j \Big(\hat{\rho}_{j,R} + \hat{\rho}_{j,D} \Big), \tag{2.28}$$

where $\hat{\rho}_{j,D} = 2 - \hat{n}_{j,D}$ measures the charge on the D site, whereas b=3.7 Å is the intermolecular effective distance (Fig.2.15).[132] Both $\hat{\mu}_x$ and $\hat{\mu}_z$ are diagonal on the real-space basis and once rotated on $\hat{H}_{stack}$ eigenvectors, can be used to calculate the polarized oscillator strength.

For the generic $|f\rangle \leftarrow |i\rangle$ transition, where both $|i\rangle$ and $|f\rangle$ are $\hat{H}_{stack}$ eigenvectors, the oscillator strength is the following (dimensionless) quantity:

$$f^{x(z)}_{f\leftarrow i} = \frac{2m_e}{e^2\hbar} \omega_{fi} \Big| \mu^{x(z)}_{fi} \Big|^2, \tag{2.29}$$

where m_e is the electron mass, $\omega_{fi} = (\mathcal{E}_f - \mathcal{E}_i)/\hbar$ is the transition frequency and $\mu^{x(z)}_{fi} = \langle f | \hat{\mu}_{x(z)} | i \rangle$ is the relevant transition dipole moment.

Dealing with a chain closed into a ring, Eq.2.28 is no more valid being incompatible with the system rotational symmetry. Consequently, the velocity dipole operator is introduced:[148, 141, 149]

$$\begin{aligned} \hat{v} &= \frac{i}{\hbar} [\hat{H}_{stack}, \hat{\mu}_z] \\ &= -i \frac{etb}{\hbar} \sum_{j,\sigma} \Big(\hat{c}^\dagger_{j,D,\sigma} \hat{c}_{j+1,D,\sigma} - H.c. \Big), \end{aligned} \tag{2.30}$$

where j runs over the N dyads and σ over the two spin polarizations. The $\hat{v}$ operator is not diagonal on the real-space basis and once written on $\hat{H}_{stack}$ eigenvectors, it can be used to calculate the oscillator strength along the ring:[148]

$$f^z_{f\leftarrow i} = \frac{2m_e}{e^3} \frac{t^2 b^2}{\hbar^2} \frac{|v_{fi}|^2}{\hbar\omega_{fi}}, \tag{2.31}$$

where v_{fi}=$\langle f | \hat{v} | i \rangle$. In the following, for practical reasons, a Gaussian shape with FWHM=0.06 eV will be assigned to each transition.

2.2.2 Calculated spectra

We start with an isolated D-π-R$^\bullet$ molecule, as described in Eq.2.25. Results are independent of U_D, but are strongly dependent on $2z$. For negative $2z$, zwitterionic D$^{+\bullet}$-π-R$^-$ molecules are expected, while for positive $2z$, we expect neutral dyes. If τ is not too large (we set τ=0.1 eV in line with the current estimate for TTF-PTM dyad [125, 127]), in either case an optical absorption is expected at energy $\sim |2z|$, associated with IET degrees of freedom (Fig.2.16, left panel).

Results obtained for stacks containing 4 to 6 dyads, assuming periodic boundary conditions (rings), are discussed in the following. Different $2z$ values are used in order to study stacks with either neutral ($2z>0$) or ionic ($2z<0$) character. Moreover, the on-site Coulomb repulsion, U_D, is typically set to 1.29 eV, [125] being the relevant value within TTF$^{+\bullet}$ chains, whereas t=0.05 eV is estimated from ZINDO calculations on a (MPTTF-PTM)$_2$ dimer in its crystallographic geometry.[132]

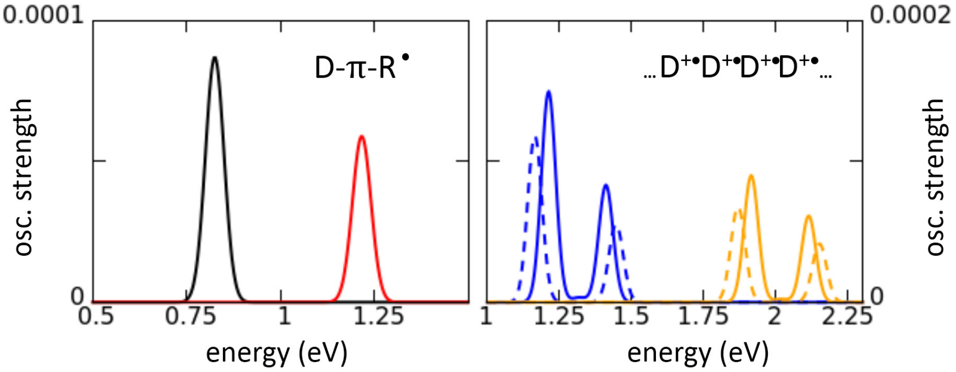

Figure 2.16: Results for an isolated D-π-R$^\bullet$ dyad and for an half-filled Hubbard chain. Left panel: Oscillator strength against transition energy (in eV) along the x (molecular) axis, for a single dyad for two different values of the IET energy, namely $|2z|$=0.8 eV (black curve) and $|2z|$=1.2 eV (red curve). Intramolecular hopping integral τ=0.1eV and N=4. Right panel: Oscillator strength vs transition energy (in eV) along the z (stack) axis, for D$^{+\bullet}$ chain (i.e., τ=0 in Eq.2.26) for rings with N=4 (dashed curves) and 6 (continuous curves), for U_D=1.29 eV (blue curves) and 2 eV (orange curves). Intermolecular hopping integral t=0.05 eV.

2.2.2.1 Ionic MPTTF-PTM chains

The discussion can start from the half-filled Hubbard $D^{+\bullet}$ chain as obtained by switching off the τ hopping integral in Eq.2.26. The oscillator strength along the stack axis of rings with N=4, 6 is calculated using Eq.2.31 (Fig.2.16, right panel). The expected single peak at $\sim U_D$, signature of the $D^{+\bullet}$-$D^{+\bullet} \rightarrow D^{2+}$-D process, [150] is split into a doublet centered at U_D (results for U_D=1.29 eV and 2 eV are shown as blue and orange curves, respectively). However, calculations performed on rings with N=4 (dashed curves) and 6 (continuous curves) suggest this being a finite size effect, the splitting appreciably reducing while increasing N.

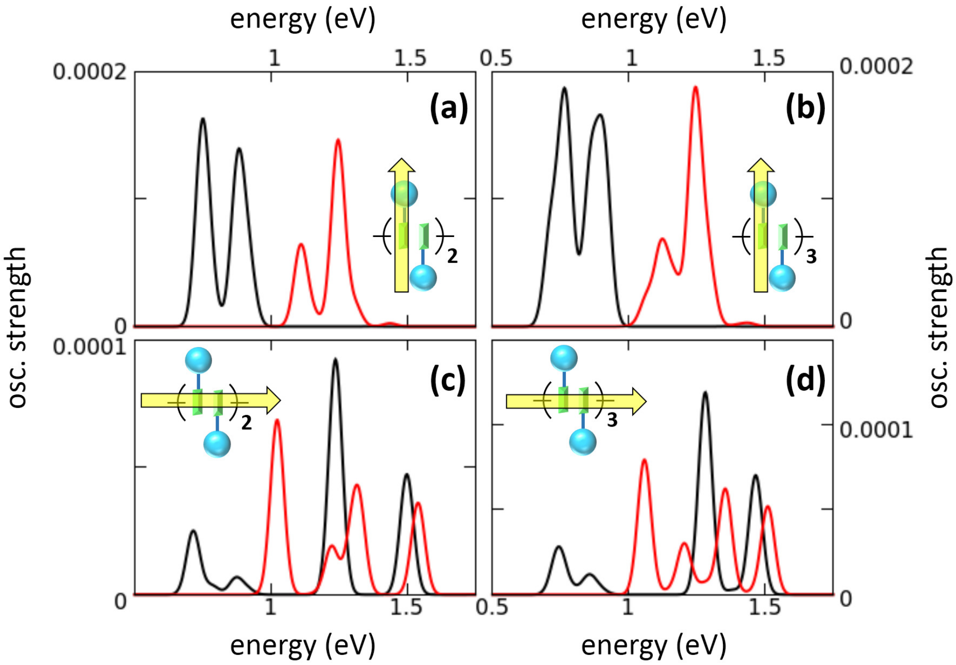

Figure 2.17: Intra and intermolecular charge transfer effects on the oscillator strength in the $D^{+\bullet}$-π-R^- stack. Oscillator strength vs transition energy (in eV) along x axis (upper panels) and z axis (lower panels) for rings with N=4 (panels a and c) and 6 (panels b and d). Black and red curves are obtained for $2z$=-0.8 eV and -1.2 eV, respectively. Other parameters: t=0.05 eV, τ=0.1 eV, U_D=1.29 eV.

Switching on the D-π-$R^\bullet$ intramolecular interaction (τ=0.1 eV), the energy dependence of the oscillator strength calculated for two different $2z$ values and along two different polarizations (z and x axes) is reported in Fig.2.17 for rings with N=4 (left panels) and 6 (right panels). In this parameter regime, absorption spectra become more complex, with signatures coming from both intra and intermolecular charge transfer degrees of freedom.

Focusing on the multiplets shown in panels c and d for two different $2z$ values, the Hubbard exciton (D^{2+}-D) signal is visible as a doublet at $\sim U_D$. At energy $\sim |2z|$, another band, split into two peaks, can be associated to the intramolecular charge transfer process as also suggested by the spectra calculated using an electric field polarized along the molecular bond (panels a and b).

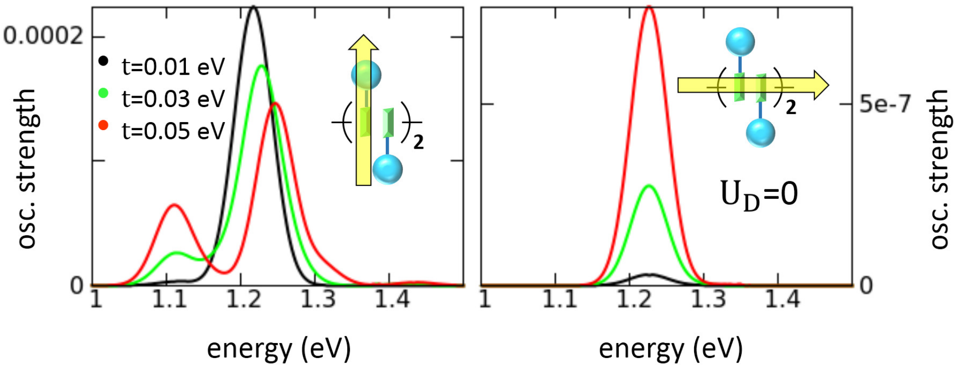

Figure 2.18: The effect of an increasing t hopping integral on the intramolecular charge transfer signal in an ionic ring with N=4. In particular, oscillator strength vs energy in eV, along the x axis (left panel) and the z axis (right panel) calculated for three different values of t. Parameters used: $2z$=-1.2 eV, τ=0.1 eV. In the left panel, U_D=1.29 eV. In the right panel, U_D=0.

In Fig.2.18, the effect of increasing the t hopping integral on the intramolecular charge transfer signal is shown. Normally to the stack axis (left panel), slight changes in the intermolecular hopping probability strongly affect the band shape and for t=0.03 eV (green curve) the IET peak is split into a doublet. A further increment in the electronic kinetic energy along the stack, t=0.05 eV (red curve), brings back to the complex signal reported as a red curve in Fig.2.17, panel a. On the other hand, looking along the stack (right panel) and putting to zero U_D, the weak IET peak intensity gradually increases while increasing t. Switching on U_D, the red curve gains intensity and becomes that reported in Fig.2.17, panel c.

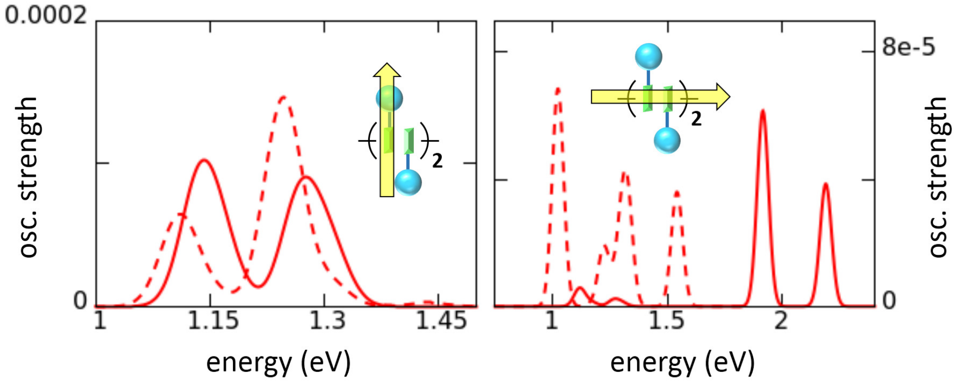

Figure 2.19: The effect of U_D on the polarized oscillator strength within an ionic ring with N=4. Results for U_D=1.29 eV (dashed line) and U_D=2 eV (continuous line) along the x axis (left panel) and the z axis (right panel). Same other parameters as in Fig.2.17.

Finally, the complex spectrum reported for $2z$=-1.2 eV in Fig.2.17, panel c, can be made more clear by changing the U_D value, in order to avoid all the bands falling in the same spectral region; for example, setting U_D=2 eV, the Hubbard exciton signal is moved to a different energy region respect to the IET, whose intensity is strongly decreased respect to the case with a lower U_D value (Fig.2.19, right panel). Moreover, looking along the dyad bond direction, changing U_D causes a slight change in the band shape (Fig.2.19, left panel).

2.2.2.2 Neutral MPTTF-PTM chains

In analogy with the ionic chain, making several (4 or 6) neutral D-π-R$^\bullet$ molecules mutually interacting (i.e., setting t=0.05 eV), a neutral stack is obtained. Setting τ=0 and U_D=1.29 eV, the oscillator strength along the stack axis is zero, being all the D sites completely filled, with no possibility of intermolecular hopping. Switching on the intramolecular hopping (i.e., $\tau \neq 0$), the situation along x and z axes completely changes.

If t is small compared to $2z$, the problem can be treated perturbatively.

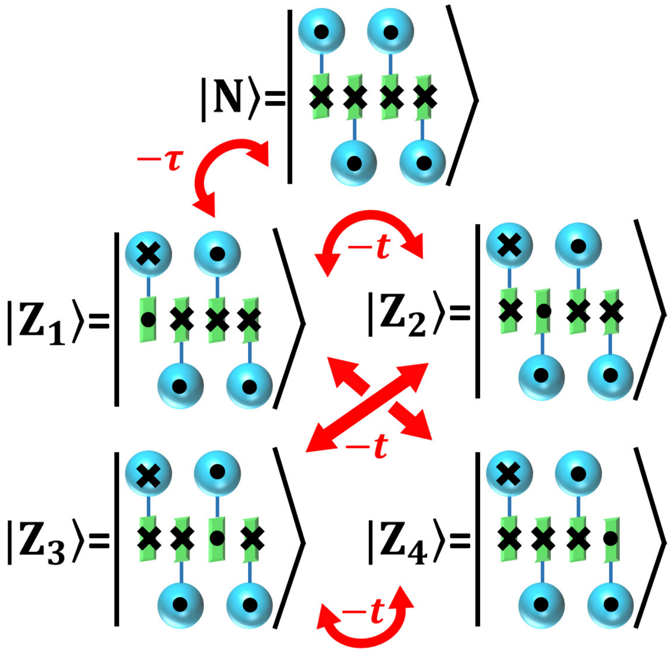

Figure 2.20: Sketch of the basis functions relevant to the neutral D-π-R$^\bullet$ ring with N=4 (spin degeneracy is neglected). Black dot: one electron; cross: two electrons.

The neutral stack electronic ground-state is mainly represented by a configuration where all the donor sites are doubly occupied and all the acceptor sites are singly occupied. This neutral configuration is called $|N\rangle$ in Fig.2.20. Because of τ hopping integral, $|N\rangle$ is perturbed by partially ionic configurations, generated through both intra and intermolecular charge transfer processes; for a ring with N=4, there are four possible partially ionic degenerate configurations, namely $|Z_i\rangle$, for i=1,..., 4, (and, of course, for each of them, their translational equivalent version), that are mixed by t (Fig.2.20).

The stack Hamiltonian in Eq.2.26 written on the reduced 5-fold Hilbert space thus reads:

$$\hat{H}^{N=4}_{2z>0} = \left(\begin{array}{c|cccc} 0 & -\sqrt{2}\tau & 0 & 0 & 0 \\ \cline{2-5} -\sqrt{2}\tau & 2z & -t & 0 & -t \\ 0 & -t & 2z & -t & 0 \\ 0 & 0 & -t & 2z & -t \\ 0 & -t & 0 & -t & 2z \end{array} \right). \qquad (2.32)$$

Diagonalizing the highlighted 4×4 block spanned by $|Z_i\rangle$ functions, the Hamiltonian becomes:

$$\hat{H}'^{N=4}_{2z>0} = \left(\begin{array}{c|cccc} 0 & -\tau/\sqrt{2} & -\tau/\sqrt{2} & -\tau/\sqrt{2} & -\tau/\sqrt{2} \\ \cline{2-5} -\tau/\sqrt{2} & 2z-2t & 0 & 0 & 0 \\ -\tau/\sqrt{2} & 0 & 2z & 0 & 0 \\ -\tau/\sqrt{2} & 0 & 0 & 2z & 0 \\ -\tau/\sqrt{2} & 0 & 0 & 0 & 2z+2t \end{array} \right). \qquad (2.33)$$

Expanding the basis functions spanning Eq.2.33 up to the first order in τ, transition dipole moments along x and z directions can be estimated. In particular, transitions towards the two degenerate states at $\sim 2z$ are allowed along both x and z directions, whereas states at $\sim 2z \pm 2t$ have a finite oscillator strength only along the x axis. Consequently, in a ring with N=4, a triplet, with $\sim 2t$ peak separation, should be visible along the D-π-R$^\bullet$ bond, while a single band should appear using an electric field polarized along the stack. Indeed, this is exactly the situation found in Figure 2.21, left panels, where, along the x axis, the band at $2z$ is splitted into three peaks separated by an energy $\sim 2t$ (panel a), whereas, looking along the stacking direction, a single peak is centered at $2z$ energy (panel c).

Analogously, for a ring with N=6, a reduced 7-fold Hilbert space can be defined, with the stack Hamiltonian reading:

$$\hat{H}^{N=6}_{2z>0} = \left(\begin{array}{c|cccccc} 0 & -\sqrt{3}\tau & 0 & 0 & 0 & 0 & 0 \\ \cline{2-7} -\sqrt{3}\tau & 2z & -t & 0 & 0 & 0 & -t \\ 0 & -t & 2z & -t & 0 & 0 & 0 \\ 0 & 0 & -t & 2z & -t & 0 & 0 \\ 0 & 0 & 0 & -t & 2z & -t & 0 \\ 0 & 0 & 0 & 0 & -t & 2z & -t \\ 0 & -t & 0 & 0 & 0 & -t & 2z \end{array} \right). \qquad (2.34)$$

Diagonalization of the highlighted 6×6 block spanned by $|Z_i\rangle$, for i=1,..., 6,

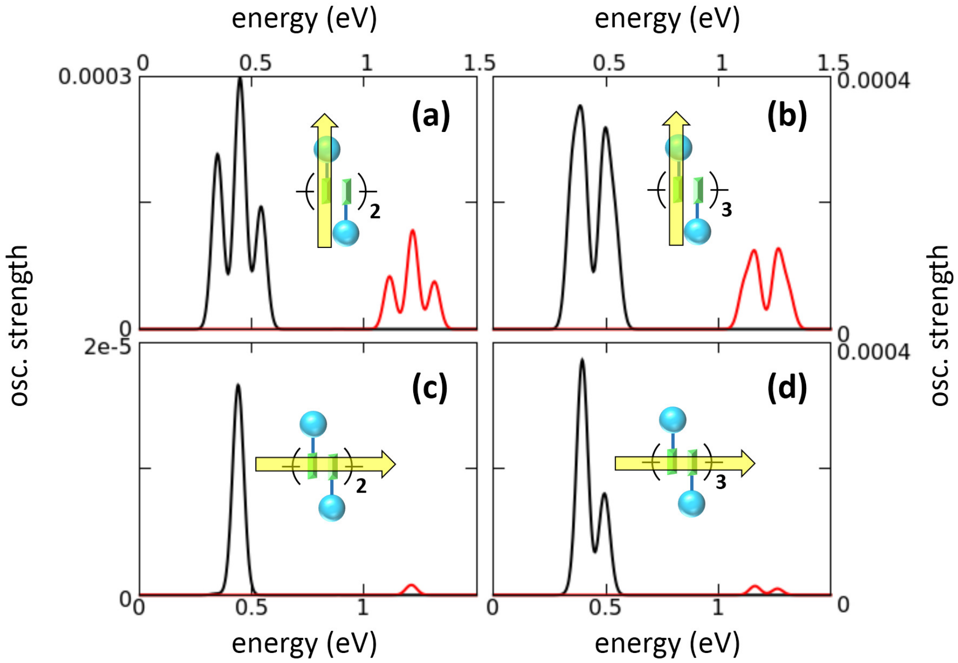

Figure 2.21: Neutral D-π-R$^\bullet$ ring with N=4 (left panels) and 6 (right panels). Oscillator strength vs transition energy (in eV) calculated along x (panels a and b) and z axes (panels c and d), for $2z$=0.4 eV (black curve) and 1.2 eV (red curve). Other parameters are those used in Fig.2.17.

leads to the following Hamiltonian:

$$\hat{H}'^{N=6}_{2z>0} = \left(\begin{array}{c|cccccc} 0 & -\tau/\sqrt{2} & \tau\sqrt{3}/2 & -\tau/2 & -\tau\sqrt{3}/2 & -\tau/2 & -\tau/\sqrt{2} \\ \hline -\tau/\sqrt{2} & 2z-2t & 0 & 0 & 0 & 0 & 0 \\ \tau\sqrt{3}/2 & 0 & 2z-t & 0 & 0 & 0 & 0 \\ -\tau/2 & 0 & 0 & 2z-t & 0 & 0 & 0 \\ -\tau\sqrt{3}/2 & 0 & 0 & 0 & 2z+t & 0 & 0 \\ -\tau/2 & 0 & 0 & 0 & 0 & 2z+t & 0 \\ -\tau/\sqrt{2} & 0 & 0 & 0 & 0 & 0 & 2z+2t \end{array}\right).$$

The doublet in Fig.2.21, panel b, is a doublet of doublets (indeed, a shoulder for both peaks can be perceived) and is mainly due to the transition towards the two couples of doubly degenerate states (at energies $\sim 2z \pm t$) as well as towards the two states at $\sim 2z \pm 2t$ energies. On the other hand, the two peaks separated by $\sim 2t$ energy in panel d, correspond to the transitions towards the two couples of degenerate states. Of course, if t becomes too big with respect to $2z$, the perturbative treatment breaks down and the spectra become more complex.

2.2.2.3 The effect of long-range electrostatic interactions

The stack model Hamiltonian in Eq.2.26 can be extended in order to account for long-range Coulomb interactions:[30, 47]

$$\hat{H}(V) \quad = \quad \hat{H}_{stack} + V \sum_{i} \hat{\rho}_{i,D} \hat{\rho}_{i,R}, \tag{2.35}$$

where V is the interaction strength, the sum runs over the N stack molecules and only interactions between D and R sites residing on the same dyad are accounted for (see sketch in Fig.2.22, panel a).

For the sake of simplicity and being MPTTF-PTM segregated stack (Fig.2.3, panel b) a neutral CT crystal, [132] the effect of electrostatic interactions on the polarized oscillator strength will be addressed only within neutral ($2z$ >0) stacks.

Looking at Eq.2.35, it is clear that function $|Z_1\rangle$ in Fig.2.20 is indeed lower in energy respect to the other three partially ionic diagrams; as a result, Eq.2.32 can be rewritten as:

$$\hat{H}^{N=4}_{2z>0}(V) = \left(\begin{array}{cc|ccc} 0 & \multicolumn{1}{c}{-\sqrt{2}\tau} & 0 & 0 & 0 \\ -\sqrt{2}\tau & \multicolumn{1}{c}{2z - V} & -t & 0 & -t \\ \cline{3-5} 0 & -t & 2z & -t & 0 \\ 0 & 0 & -t & 2z & -t \\ 0 & -t & 0 & -t & 2z \end{array} \right). \tag{2.36}$$

Mixing the degenerate partially ionic basis functions spanning the 3×3 highlighted block, the matrix becomes:

$$\hat{H}'^{N=4}_{2z>0}(V) = \left(\begin{array}{cc|ccc} 0 & \multicolumn{1}{c}{-\sqrt{2}\tau} & 0 & 0 & 0 \\ -\sqrt{2}\tau & \multicolumn{1}{c}{2z - V} & -t & 0 & t \\ \cline{3-5} 0 & -t & 2z - t\sqrt{2} & 0 & 0 \\ 0 & 0 & 0 & 2z & 0 \\ 0 & t & 0 & 0 & 2z + t\sqrt{2} \end{array} \right). \tag{2.37}$$

If off-diagonal terms in Eq.2.37 are small with respect to the diagonal ones, using a perturbative approach, the basis states can be expanded up to the

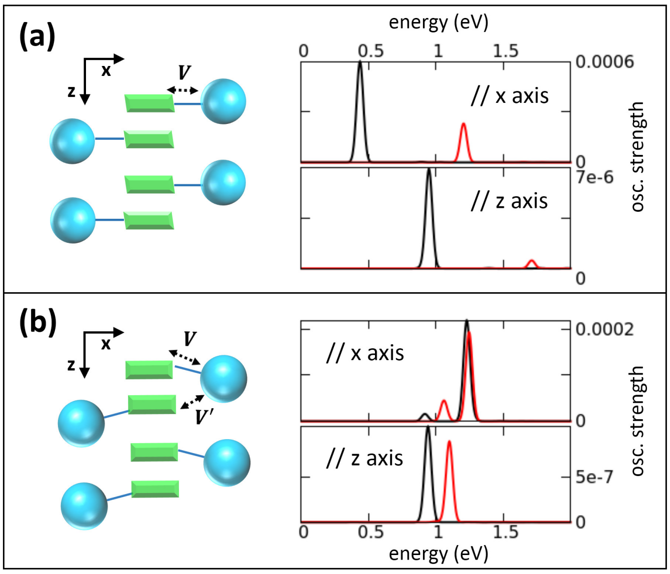

Figure 2.22: Intra and intermolecular electrostatic interactions affecting the oscillator strength in a D-π-R$^\bullet$ neutral ring with N=4. (a) Polarized oscillator strength calculated for an intramolecular electrostatic interaction V=0.5 eV (see sketch on the left), for $2z$=0.4 eV (black curve) and 1.2 eV (red curve). (b) Effect of two different long-range electrostatic interactions, V and V' (see sketch on the left), on the polarized oscillator strength. Results shown for $2z$=1.2 eV and V=0.5 eV, setting V'=0.6 eV (red curve) and 0.75 eV (black curve). In both panels a and b, $2z$ is rescaled to $2z+V$. Other parameters: t=0.05 eV, τ=0.1 eV, U_D=1.29 eV.

first order in t and τ and the relevant transition dipole moments along x and z axes can be calculated.

Calculated polarized oscillator strengths are shown in Fig.2.22, panel a. Because of V, the x-polarized triplet centered at $2z$ reported in Fig.2.21, panel a, is now reduced to a single peak corresponding to a localized IET process. This is also confirmed by the oscillator strength calculated along the stack, where a very weak signal is observed at $\sim 2z + V$. In order to make the exciton more delocalized along the chain, one can introduce a further interaction term, $V' \sum_i \hat{\rho}_{i,R}\hat{\rho}_{i+1,D}$, between R and D units belonging to adjacent dyads as reported in the sketch in Fig.2.22, panel b. In the same panel, polarized oscillator strengths are shown for two different values of

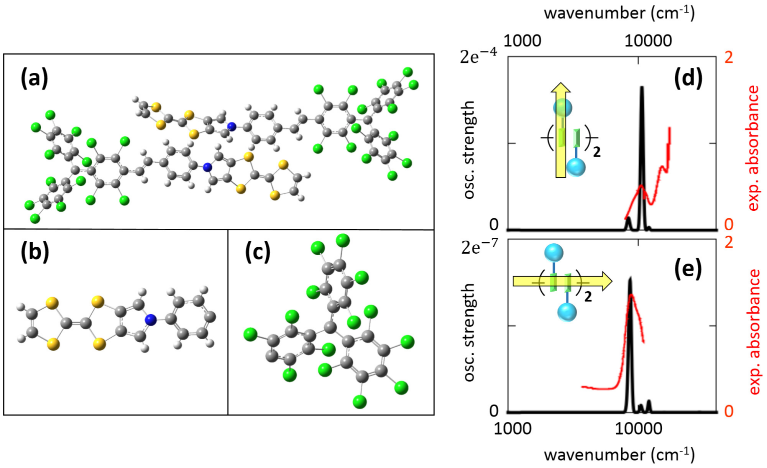

Figure 2.23: Long-range Coulomb interactions using DFT electrostatic potential (ESP) charges and comparison with the experimental data from Ref.[132]. (MPTTF-PTM)$_2$ dimer in the crystallographic geometry (panel a), together with D (panel b) and R (panel c) fragments used to estimate long-range electrostatic interactions (atom color legend: sulfur in yellow, carbon in grey, chlorine in green, nitrogen in blue). Calculated oscillator strength (black curve) together with experimental polarized absorption spectra (red curve) in panels d and e. Notice the logarithmic wave number scale. Calculation done for a MPTTF-PTM ring with N=4, using long-range electrostatic interactions in Tab.2.2. Other parameters: t=0.05 eV, τ=0.1 eV, U_D=1.29eV, $2z$=1.3 eV. U_D is rescaled to $U_D + V_{Dj,Dj+1}$.

V', while keeping fixed V and $2z$ values. The strong peak associated with the localized exciton is still visible along the x direction, together with a lower energy weaker band that gets intensity along the stack axis too and that can be associated with the delocalized excitation. Indeed, the modulus of the complex quantity Z in Eq.2.20 estimated on the stack ground state moves from ~0.72 (V'=0) to ~0.4 (V'=0.6 eV), the electrons becoming more delocalized along the chain.

Furthermore, using electrostatic potential (ESP) charges calculated at DFT level ((U)CAM-B3LYP/6-31G* using GAUSSIAN09 package [151]) for a zwitterionic (MPTTF$^{+\bullet}$-PTM^{-})$_2$ dimer in the crystallographic geometry (Fig.2.23, panel a), it was possible to give a reliable estimate to long-range

$V_{Dj,Dj+1}$	$V_{Dj,Rj+1}$	$V_{Rj,Dj+1}$	$V_{Rj,Rj+1}$	$V_{Dj,Rj}$	$V_{Dj+1,Rj+1}$
1.544	-1.256	-1.223	0.414	-0.782	-0.777

Table 2.2: Long-range electrostatic interaction energies between D and R units, as defined in Fig.2.23, panels b and c. Calculation done using ESP charges obtained at DFT level (functional (U)CAM-B3LYP, basis set 6-31G*) for the dimer crystallographic geometry. All the values are in eV.

electrostatic interactions acting along the stack. To this end, each dyad was divided into two parts, D and R, and the relevant electrostatic interactions between the resulting four pieces forming the aforementioned dimer were calculated. Results are reported in Table 2.2, while a sketch of D and R parts entering the calculation is shown in Fig.2.23, panels b and c. In order to get the oscillator strengths shown in Figure 2.23, panels d and e, each long-range electrostatic interaction in Table 2.2 was divided by the dielectric constant due to core electrons ($\sim$ 2 for CT crystals [111]). Results are superimposed onto the relevant experimental absorption spectra from Ref.[132]. We approximately match the experimental spectra, the peaks observed along the two polarizations being due to a complex interplay between both intra and intermolecular charge transfer degrees of freedom. However, additional experimental work is required in order to draw some definitive conclusion.

2.3 Conclusions

The interplay between intra and intermolecular charge transfer processes offers an unprecedented opportunity to further extend the already wide range of properties of functional molecular materials, thus paving the way for multifunctional systems whose structure can be carefully controlled through modern synthetic procedures.

The first part of the Chapter was fully dedicated to the theoretical modeling of a novel mixed stack CT crystal. Crucially, the system consists in the quasi monodimensional ...DADADA... mixed stack motif, each D site being decorated, through a conjugated π-bridge, with an organic radical, $R^\bullet$. Consequently, CT degrees of freedom create delocalized electrons along one dimension, thus recovering the usual mixed stack physics. In particular, N and I phases in Fig.2.6 are those typically observed within mixed stack CT crystals, the I phase being unstable towards dimerization (Fig.2.13, panel b) and leading to ferroelectric behavior (Fig.2.14, right panel).

Because of IET, a third new phase emerges (Z in Fig.2.6), presenting singly occupied D sites together with doubly occupied R sites, while leaving A sites empty. Combining IET and CT degrees of freedom, the ground state of the I phase is ferrimagnetic in nature. Using realistic parameters, the ferrimagnetic order is stable up to ambient temperature in a wide region of the I phase. Lattice dimerization weakens the magnetic order, without fully destroying it. As a result, ferrimagnetic and ferroelectric orders coexist in a finite region of the phase diagram (green area in Fig.2.13, panel c), thus making the decorated mixed stack studied in this work the first (potentially) multifferoic organic material.

The second part of the Chapter was fully devoted to the calculation of optical spectra within a decorated segregated stack CT crystal. In particular, stimulated by some recent experimental data on the MPTTF-PTM CT crystal, [132] a model to describe a stack of D-π-$R^\bullet$ molecules was presented and polarized optical spectra were calculated.

Quite surprisingly, weak intermolecular interactions (t is as small as 50 meV in MPTTF-PTM segregated CT crystal) are able to induce remarkable effects on the electronic spectra along both CT and IET directions. More precisely, for neutral stacks ($2z>0$) large effects are observed in the IET region (i.e., for energies $\sim 2z$) for both polarizations (Fig.2.21). The apparently complex physics is well understood in terms of $N+1$ essential states, with N being the number of D-π-$R^\bullet$ dyads forming the chain. On the other hand, considering ionic chains ($2z<0$), the IET band at $\sim |2z|$ comes with the signature of the Hubbard exciton at $\sim U_D$ (Fig.2.17). Here, IET and CT states are strongly intertwined with Hubbard excitonic states, thus making a description in terms of a few essential states difficult. Long-range electrostatic interactions were introduced in the model, their effect being investigated within neutral chains (Fig.2.22). In particular, using

ESP charges obtained at DFT level, calculated spectra reasonably matching MPTTF-PTM experimental ones were obtained (Fig.2.23).

Chapter 3

Ultrafast modulation of electronic spectra

The recent development of multiple ultrafast pulse techniques paved the way for the artificial modulation of material properties, thus leading to a direct control of spin, charge, orbital and lattice degrees of freedom.[50, 51] Exotic metastable phases were created upon ultrafast photoexcitation in both inorganic and organic strongly correlated systems and the resulting dynamics was followed in real time. Finely tuned pulses in the mid-infrared (mid-IR) and terahertz (THz) frequency regions [152, 153, 154, 155] were used to selectively excite molecular and lattice modes, affecting fundamental interactions as well as material macroscopic properties. Along these lines, using ultrafast strong THz pulses, a percolative metallicity was induced in VO_2 Mott insulator, [156, 157] whereas a rearrangement of the magnetic structure was observed in $TbMnO_3$ [158] and $TmFeO_3$ [159] perovskites. On the organic side, the dynamics of the photoinduced neutral-ionic transition (PINIT) in TTF-CA mixed stack CT crystal, as induced by an optical pump pulse with a photon energy equal to $\sim$0.6 eV, was detected with a time-resolution of $\sim$20 fs.[160] Moreover, ultrafast control of the electric polarization in TTF-CA ionic phase [161] as well as a paraelectric-to-ferroelectric transition [162] were achieved by THz modulation of the dimerization (Peierls) mode. In this context, both electron-vibration (e-mv) and electron-lattice (e-l) couplings play a prominent role in driving photoinduced phase transitions. Ultrafast spectroscopic techniques provide an unprecedented opportunity to test model Hamiltonians traditionally used to describe coupled electron-nuclear physics within strongly correlated electronic systems.

Recently, Kaiser and coworkers [56, 57] carried out ultrafast mid-infrared pump near-infrared probe experiments on the CT crystal ET-F$_2$TCNQ (bis (ethylenedithio) tetrathiafulvalene 2,5-difluorotetracyanoquinodimethane). Bis(ethylenedithio)tetrathiafulvalene (BEDT-TTF, shortly ET) is an organic electron donor, D, mainly known as the fundamental constituent of the so-called "quasi-two-dimensional (2-D) organic superconductors", a family of CT salts typically with composition ET$_2$X, where X is a monovalent electron acceptor (A) anion. In 1978, Mizuno and coworkers first prepared

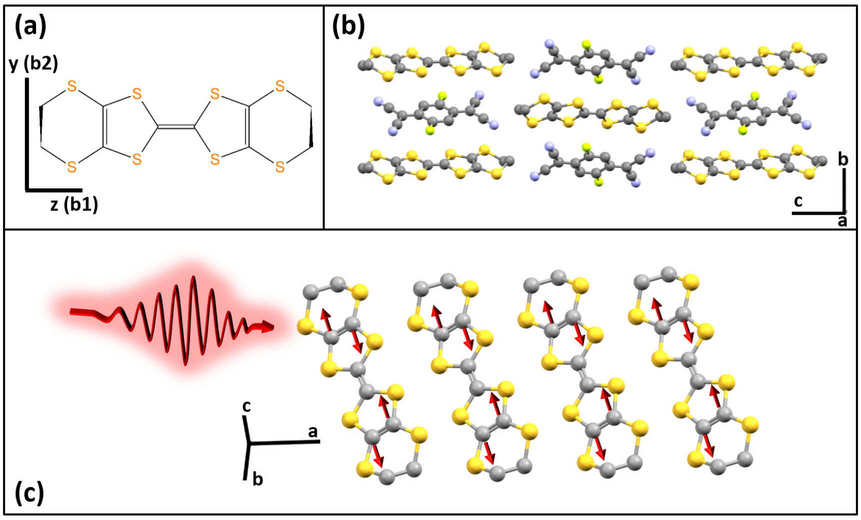

Figure 3.1: (a) Sketch of the molecular structure of ET molecule; labels along the axes refer to relevant irreducible representations in the D_2 point group.[163] (b) Crystallographic structure of ET-F$_2$TCNQ segregated stack CT crystal along a crystallographic axis (sulfur yellow, carbon grey, fluorine green, nitrogen blue). (c) Sketch of the ET$^{+\bullet}$ monodimensional stack interacting with the mid-IR pump pulse used in Refs.[56, 57]. Red arrows mark ET$^{+\bullet}$ ring deformation as induced by the pump pulse.

the ET-TCNQ salt, performing conductivity measurements on compressed pellets of the compound [164]. In 1986, Mori and Inokuchi found two polymorphs: a segregated-stack, highly conducting form [165] and a low conducting, mixed stack form [166]. In 1997, Hasegawa and coworkers reported the crystal structure of the segregated-stack ET-F_2TCNQ [167]. In this system ET is the electron donor, D (Fig.3.1, panel a), while F_2TCNQ is the electron acceptor, A, and the D-to-A CT is complete, thus leading to a segregated stack of fully charged $ET^{+\bullet}$ molecules (Fig.3.1, panel b). Even if F_2TCNQ favors monodimensional (1-D) stacking, Peierls and spin-Peierls instabilities are removed by ET tendency to form side-by-side interactions in a 2-D pattern. Indeed, this leads to the formation of a uniform 1-D Mott $ET^{+\bullet}$ chain surrounded by strongly localized unpaired spins on A units. An intrastack CT absorption band, related to intermolecular electron hopping is observed at ~5500 cm^{-1} for an electric vector parallel to *a* crystallographic stacking axis [167]. In Refs.[56, 57], an ultrashort mid-IR pump pulse (in the 900-

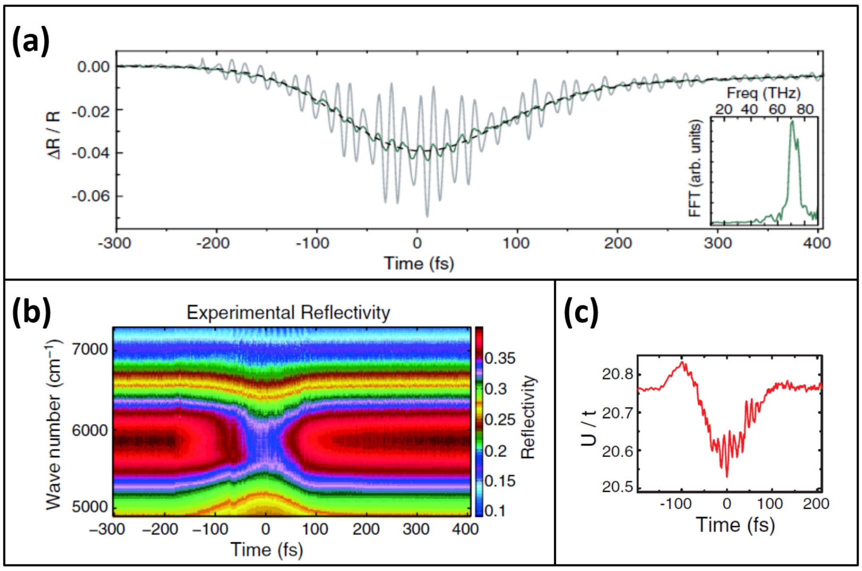

Figure 3.2: (a) Experimental time-evolution of the frequency integrated reflectivity signal for the ET-F_2TCNQ CT crystal at a pump fluence of 0.9 mJ/cm^2 at 298 K (continuous green curve). Double exponential fit is overlapped (dashed black curve). Probe pulse deconvolved signal is also shown (continuous grey curve). Relevant Fourier transform is reported in the inset, peaking at ~2390 cm^{-1}. (b) Two-dimensional map showing the experimental reflectivity signal as a function of both time and frequency. (c) Time-dependence of the Hubbard U/t term as obtained from fit. Data adapted from Ref.[57].

1100 cm^{-1} frequency range) polarized normally to the $\mathrm{ET}^{+\bullet}$ chains, is used to selectively drive a non-totally symmetric (non-ts) $\mathrm{ET}^{+\bullet}$ ring-deformation (Fig.3.1, panel c). While the molecules are still vibrating, a second weaker ultrafast pulse (probe pulse), polarized along the stack axis, interrogates the system in the near-IR (4000-7000 cm^{-1}) spectral region. As a result, a transient change of the intrastack CT band is observed, with ultrafast (coherent) oscillations at *twice* the frequency of the driven molecular mode (Fig.3.2, panels a and b).

In the first part of this Chapter, a theoretical description of the pump-probe experiment reported in Refs.[56, 57] is presented. Using quantum cell models parametrized against quantum chemical calculations, the coupled electron-nuclear dynamics of the system, as driven by the mid-IR pump pulse, is attacked by numerical integration of the time-dependent Schrödinger equation. The model Hamiltonian for ET-$\mathrm{F_2}$TCNQ CT crystal is described and validated against quantum chemical calculations in Sect.3.1. Considering the smallest possible system fragment, i.e. an $(\mathrm{ET}^{+\bullet})_2$ dimer, the problem is attacked in Sect.3.2 in a fully non-adiabatic way and adiabatically in Sect.3.3. The relevance of a dimer model in describing ET-$\mathrm{F_2}$TCNQ physics is discussed in Sect.3.4. Having validated the model, in the second part of the Chapter (Sect.3.5), we propose a novel two-phonon pump-probe experiment on TTF-CA CT crystal and preliminary results are presented.

3.1 The model

In ET-$\mathrm{F_2}$TCNQ crystal, the $\mathrm{ET}^{+\bullet}$ molecules form a 1-D strongly correlated electronic system, whose physics is described in terms of a 1-D Hubbard model extended to account for nearest-neighbor (n-n) electrostatic interactions:

$$\hat{H}_{el} = -t\sum_{i,\sigma}(\hat{c}^{\dagger}_{i,\sigma}\hat{c}_{i+1,\sigma} + H.c.) + U\sum_{i}\hat{n}_{i,\uparrow}\hat{n}_{i,\downarrow} + V\sum_{i}\hat{\rho}_i\hat{\rho}_{i+1}, \quad (3.1)$$

where $\hat{c}^{(\dagger)}_{i,\sigma}$ is the fermionic operator that annihilates (creates) an electron on the i-th ET molecular site with spin σ, while $\hat{n}_{i,\uparrow(\downarrow)}$ is the fermionic number operator counting the number of electrons with spin up (down) on the i-th chain site. Moreover, $\hat{\rho}_i = 2 - \hat{n}_i$ is the ET ionicity operator.

Looking at the right-hand side of Eq.3.1, the first term describes the electron delocalization along the stack, whereas the second term accounts for on-site electron-electron repulsion, U. Intermolecular electrostatic interactions are described by the third term, V. Focusing on the ET frontier orbital of a stack with N sites, the problem amounts to distributing N electrons on N sites, thus leading to a half filled Hubbard chain.

Estimates of model parameters entering Eq.3.1 were already reported in the literature.[56, 57, 168] The accepted estimate for the hopping integral, t=0.04 eV, agrees with what we obtain at the ZINDO level, using the "energy splitting in the dimer" model on the $(\mathrm{ET}^{+\bullet})_2$ dimer in the crystallographic geometry [169].

The Hubbard U can be estimated as the difference between the ionization potential and the electronic affinity of $\mathrm{ET}^{+\bullet}$ molecule, making use of the molecular total energies obtained from quantum chemistry methods. Indeed, Hubbard U is the energy relevant to the intrastack CT process, that is the Coulomb repulsive energy felt by two electrons both staying in the highest occupied molecular orbital (i.e., the HOMO) [170]:

$$U \quad = \quad \mathcal{E}(ET) - 2\mathcal{E}(ET^{+\bullet}) + \mathcal{E}(ET^{2+}), \tag{3.2}$$

where $\mathcal{E}$ is the ground state ET total energy in the different oxidation states. In particular, $\mathcal{E}(ET^{+\bullet})$=-97174.78329 eV was obtained after geometry optimization of $\mathrm{ET}^{+\bullet}$ in gas phase at DFT level ((U)B3LYP/6-31G*, using GAUSSIAN09 package [151]). Starting from this optimized geometry, $\mathcal{E}(ET)$=-97180.47697 eV and $\mathcal{E}(ET^{2+})$=-97165.02945 eV were obtained by adding and removing one electron, respectively, thus leading to U=4.06 eV, in good agreement with the literature [170, 171].

In Eq.3.1, all non-local electrostatic interactions are collapsed into the effective nearest-neighbor V interaction. Therefore, we cannot obtain a reliable estimate of V from quantum chemical calculations and fix V in order to best fit the experimental data. Since for the $(\mathrm{ET}^{+\bullet})_2$ dimer, discussed in the following, only $U - V$ enters the Hamiltonian, $U - V$=0.666 eV is used in order to correctly reproduce the experimentally observed frequency of the CT band, ~0.68 eV.

In the pump-probe experiment reported in Refs.[56, 57], the pump pulse, polarized normally to the a crystallographic axis, covers the 900-1100 cm^{-1}

mode (symmetry)	ω_v cm^{-1}	η^2 (D/Å)^{2}amu^{-1}	$\frac{\partial^2 U}{\partial Q^2}$ (meV)	$\frac{\partial^2 \Delta}{\partial Q^2}$ (meV)	$\frac{\partial^2 V}{\partial Q^2}$ (meV)	T$_b$	T$_c$
40 (b2)	902	0.2281	5.4	7.3	0.1	0.28	0.07
41 (b3)	918	0.1611	-0.5	1.7	0.0	0.72	0.01
42 (b2)	927	0.0173	1.0	2.6	0.0	0.28	0.07
43 (b1)	958	0.2974	-0.6	0.7	0.1	0.0	0.90
45 (b1)	1028	0.1634	0.2	-0.5	0.0	0.0	0.90
47 (b3)	1028	0.0017	-2.2	9.5	0.0	0.72	0.01
48 (b2)	1031	0.7663	-3.0	10.3	0.2	0.28	0.07
49 (b3)	1063	0.0060	4.1	6.3	0.0	0.72	0.01

Table 3.1: Selected results for ET$^{+\bullet}$ vibrational modes as obtained from DFT calculations ((U)B3LYP/6-31G*) in gas phase. Only IR-active modes in the 900-1100 cm^{-1} pump pulse spectral range are shown. For each normal mode (symmetry label in parenthesis), it is shown scaled vibrational frequency, ω_v, squared molecular dipole moment derivative with respect to the vibrational coordinate, η^2, and relevant electron-molecular vibration quadratic coupling constants. Moreover, squared director cosines relevant to b and c crystallographic axes are reported in the last two columns.

spectral range. The pump beam excites non-totally symmetric molecular vibrations (modes transforming as b_1, b_2 or b_3 irreducible representations in the D_2 molecular symmetry [163]) and specifically, it excites the in-phase motion of all molecules (zone-center vibrational modes). Accordingly, we will only consider quadratic modulations of the energies, since linear modulations are allowed only for symmetric modes.

Quantum chemistry methods (DFT) are used to estimate the relevant electron-molecular vibration coupling strengths. Starting from ET$^{+\bullet}$ gas phase optimized geometry ((U)B3LYP/6-31G*), a vibrational frequency calculation is performed to obtain molecular normal modes. A selected series of results is shown in Tab.3.1, whereas the complete set is shown in Appendix D. Vibrational frequencies, ω_v, are rescaled using scaling factors 0.9679 and 1.01 for frequencies above and below 1300 cm^{-1}, respectively [163]. As far as Hubbard U is concerned, the coupling constant reads:

$$\beta_\alpha = \left.\frac{\partial^2 U}{\partial Q_\alpha^2}\right|_0 = \frac{U(Q_\alpha) + U(-Q_\alpha) - 2U(0)}{Q_\alpha^2}, \tag{3.3}$$

where Q_α is the dimensionless normal coordinate associated with the α-th molecular mode, while $U(Q_\alpha)$ is obtained using Eq.3.2 for the deformed geometry. Results are reported in Tab.3.1.

Since all $\mathrm{ET}^{+\bullet}$ molecules vibrate in-phase, the modulation of the on-site energy is irrelevant (the total number of electrons being constant). However, for the sake of completeness, we have calculated the relevant coupling constants by calculating the modulation of the on-site energy, $\partial^2\Delta/\partial Q_\alpha^2$, where on-site energy is estimated from DFT calculations as:

$$\Delta \;=\; \mathcal{E}(ET^{+\bullet}) - \mathcal{E}(ET^{2+}). \tag{3.4}$$

Results are shown in Tab.3.1.

A rough estimate of the modulation of V can be obtained from the calculated IR intensities. Indeed, in the dipolar approximation the intermolecular interaction is proportional to the product of the molecular dipole moments, whose modulation with the vibrational modes is related to the IR intensity. We obtain:

$$\frac{\partial^2 V}{\partial Q_\alpha^2} \;=\; \frac{1}{4\pi\varepsilon_0 r^3}\frac{\hbar}{2\omega_\alpha}\eta_\alpha^2, \tag{3.5}$$

where r=3.59Å is the intrastack ET-ET distance [167], while η_α is ET ground state electric dipole moment derivative with respect to the α-th normal mode, its squared value being proportional to the IR intensity of the vibrational mode (third column in Tab.3.1). Results shown in Tab.3.1 correspond to small values, suggesting a negligible role of V modulation.

In the following, in agreement with Refs.[56, 57], we will only account for the quadratic U modulation and we will introduce a single coupled mode per molecule, so that the model Hamiltonian reads:

$$\hat{H} \;=\; \hat{H}_{el} + \frac{\hbar\omega_v}{4}\sum_i(\hat{P}_i^2 + \hat{Q}_i^2) + \beta\sum_i \hat{Q}_i^2\hat{n}_{i,\uparrow}\hat{n}_{i,\downarrow}, \tag{3.6}$$

where $\hat{Q}_i = (\hat{a}_i^\dagger + \hat{a}_i)$ and $\hat{P}_i = i(\hat{a}_i^\dagger - \hat{a}_i)$ are the dimensionless vibrational coordinate and conjugated momentum relevant to the i-th molecular site.

To calculate optical spectra, we need explicit expressions for the relevant components of the dipole operator. Intrastack CT excitation, polarized along the a stack axis, is described by the dipole operator:

$$\hat{\mu}_a = \sum_i i\hat{n}_i, \tag{3.7}$$

where both the electronic charge and the lattice constant are set to one. The pump beam, polarized perpendicular to the a axis, excites localized molecular vibrations, the relevant component of the dipole moment being:

$$\hat{\mu}_{IR} = \eta \sum_i \hat{Q}_i, \tag{3.8}$$

where squared η values are reported in Tab.3.1.

The director cosine matrix, $\mathbb{T}$, reads:

$$\mathbb{T} = \begin{pmatrix} a_x & a_y & a_z \\ b_x & b_y & b_z \\ c_x & c_y & c_z \end{pmatrix} = \begin{pmatrix} 0.528 & 0.81 & 0.21 \\ 0.846 & 0.532 & 0.0 \\ 0.1 & 0.256 & 0.95 \end{pmatrix}, \tag{3.9}$$

where molecular axes x, y, z and crystallographic directions a, b, c were defined in Fig.3.1, panels a and b, respectively. For the sake of clarity, c_z is the cosine of the angle between the c crystallographic axis and z ET direction. Squared c_z value gives the fraction of ET$^{+\bullet}$ molecules excited along z molecular direction, having pumped along c crystallographic axis. Looking at the relative IR intensities in Tab.3.1, third column, and at the squared director cosines shown in the seventh and eighth columns, the pump beam will mostly excite mode number 48. Consequently, in the following, we will use ω_v=1031 cm^{-1} and β=-3 meV, as relevant to mode 48.

3.2 Non-adiabatic results

The very large U/t ratio that characterizes ET$^{+\bullet}$ stacks in ET-F$_2$TCNQ crystals, suggests a strongly localized nature of the electronic structure. As it will be validated below, in this hypothesis a dimer (ET$^{+\bullet}$)$_2$ model is expected to reliably describe relevant excitations. With this choice, we are able to present fully non-adiabatic calculations of optical spectra.

Three singlet basis states are enough to describe optical spectra of a (ET$^{+\bullet}$)$_2$ dimer: $|\frown\rangle$, $|x0\rangle$, $|0x\rangle$, where x and 0 mark a doubly occupied ET site and an empty ET^{2+} site, respectively, whereas $|\frown\rangle = 2^{-1/2}(\hat{c}^{\dagger}_{1,\uparrow}\hat{c}^{\dagger}_{2,\downarrow} - \hat{c}^{\dagger}_{1,\downarrow}\hat{c}^{\dagger}_{2,\uparrow})|00\rangle$ is the singlet valence bond (VB) state. Introducing in-phase and out-of-phase vibrational coordinates, $\hat{Q}_{\pm} = 2^{-1/2}(\hat{Q}_1 \pm \hat{Q}_2)$, and their conjugated momenta, $\hat{P}_{\pm}$, Eq.3.6 can be rewritten for the (ET$^{+\bullet}$)$_2$ dimer as:

$$\begin{aligned} \hat{H}_{dim} &= -t\sum_{\sigma}(\hat{c}^{\dagger}_{1,\sigma}\hat{c}_{2,\sigma} + H.c.) + U_{eff}(\hat{n}_{1,\uparrow}\hat{n}_{1,\downarrow} + \hat{n}_{2,\uparrow}\hat{n}_{2,\downarrow}) \\ &\quad + \frac{\hbar\omega_v}{4}(\hat{P}_+^2 + \hat{P}_-^2 + \hat{Q}_+^2 + \hat{Q}_-^2) \\ &\quad + \beta\frac{\hat{Q}_+^2 + \hat{Q}_-^2}{2}(\hat{n}_{1,\uparrow}\hat{n}_{1,\downarrow} + \hat{n}_{2,\uparrow}\hat{n}_{2,\downarrow}) \\ &\quad + \beta\hat{Q}_+\hat{Q}_-(\hat{n}_{1,\uparrow}\hat{n}_{1,\downarrow} - \hat{n}_{2,\uparrow}\hat{n}_{2,\downarrow}), \end{aligned} \tag{3.10}$$

where $U_{eff} = U - V$ and σ runs over spin polarizations. Actually, only the in-phase motion, $\hat{Q}_+$, is driven by the pump beam, whereas the out-of-phase combination, $\hat{Q}_-$, starts moving because of the coupling to $\hat{Q}_+$ through the electronic system, as described by the last term in Eq.3.10.

Following Chapter 1, in order to treat on an equal footing both electrons and nuclei, a fully non-adiabatic approach to the (ET$^{+\bullet}$)$_2$ dimer Hamiltonian in Eq.3.10 is adopted. More precisely, the non-adiabatic approach writes the system Hamiltonian on the vector space spanned by the direct product of the three electronic states times the eigenstates of $\hat{Q}_+$ and $\hat{Q}_-$ harmonic oscillators. The harmonic oscillators basis, being infinite, are truncated to m states, with m large enough in order to reach convergence on quantities of interest (typically, m=10 is set for both $\hat{Q}_+$ and $\hat{Q}_-$, thus reaching a total dimension of 300). The exact diagonalization of the Hamiltonian gives the numerically exact non-adiabatic (i.e. vibronic) eigenstates describing the coupled electron-nuclear motion.

3.2.1 Static and dynamic properties

We start the discussion with a preliminary analysis of the effect of the mid-IR pump beam on the absorption spectrum. The pump pulse is expected to populate the first few vibrational eigenstates of $\hat{Q}_+$. In order to identify the first vibrational eigenstate, $|v_1\rangle$, among the vibronic eigenstates obtained from the diagonalization of the non-adiabatic Hamiltonian, we search for the excited state, $|E\rangle$, with the largest transition dipole moment from the ground state, $|\langle G|\hat{\mu}_{IR}|E\rangle|^2$. The second vibrational eigenstate, $|v_2\rangle$, is found looking for the state $|E'\rangle$ with the largest $|\langle v_1|\hat{\mu}_{IR}|E'\rangle|^2$ and so on.

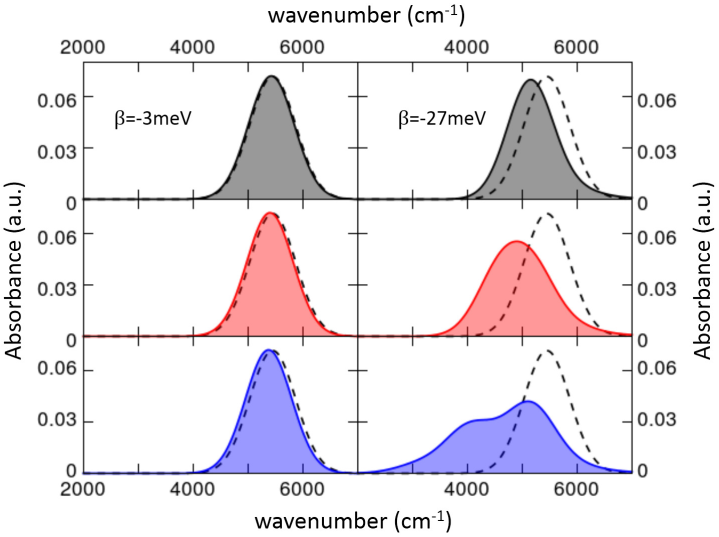

Figure 3.3: Optical CT spectra calculated for a $(ET^{+\bullet})_2$ dimer with ω_v=1031 cm^{-1} and β=-3 meV (left panels) and -27 meV (right panels). Spectra calculated from the ground state, $|G\rangle$, and from $|v_1\rangle$ and $|v_2\rangle$ are shown in upper, middle and bottom panels, respectively. The dashed lines show the same spectra calculated for β=0 (i.e., for no electron-vibration coupling).

In Fig.3.3, we show the absoprtion spectra calculated for the $(ET^{+\bullet})_2$ dimer starting from the ground state ($|G\rangle$), from the first and second vibrationally excited states ($|v_1\rangle$ and $|v_2\rangle$, respectively). Results obtained in the absence of e-mv coupling (β=0) are compared with those obtained for a realistic value of the coupling (β=-3 meV) and for an unphysically large coupling (β=-27 meV).

In the hypothesis that the mid-IR pulse populates $|v_1\rangle$ and $|v_2\rangle$, it is clear that (as expected) the pump-pulse will not affect CT spectra of the system with no e-mv coupling. On the other hand, a progressive red-shift of the band is observed upon populating $|v_1\rangle$ and $|v_2\rangle$, the effect increasing with the strength of the coupling. For positive β values a blue-shift of the band is observed (results not shown). The experimentally observed transient $\sim$70 cm^{-1} red-shift of the absorption band [57] is reproduced in Fig.3.3, left panels, where parameters relevant to ET normal mode number 48 were used, accounting for realistic excitations up to $|v_2\rangle$. We observe that the satellite peaks reported in Ref.[56] in the 3000-4000 cm^{-1} spectral range are not reproduced by our calculations unless unrealistically large $|\beta|$ values are adopted, at least one order of magnitude larger than those estimated through DFT calculations (Fig.3.3, right panels).

Having discussed the effect of the population of vibrational states on optical spectra, we now turn attention to the simulation of the pump-probe experiment. To this aim, the time-dependent pump pulse electric field is explicitly introduced into Eq.3.10:

$$\hat{H}(t) \quad = \quad \hat{H}_{dim} - \hat{\mu}_{IR}F(t), \tag{3.11}$$

where $F(t)$ is the time-dependent electric field associated with the pump pulse. In particular, in order to reproduce the experimental pump beam, $F(t)$ is defined by a cosine with frequency ω_{IR}=1010 cm^{-1} convolved with a Gaussian profile having zero mean and standard deviation σ=100 fs (Fig.3.4, panels a and b). Consequently, Eq.3.11 can be rewritten as:

$$\hat{H}(t) \quad = \quad \hat{H}_{dim} - \sqrt{2}\eta F_0 cos(\omega_{IR}t)e^{-\frac{t^2}{\sigma^2}}\hat{Q}_+, \tag{3.12}$$

where F_0 is the amplitude of the pump pulse electric field.

The time-dependent Schrödinger equation for the electron-nuclear coupled problem is numerically integrated through a fourth-order Runge-Kutta algorithm, with time step equal to 0.1 fs.[102] The calculated expectation value of $\hat{Q}_+^2$ in time is reported in Fig.3.4. It shows oscillations at twice the pump frequency, as shown by the relevant Fourier transform in panel d (blue filled area). The out-of-phase vibrational motion, $\hat{Q}_-$, being coupled to the pump field only through $\hat{Q}_+$, oscillates at the same frequency, but with an amplitude four orders of magnitude smaller than that observed for $\hat{Q}_+^2$ (Fig.3.4, insets in panels c and d), confirming that only zone-center modes are spectroscopically relevant.

Damped oscillations in the experimental spectra (Fig.3.2, panels a and b) can be reproduced accounting for some source of energy dissipation. To this end, following the quantum-classical hybrid approach discussed in Subsect.1.3.1, a bath of 20 classical particles connected through anharmonic springs is coupled to the $(\mathrm{ET}^{+\bullet})_2$ dimer. The reservoir potential function

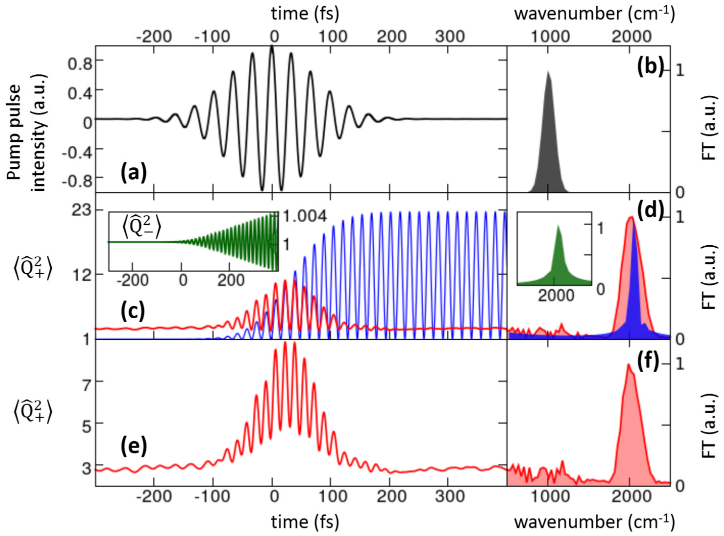

Figure 3.4: Mid-IR pump pulse driven quantum dynamics of the coupled electron-vibrational $(\mathrm{ET}^{+\bullet})_2$ system. (a-b) Temporal evolution of the pump beam electric field and its Fourier transform, respectively. (c-d) Temporal evolution of $\langle \hat{Q}_+^2 \rangle$ calculated for a non-dissipative (blue line) and a dissipative (red line) driven system, and their Fourier transforms, respectively. Green curves in the insets in panels c and d show the relevant results for the out-of-phase mode, $\langle \hat{Q}_-^2 \rangle$, with no friction. (e-f) Time-dependence of $\langle \hat{Q}_+^2 \rangle$ calculated for a driven dissipative system, accounting for the finite temporal resolution of the probe pulse (FWHM=10 fs) and its Fourier transform, respectively. Same model parameters as used in Fig.3.3, left panels.

reads:[53]

$$V_{\mathcal{B}} = \frac{\hbar\omega_b}{4} \sum_{i=1}^{20} \Big(q_i(t) - q_{i+1}(t)\Big)^2 + V_0\chi^4 \sum_{i=1}^{20} \Big(q_i(t) - q_{i+1}(t)\Big)^4, \tag{3.13}$$

where q_i is the dimensionless coordinate relevant to the i-th classical oscillator, its reference vibrational frequency, ω_b, set to 60 cm^{-1}. We set $q_i(t=0)$=0, $\forall i$=1,..., 20. Moreover, χ=4.4 is the anharmonicity constant, whereas V_0 is set to 1 eV. Fixed boundary conditions are adopted by introducing a fixed extra coordinate, $q_{21}(t)$=0.

The first classical oscillator of the chain is directly connected to the $(\mathrm{ET}^{+\bullet})_2$ dimer with a coupling strength α=0.16 eV. In particular, the $\mathcal{SB}$

interaction term reads:

$$\hat{H}_I \;=\; -\alpha \hat{Q}_+ q_1(t), \tag{3.14}$$

where $q_1(t)$ is the coordinate of the first classical oscillator. On the other hand, the five classical oscillators most distant from the quantum system (i.e., i=16-20) are linked to five different uncorrelated thermostats, their temperatures being all set equal to 298 K.

Following Eq.1.24, the equation of motion for the i-th classical particle reads:

$$\begin{aligned} \frac{\hbar}{2\omega_b}\frac{d^2 q_i}{dt^2} &= -\frac{\partial V_{\mathcal{B}}}{\partial q_i} + \alpha\langle \hat{Q}_+\rangle \delta_{i,1} \\ &+\frac{\hbar}{2\omega_b}\left(-\gamma\frac{dq_i}{dt} + 2\zeta\sqrt{\frac{\gamma k_b T \omega_b}{\hbar \Delta t}}\right)\delta_{i,j}, \end{aligned} \tag{3.15}$$

where the Kronecker delta $\delta_{i,1}$ ensures that only the first oscillator of the chain is directly connected to the $(\mathrm{ET}^{+\bullet})_2$ dimer, thus feeling the average quantum back reaction. Terms entering the second line of the equation account for dissipation and Langevin-type thermal fluctuations for oscillators number j=16-20. In particular, the static friction coefficient, γ, is set equal to 10^{15} s^{-1}, while ζ is a Gaussian random variable with unit standard deviation and zero mean.

As already discussed in Subsect.1.3.1, at each temporal step, Eq.3.15 is numerically solved for each classical coordinate, q_i, using Verlet algorithm.[100, 101] The newly calculated $q_1(t+\Delta t)$ is plugged into Eq.3.14 and fourth-order Runge-Kutta algorithm is used to propagate in time the $(\mathrm{ET}^{+\bullet})_2$ dimer wave function.[102] Moreover, the same time step is used for both quantum and classical dynamics, Δt=0.1 fs. Relevant results are obtained averaging several Langevin trajectories, 741 being the typical number.

The parameters entering the dissipation model were selected to reproduce the experimentally observed fast decay of the ultrafast reflectivity oscillations (Fig.3.2, panels a and b). Indeed, a careful balance has to be found between the classical chain anharmonicity, χ, and the system-bath coupling strength, α, in order to guarantee a fast flow of the pumped energy away from the quantum system. Moreover, a proper γ value must be chosen in order to reach the correct canonical equilibrium state.[53]

The red curve in Fig.3.4, panel c, well reproduces the experimentally observed coherent reflectivity oscillations in Fig.3.2, panel a. A closer agreement with the experiment is obtained by convolving the red curve with a Gaussian signal having FWHM=10 fs, thus accounting for the experimental probe pulse finite temporal resolution.

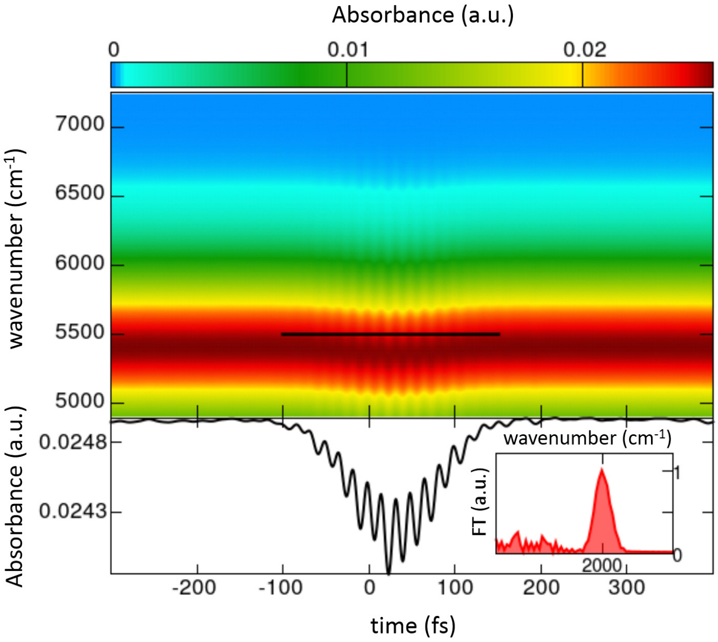

Figure 3.5: Time evolution of the optical CT spectrum obtained for a dissipative dimer with ω_v=1031 cm^{-1} and β=-3 meV, using a probe pulse with FWHM=10 fs. Bottom panel: section at 5500 cm^{-1} (the black line superimposed on the color map marks this value) together with its Fourier transform (shown in the inset). Results obtained averaging 741 Langevin trajectories for the same model parameters used in Fig.3.3, left panels.

Time-dependence of optical CT spectrum is reported as a color map in Fig.3.5. In particular, the 3-fold electronic dimer Hamiltonian is diagonalized for each $\langle \hat{Q}_+(t) \rangle$ value and the absorption spectrum is calculated adopting a Gaussian band shape with HWHM=0.09 eV. Ultrafast oscillations of the CT band are clearly visible both in the color map and in the section at 5500 cm^{-1} (bottom panel) at twice the pump frequency (Fourier transform of the time-section is shown in the inset). These results nicely

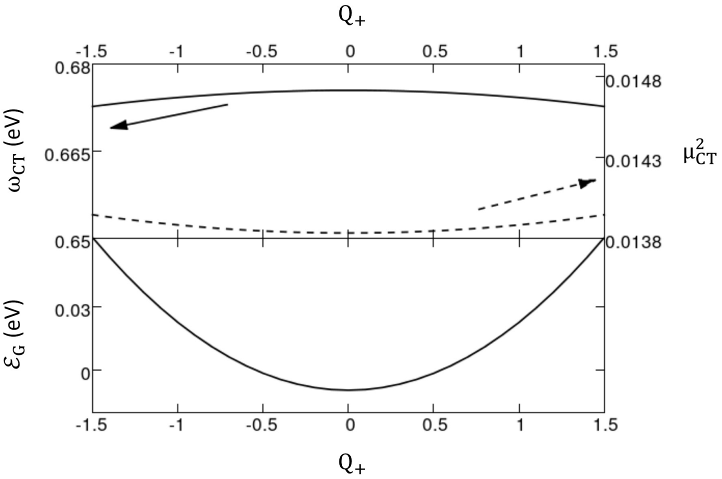

Figure 3.6: The adiabatic $(\mathrm{ET}^{+\bullet})_2$ dimer. CT transition frequency, squared transition dipole moment (top panel) and ground state energy (bottom panel) vs Q_+.

match the experimental data in Fig.3.2, panels a and b, without imposing any ad-hoc Hubbard U time-dependence as it was done in Ref.[57] (see Fig.3.2, panel c).

3.3 Adiabatic results

The fully non-adiabatic approach discussed in the previous Section is computationally intensive and makes the adiabatic ansatz quite appealing. The dimer Hamiltonian in the adiabatic approximation reads:

$$\hat{H}_{dim}(Q_+) = \hat{H}_{el} + \frac{\hbar\omega_v}{4}Q_+^2 + \beta\frac{Q_+^2}{2}(\hat{n}_{1,\uparrow}\hat{n}_{1,\downarrow} + \hat{n}_{2,\uparrow}\hat{n}_{2,\downarrow}), \quad (3.16)$$

where the effect of the out-of-phase nuclear motion, Q_-, on the electronic degrees of freedom was safely neglected and the nuclear kinetic energy was disregarded in line with the adiabatic approximation. Written on the 3-fold Hilbert space, $\mathcal{H}_{dim} = span\{|\frown\rangle, |x0\rangle, |0x\rangle\}$, Eq.3.16 reads:

$$\hat{H}_{dim}(Q_+) = \begin{pmatrix} 0 & -\sqrt{2}t & -\sqrt{2}t \\ -\sqrt{2}t & U_{eff}(Q_+) & 0 \\ -\sqrt{2}t & 0 & U_{eff}(Q_+) \end{pmatrix} + \frac{\hbar\omega_v}{4}Q_+^2, \quad (3.17)$$

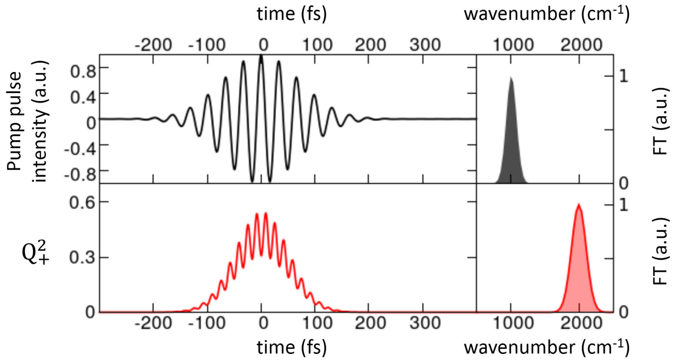

Figure 3.7: Classical Q_+ dynamics as induced by the mid-IR pump pulse (upper left panel) on the ground state potential energy curve, $\mathcal{E}_G$, of the $(\mathrm{ET}^{+\bullet})_2$ dimer. $Q_+^2(t)$, convolved with the probe pulse profile (FWHM=10 fs), is shown in the bottom left panel. Corresponding Fourier transforms are shown in the right panels.

where $U_{eff}(Q_+) = U - V + \beta Q_+^2/2$. Introducing the two symmetrized CT states, $|\pm\rangle = 2^{-1/2}(|x0\rangle \pm |0x\rangle)$, Eq.3.17 becomes:

$$\hat{H}'_{dim}(Q_+) = \left(\begin{array}{cc|c} 0 & -2t & 0 \\ -2t & U_{eff}(Q_+) & 0 \\ \hline 0 & 0 & U_{eff}(Q_+) \end{array}\right) + \frac{\hbar\omega_v}{4} Q_+^2. \quad (3.18)$$

Diagonalizing the highlighted block, one gets the adiabatic ground state energy:

$$\mathcal{E}_G(Q_+) = \frac{1}{2}\left(U_{eff}(Q_+) - \sqrt{U_{eff}^2(Q_+) + 16t^2}\right) + \frac{\hbar\omega_v}{4} Q_+^2. \quad (3.19)$$

The analytical expressions for the excitation energy, ω_{CT}, and for the squared transition dipole moment, μ_{CT}^2, read:

$$\omega_{CT}(Q_+) = \frac{1}{2}\left(U_{eff}(Q_+) + \sqrt{U_{eff}^2(Q_+) + 16t^2}\right), \quad (3.20)$$

$$\mu_{CT}^2(Q_+) = \frac{1}{2}\left(1 - \frac{U_{eff}(Q_+)}{\sqrt{U_{eff}^2(Q_+) + 16t^2}}\right), \quad (3.21)$$

where the dimensionless transition dipole moment is expressed in $e \cdot a$=1 units. The three quantities are shown in Fig.3.6 as a function of Q_+.

The Q_+-dependent ground state energy in Fig.3.6, bottom panel, represents the potential energy for Q_+ motion. Accordingly, the classical Q_+ dynamics is calculated through numerical integration (Verlet algorithm [100, 101]) of the differential equation:

$$\frac{d^2Q_+}{dt^2} = \frac{\omega_v}{\hbar}\left(-\frac{\partial\mathcal{E}_G}{\partial Q_+} + F(t)\right) - \gamma\frac{dQ_+}{dt}, \tag{3.22}$$

where $Q_+(t=0) = 0$ and the static friction coefficient γ=10^{15} s^{-1} accounts for the finite lifetime of the vibrational excitation.

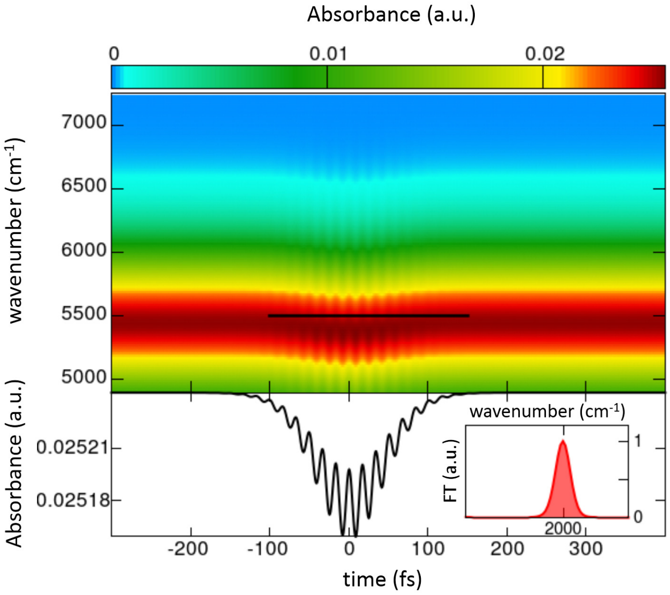

Figure 3.8: Time evolution of the optical CT spectrum at 0K, calculated in the adiabatic limit for the same model parameters as in Fig.3.3, left panels, and γ=10^{15} s^{-1}. A section of the map at ω=5500 cm^{-1} (the black line superimposed on the color map marks this value) is reported in the bottom panel, with the relevant Fourier transform shown in the inset. A Gaussian band shape with HWHM=0.09 eV is assigned to CT transition.

Results from classical dynamics are reported in Fig.3.7 and compare well with the non-adiabatic ones in Fig.3.4, thus confirming the validity of the adiabatic approximation. Same conclusions can be drawn while looking at the time-evolution of the optical CT spectrum in Fig.3.8, being very similar to the non-adiabatic result (Fig.3.5).

3.4 Larger ET$^{+\bullet}$ clusters: the wave function localization

Having proved the reliability of the adiabatic approximation, we could treat larger systems, up to 14 ET$^{+\bullet}$ sites. However, the dimer model is sufficient to describe the pump-probe experiment reported in Refs.[56, 57] because of the extremely localized nature of the ET-F$_2$TCNQ system, having $U_{eff} > 16t$. In order to prove this view, the Hamiltonian in Eq.3.1 is written, for U=0.666 eV and V=0, on the real-space basis, distributing N electrons on N site orbitals. Since each ET site can be empty, singly or doubly occupied, the basis dimension moves from more than 63000 electronic states for S_z=0 and N=10, to more than 850000 for S_z=0 and N=12.

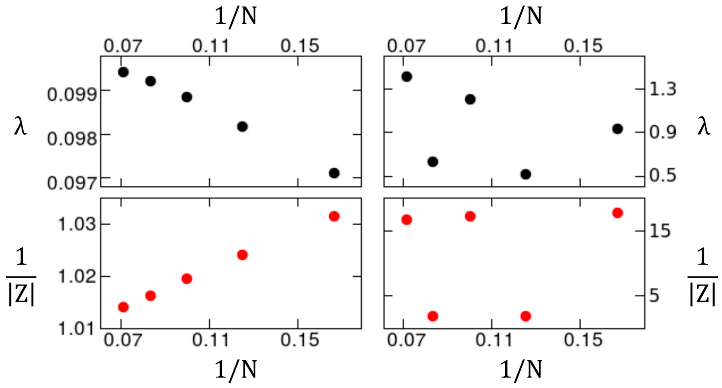

Figure 3.9: Ground state wave function delocalization for the model in Eq.3.1, with U=0.666 eV and V=0. Top panels: wave function delocalization length, λ. Bottom panels: inverse modulus of the complex quantity Z, as defined in Eq.2.20. All quantities are reported against the inverse number of chain sites. Left panels show results for t=0.04 eV, as relevant to ET-F$_2$TCNQ crystal. Right panels show results for a system with a much larger t=1.1 eV. In the right panels, large finite size effects are seen in terms of a large difference between $N = 4n$ and $N = 4n + 2$ systems.

Due to its extremely sparse nature, the Hamiltonian matrix is stored in machine memory using the CSR format in the 3-array variation [139] (see Subsect.2.1.2.3) and diagonalization routines from the ARPACK library [140] are used to get the fully correlated electronic ground state. Periodic boundary conditions are adopted in order to reduce finite size effects. Both spin and translational (i.e., rotational) symmetries are exploited by working in the S_z=0 and $|\vec{k}|$=0 sectors.

To study the system wave function delocalization, the complex quantity, Z, defined in Eq.2.20 can be used.[144, 145] In particular, for localized systems, $1/|Z| \rightarrow 1$ for $N \rightarrow \infty$. This is clearly shown in Fig.3.9, lower left panel, for t=0.04 eV as relevant to ET-F$_2$TCNQ crystal. On the other hand, results obtained for t=1.1 eV (lower right panel) are not converged, finite size effects being too large. Along the same lines, the dimensionless delocalization length defined as $\lambda = \sqrt{-N \log |Z|^2/(2\pi n_0)}$, with n_0 being the electron average site density, [144, 145] corresponds to a small fraction of the crystal unit cell, further validating an analysis based on a dimer model.

3.5 2-phonon excitation in TTF-CA

Recently, ultrashort (few picoseconds) THz light pulses were used to drive out-of-equilibrium a lattice mode in the CT mixed-stack crystal TTF-CA (Fig.3.10, panel a) [161, 162], observing an ultrafast (coherent) modulation of the reflectivity signal at twice the pump pulse frequency. In this Section, we do not discuss these results, rather we design a new experiment.

The physics of TTF-CA crystal is well captured by the modified Hubbard model in Eq.2.1 extended in order to account for long-range electrostatic interactions and adiabatically coupled to lattice dimerization (Peierls) mode, δ, and molecular mode, q.[30, 49, 47] The high correlation limit is typically adopted, thus sending to infinity both Hubbard U and site energy, Δ, while keeping finite the difference $2\Gamma = 2\Delta$-U.[134, 108, 30, 47]

Treating Coulomb long-range interactions at the mean-field level, the Hamiltonian for a N-sites TTF-CA stack reads:[30]

$$\begin{aligned}\hat{H}_{MF} \;\; = \;\; & \left(\Gamma - \frac{V}{2} + q - \varepsilon_c \rho\right) \sum_i (-1)^i \hat{n}_i \\ & - \sum_i [1 + (-1)^i \delta](\hat{c}^\dagger_{i,\sigma} \hat{c}_{i+1,\sigma} + H.c.) \\ & + \frac{N}{2} \varepsilon_c \rho^2 - N \varepsilon_c \rho + N \frac{q^2}{2\varepsilon_v} + N \frac{\delta^2}{2\varepsilon_d},\end{aligned} \tag{3.23}$$

where the first line describes site energy modulation as induced by the

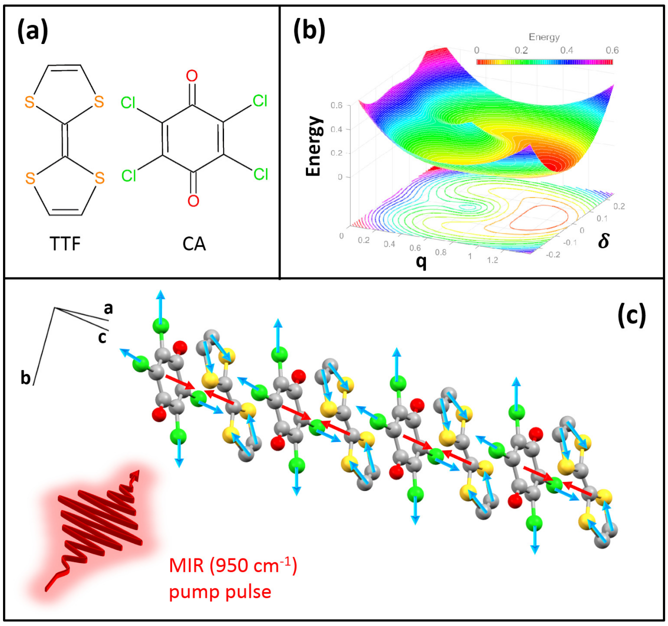

Figure 3.10: Two-phonon excitation in TTF-CA. (a) Molecular structures of TTF and CA. (b) Ground state potential energy, $\mathcal{E}_{GS}$, as a function of q and δ, for a neutral (V=2.26) TTF-CA ring with N=8 (contour lines at the bottom of the plot clearly show the PES having a single minimum, as relevant to the neutral regular stack). Other model parameters: α=1.4, ε_v=1.8, ε_d=0.28, where t hopping integral is taken as the energy unit. (c) Sketch of the novel pump-probe experiment discussed in this Section. Pumped lattice dimerization mode (red arrows) puts molecular totally symmetric modes in motion (light blue arrows).

totally-symmetric molecular coordinate, q, and the electrostatic interactions. Indeed, V is the intrachain nearest-neighbor Coulomb interaction and $\varepsilon_c\rho = V(\alpha - 1)\rho$, α being the crystal Madelung constant and ρ the average on-site ionicity. The second line of the Hamiltonian describes the electron delocalization along the stack, being modulated by the lattice distortion coordinate, δ. Nuclear as well as electrostatic potential energies enter the third line of the equation, with ε_v and ε_d being the molecular and the lattice relaxation energies, respectively. The nuclear kinetic energy is neglected in line with the adiabatic approximation. Model in Eq.3.23

proved successful in describing ground state as well as excited state TTF-CA properties.[172, 30, 48, 31, 142, 47]

In this Section, we design the modulation of the CT spectral band in neutral TTF-CA crystal via ultrafast pumping of the combination bands observed in the infrared (IR) spectra of TTF-CA.[109] More precisely, an ultrashort pump beam tuned in the mid-IR frequency region and polarized along the TTF-CA stack axis is used to drive the lattice dimerization mode, δ (Fig.3.10, panel c). Indeed, the frequency of the lattice mode falls in the far-IR spectral region ($\sim$20-50 cm^{-1} [109, 111]) and it is not in resonance with the mid-IR pump pulse. Consequently, as soon as the pump pulse is switched off, the lattice mode equilibrates (off-resonance driven motion). However, while pumping, because of the strong anharmonicity inherent in the system, energy starts flowing from δ to the totally symmetric q molecular coordinate that, being resonant with the pump pulse, is actually put in motion. Accordingly, a site energy modulation is triggered, leading to a coherent modulation of the CT band at the frequency of the combination band. In the following, some preliminary results seem to confirm this idea.

The Hamiltonian in Eq.3.23 is written on the real-space basis for finite size rings (typically, N=8). In order to reduce the problem size, calculations are carried out within the S_z=0 spin space, further limiting to the center of the Brillouin zone. Using the Lanczos algorithm, the Hamiltonian matrix is diagonalized (typically, asking for the first 20 eigenvalues and eigenvectors) for different (Γ_{eff}, δ) points, where $\Gamma_{eff} = \Gamma - \frac{V}{2} + q - \varepsilon_c \rho$. The expectation value of the ionicity, ρ, is then used to self-consistently get the relevant potential energy surfaces (PES). The PES in Fig.3.10, panel b, is the ground state for a neutral (V=2.26) TTF-CA stack, having set α=1.4, ε_v=1.8, ε_d=0.28, with t hopping integral taken as the energy unit [30, 47] (however, when energy absolute values are nedeed, t is set equal to 0.21 eV, as relevant to TTF-CA crystal [141, 142]).

Now, let's focus on the effect of an externally applied electric field. In Sects.3.2 and 3.3, the driving pump-pulse was polarized normally to the ET ring plane. Here, on the contrary, we want to apply an electric field polarized along the TTF-CA ring in order to drive out-of-equilibrium the dimerization lattice mode, δ. The definition of an electric field parallel to the stack axis and of the relevant dipole moment operator is a tricky affair for systems

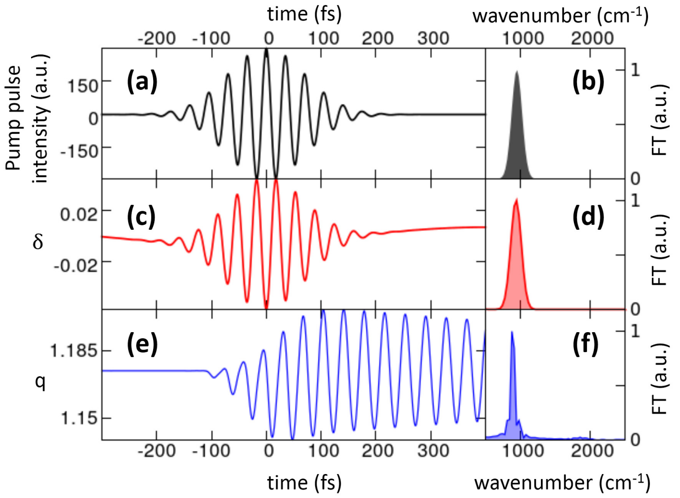

Figure 3.11: TTF-CA classical nuclear dynamics as induced by a mid-IR pump pulse polarized along the stack. (a) Time-dependency of the pump pulse used in the calculations. (c-e) Lattice, δ, and molecular, q, driven motions, respectively. (b-d-f) Relevant Fourier transforms. Results shown for a neutral (V=2.26) TTF-CA ring with N=8 at 298 K. Other model parameters: α=1.4, ε_v=1.8, ε_d=0.28, where t hopping integral is taken as the energy unit.

with periodic boundary conditions [148, 141, 149]. However here, much as done in Sect.3.3, we just introduce the electric field to drive the lattice mode. Accordingly, the equations of motion for the classical dynamics of δ and q coordinates on the ground state PES, $\mathcal{E}_{GS}(\delta, q)$, read:

$$\frac{d^2\delta}{dt^2} = \frac{\varepsilon_d}{N}\omega_d^2\left(- \frac{\partial \mathcal{E}_{GS}}{\partial \delta} + F(t)\right) - \frac{1}{\tau_d}\frac{d\delta}{dt}, \tag{3.24}$$

$$\frac{d^2 q}{dt^2} = -\frac{\varepsilon_v}{N}\omega_v^2 \frac{\partial \mathcal{E}_{GS}}{\partial q} - \frac{1}{\tau_v}\frac{dq}{dt}, \tag{3.25}$$

where the oscillator frequencies are set to ω_v=1200 cm^{-1} and ω_d=66 cm^{-1}. We set relevant decay times based on the experimental data reported in Ref.[160] as τ_v=650 fs and τ_d=5.25 ps. The pump pulse profile used in the simulations, $F(t)$, is shown in Fig.3.11, panel a, together with its Fourier transform peaking at 950 cm^{-1} in panel b. In order to calculate partial derivatives $\partial\mathcal{E}_{GS}/\partial\delta$ and $\partial\mathcal{E}_{GS}/\partial q$, the ground-state PES is first interpolated (bilinear interpolation algorithm) and five-point stencil method is used. Eqs.3.24 and 3.25 are solved using Verlet algorithm, with time-step Δt=0.1 fs.

We start from a neutral regular stack, i.e. $\delta(t=0)=0 \wedge \dot{\delta}(t=0)=0$. Moreover, since the PES minimum (Fig.3.10) is rather flat along q axis, a thermal (Boltzmann) distribution of $q(t=0)$ values is considered. As a consequence, several trajectories (typically, 70) starting from slightly different q values are considered, while we always set $\dot{q}(t=0)=0$. Time-dependent properties are obtained averaging over the 70 Boltzmann-weighted different trajectories.

Because of its symmetry, the pulsed electric field, $F(t)$, is coupled to the dimerization (Peierls) lattice mode, δ, and not to the totally symmetric molecular vibration, q. Looking at Fig.3.11, panels a and c, we see that switching on the pump pulse immediately starts δ oscillations at the pump frequency (the relevant Fourier transforms being shown in panels b and d). The δ oscillations stop as soon as $F(t)$ is switched off and well before its relevant decay time, τ_d. Indeed, because of the non-resonance condition (pump pulse frequency much larger than ω_d) there is no energy transfer from the electric field to the dimerization mode and the switching off of the δ oscillations has nothing to do with the relaxation time τ_d. However, because of the anharmonicity inherent in TTF-CA ground-state PES, when the Peierls phonon is driven, we also perturb the totally symmetric molecular vibration, q (panel e), that after some time ($\sim$100 fs according to the simulation) starts oscillating at the pump frequency (panel f) in a truly δ-mediated process. Unlike δ, the molecular mode resonates with the electric pulse, a true energy absorption takes place and q oscillations dampen on a longer time as determined by the decay time, τ_v. Indeed, this is the real-time picture of the combination bands that are observed in the infrared spectra of TTF-CA [109], with energy being absorbed at $\omega_v \pm \omega_d$.

Resorting to the velocity dipole formalism (see Eq.2.30), it is possible to calculate optical spectra for an electric field polarized along the ring.[148, 141, 149] Accounting for the stack dimerization, the velocity dipole operator

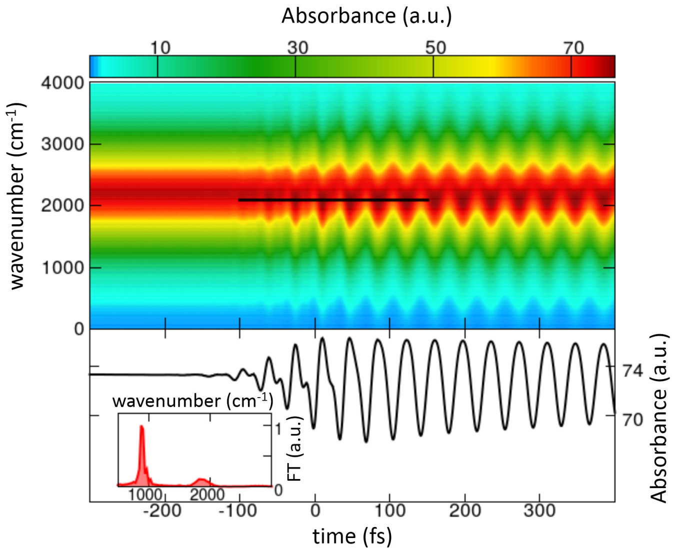

Figure 3.12: Time evolution of neutral TTF-CA optical CT spectrum obtained for TTF-CA ring with N=8 as driven by the mid-IR pump pulse in Fig.3.11, panel a. Bottom panel: time-section at ω=2101 cm^{-1} (the black line superimposed on the color map marks this value). The relevant Fourier transform is reported in the inset. Same model parameters used in Fig.3.11.

reads:

$$\begin{aligned}\hat{v} &= \frac{i}{\hbar}[\hat{H}_{MF}, \hat{\mu}_a] \\ &= -i\frac{eta}{\hbar}\sum_{j,\sigma}[1+(-1)^j\delta](\hat{c}^\dagger_{j,\sigma}\hat{c}_{j+1,\sigma} - H.c.),\end{aligned} \tag{3.26}$$

where $\hat{\mu}_a = \sum_j [j+(-1)^j\delta]\hat{\rho}_j$ is the electric dipole moment operator relevant to the open-boundary TTF-CA chain, with j and σ indexes running over the N molecular sites and the two possible spin polarizations, respectively. The TTF-to-CA distance is a=3.7 Å [172] and t=0.21 eV is used.

Consequently, the oscillator strength along the stack for the $|i\rangle$ to $|f\rangle$ transition reads:

$$f^a_{f\leftarrow i} = \frac{2m_e}{e^3}\frac{t^2a^2}{\hbar^2}\frac{|v_{fi}|^2}{\hbar\omega_{fi}}, \tag{3.27}$$

where $v_{fi} = \langle f|\hat{v}|i\rangle$ is the relevant velocity dipole matrix element. The oscillator strength is initially calculated on a grid of (q, δ) points from the ground state towards all the higher excited states, thus obtaining $f^a_{f\leftarrow GS}(\delta, q)$. After its interpolation, the oscillator strength is used to calculate absorption spectra at each time-step, adopting a Gaussian band shape with HWHM=0.09 eV. In Fig.3.12, the time-dependent spectrum of a neutral TTF-CA ring with N=8 is reported as a color map, showing a modulation of the CT band at the pump pulse frequency, as better shown by the time-section in the lower panel and by its Fourier transform in the inset.

3.6 Conclusions

Spectroscopic techniques relying on multiple ultrashort mid-IR and THz light pulses have become an invaluable tool for exploring the very complicated phase space of strongly correlated electronic systems, with the possibility to create transient out of equilibrium configurations and to follow their vibronic dynamics in real time.[50, 51]

In this Chapter, an exhaustive theoretical analysis of a recent pump-probe experiment on ET-F_2TCNQ crystal is presented. The experiment can be described in terms of a quadratic modulation of Hubbard U by $ET^{+\bullet}$ non-totally symmetric vibrations as originally suggested in Refs.[56, 57]. However, in the original works, optical spectra were reproduced by imposing a rather peculiar U/t time-dependence (Fig.3.2, panel c).

In Sect.3.1, the model Hamiltonian proposed in Refs.[56, 57] was fully validated against quantum chemical calculations. Moreover, accounting for a $(ET^{+\bullet})_2$ dimer, a fully non-adiabatic approach to the ET-F_2TCNQ pump-probe experiment was presented in Sect.3.2, where a rigorous calculation of the system quantum dynamics as induced by a mid-IR pulse was performed. To accurately reproduce the experimental data, the model was extended in order to account for energy dissipation through a quantum-classical hybrid approach. Actually, an adiabatic approach to the $(ET^{+\bullet})_2$ dimer model proved to be enough in studying the pump-probe experiment, as discussed in Sect.3.3, with no need to go to larger $ET^{+\bullet}$ clusters as shown in Sect.3.4.

Finally, some preliminary simulations of a novel pump-probe experiment on the neutral mixed stack CT crystal TTF-CA were presented in Sect.3.5. Using a mid-IR pump pulse polarized along the stack axis, an off-resonance driven motion of the lattice dimerization (Peierls) mode is induced. Because of the strong anharmonicity of the system, the motion is transferred from the driven phonon to the totally symmetric molecular vibrations, leading to a strong modulation of the CT band as shown in the color map in Fig.3.12.

Appendix D

Complete set of quadratic coupling constants

Complete set of results for $\mathrm{ET}^{+\bullet}$ vibrational modes as obtained from DFT calculations ((U)B3LYP/6-31G*) in gas phase.

Table D.1: For each normal mode (symmetry label in parenthesis) it is shown scaled vibrational frequency, ω_v, squared molecular dipole moment derivative with respect to the vibrational coordinate, η^2, and relevant electron-molecular vibration quadratic coupling constants.

mode (symmetry)	ω_v cm^{-1}	η^2 $(\mathrm{D}/\text{Å})^2\mathrm{amu}^{-1}$	$\frac{\partial^2 U}{\partial Q^2}$ meV	$\frac{\partial^2 \Delta}{\partial Q^2}$ meV	$\frac{\partial^2 V}{\partial Q^2}$ meV
1 (b3)	24	0.0029	14.0	21.4	0.0
2 (b3)	34	0.2242	-0.3	-6.6	1.5
3 (b2)	34	0.0003	0.7	-7.7	0.0
4 (a)	35	0.0000	0.6	2.7	0.0
5 (b2)	54	0.0081	-1.9	-5.0	0.0
6 (b2)	68	0.0006	-9.1	-16.0	0.0
7 (a)	98	0.0000	-6.9	3.2	0.0

Table D.1 – (Continued)

mode (symmetry)	ω_v cm^{-1}	η^2 $(\mathrm{D}/\text{Å})^2\mathrm{amu}^{-1}$	$\frac{\partial^2 U}{\partial Q^2}$ meV	$\frac{\partial^2 \Delta}{\partial Q^2}$ meV	$\frac{\partial^2 V}{\partial Q^2}$ meV
8 (b1)	102	0.0013	-8.7	-5.6	0.0
9 (a)	162	0.0000	-0.3	-2.7	0.0
10 (b3)	178	0.0001	2.6	-1.1	0.0
11 (b3)	259	0.0005	0.1	-5.1	0.0
12 (b1)	265	0.1949	-0.4	-0.4	0.2
13 (b2)	271	0.0730	0.5	-10.8	0.1
14 (b2)	274	0.0103	0.7	-10.8	0.0
15 (a)	274	0.0000	-0.7	0.2	0.0
16 (b3)	299	0.0580	-7.1	-13.3	0.0
17 (b1)	305	0.0924	0.5	-1.5	0.1
18 (a)	322	0.0000	0.6	-4.1	0.0
19 (b3)	354	0.0000	4.0	5.0	0.0
20 (b3)	360	0.0003	-0.9	5.9	0.0
21 (b2)	365	0.0003	-1.5	7.1	0.0
22 (b1)	409	0.4831	3.5	-2.0	0.3
23 (a)	459	0.0000	1.3	0.6	0.0
24 (b2)	477	0.0046	-0.9	0.6	0.0
25 (b3)	479	0.0027	-0.5	1.9	0.0
26 (b1)	490	1.6106	1.5	-3.4	0.8
27 (b2)	512	0.0010	0.4	0.0	0.0
28 (a)	516	0.0000	-0.3	1.5	0.0
29 (a)	525	0.0000	-0.1	-0.9	0.0
30 (b1)	527	0.0842	-0.4	-1.0	0.0
31 (b1)	647	0.4055	-1.2	3.8	0.1
32 (a)	647	0.0000	-1.3	3.8	0.0
33 (b2)	685	0.0831	-2.0	3.8	0.0
34 (b3)	685	0.0042	-2.0	3.9	0.0
35 (b3)	794	0.0090	0.6	0.3	0.0
36 (b2)	798	0.0915	0.1	-0.0	0.0

Table D.1 – (Continued)

mode (symmetry)	ω_v cm^{-1}	η^2 $(\mathrm{D}/\text{Å})^2\mathrm{amu}^{-1}$	$\frac{\partial^2 U}{\partial Q^2}$ meV	$\frac{\partial^2 \Delta}{\partial Q^2}$ meV	$\frac{\partial^2 V}{\partial Q^2}$ meV
37 (b1)	817	0.3323	0.5	-0.0	0.1
38 (b1)	895	0.1992	3.9	4.9	0.1
39 (a)	896	0.0000	0.6	7.8	0.0
40 (b2)	902	0.2281	5.4	7.3	0.1
41 (b3)	918	0.1611	-0.5	1.7	0.0
42 (b2)	927	0.0173	1.0	2.6	0.0
43 (b1)	958	0.2974	-0.6	0.7	0.1
44 (a)	958	0.0000	-0.6	0.8	0.0
45 (b1)	1028	0.1634	0.2	-0.5	0.0
46 (a)	1028	0.0000	0.2	-0.4	0.0
47 (b3)	1028	0.0017	-2.2	9.5	0.0
48 (b2)	1031	0.7663	-3.0	10.3	0.2
49 (b3)	1063	0.0060	4.1	6.3	0.0
50 (b2)	1178	0.0178	-0.6	0.0	0.0
51 (b3)	1179	0.0506	-0.6	0.0	0.0
52 (b1)	1238	0.0053	-0.1	-0.8	0.0
53 (a)	1238	0.0000	-0.1	-0.8	0.0
54 (b2)	1279	0.0000	-0.2	-0.4	0.0
55 (b3)	1279	0.1160	-0.2	-0.4	0.0
56 (b1)	1304	9.1920	-0.1	-0.4	1.6
57 (a)	1306	0.0000	-0.4	-0.6	0.0
58 (b1)	1405	67.2127	18.3	2.8	10.9
59 (a)	1407	0.0000	3.6	1.8	0.0
60 (b2)	1441	0.0965	-0.6	0.7	0.0
61 (b3)	1441	0.5795	-0.6	0.7	0.1
62 (a)	1445	0.0000	-0.6	0.9	0.0
63 (b1)	1445	0.4177	-0.6	0.9	0.1
64 (a)	1459	0.0000	4.2	0.4	0.0
65 (b3)	2993	0.0646	-0.3	-0.9	0.0

Table D.1 – (Continued)

mode (symmetry)	ω_v cm^{-1}	η^2 (D/Å)^{2}amu^{-1}	$\frac{\partial^2 U}{\partial Q^2}$ meV	$\frac{\partial^2 \Delta}{\partial Q^2}$ meV	$\frac{\partial^2 V}{\partial Q^2}$ meV
66 (b2)	2993	0.0092	-0.3	-0.9	0.0
67 (b1)	2997	0.0691	-0.2	-0.7	0.0
68 (a)	2997	0.0000	-0.2	-0.7	0.0
69 (b1)	3048	0.0089	-0.2	-1.0	0.0
70 (a)	3048	0.0000	-0.2	-1.0	0.0
71 (b2)	3059	0.0005	-0.2	-0.9	0.0
72 (b3)	3059	0.0133	-0.2	-0.9	0.0

Conclusions and future outlook

In this Thesis work, we have developed and applied new models, methods and computational approaches to considerably extend the potential of the host laboratory to describe and understand the behavior of complex systems.

Studying materials where both intramolecular and intermolecular charge-transfer degrees of freedom play a role (Chapter 2), we have investigated a new family of multifunctional materials whose complex phase diagram shows large regions of stability for ferroelectric states as well as sizeable regions of multiferroic behavior. This work must be extended in the first place via a tight connection with experimentalists, to experimentally validate the models. The adopted real-space diagonalization techniques must be extended to describe optical spectra, a first attempt in this direction being already present in this work (Sect.2.2). Extending the calculations to larger systems is also important. In this respect, during a four-months stay in India, in collaboration with Prof. Swapan Pati and Dr. Bradraj Pandey, I set up a suite of fermionic time-dependent DMRG (tDMRG) codes using the time-step targeting method (TST) developed by Feiguin and White.[173] Preliminary tDMRG results for chains with 8, 10 and 12 sites match well results obtained through exact diagonalization techniques. However, calculations for larger-size systems become time-consuming, and code parallelization is needed. To this aim, I started to implement MPI routines.

The fate of photoexcited states, i.e. the relaxation of a quantum system, is a central issue in spectroscopy with enormous implications in our understanding of open quantum systems. Different approaches and computational strategies have been explored in this work, applied to simple model systems for energy transfer. Very interesting fundamental results have been obtained about the advantages and limitations of different approaches. Preliminary results on solvation effects on energy transfer processes are extremely promising and definitely suggest the need to develop original strategies to jointly describe the dynamics of the energy donor-acceptor pair and the solvent dynamics using a combined Redfield/Fokker-Planck approach.

Relaxation phenomena are crucial to describe state of the art spectroscopic experiments and here we investigated in great detail a recent pump-probe experiment, where an ultrafast pump in the mid-IR region modulates the charge-transfer absorption spectrum, probed by a probe beam in the near-IR region. These experiments offer a solid basis to validate theoretical models for CT crystals and specifically to obtain reliable information about the electron-vibration coupling that governs the phase diagrams and the physics of these strongly-correlated electronic materials. Having developed reliable and portable strategies to model these experiments, we are now in the position to open tight collaborations with experimentalists designing new experiments to obtain crucial information on specific systems.

In conclusion, this Thesis, devoted to theoretical work, opens new perspectives to study the behaviour of multifunctional molecular materials, facing the complexity offered by delocalized and strongly correlated electrons, their interaction with nuclear degrees of freedom and with external electric fields. Relaxation phenomena, crucial to energy transfer processes and to understand advanced spectroscopic experiments, represent another source of complexity, bringing us into the fascinating realm of open quantum systems.

Bibliography

[1] D. M. Roundhill and J. P. J. Fackler, *Optoelectronic Properties of Inorganic Compounds*. Springer, Boston, MA, 1999.

[2] T. Sugawara, H. Komatsu, and K. Suzuki, "Interplay between magnetism and conductivity derived from spin-polarized donor radicals," *Chem. Soc. Rev.*, vol. 40, pp. 3105–3118, 2011.

[3] Z. Liu, A. A. Yasseri, J. S. Lindsey, and D. F. Bocian, "Molecular Memories That Survive Silicon Device Processing and Real-World Operation," *Science*, vol. 302, no. 5650, pp. 1543–1545, 2003.

[4] J. M. de la Fuente and S. Penadés, "Glyconanoparticles: Types, synthesis and applications in glycoscience, biomedicine and material science," *Biochimica et Biophysica Acta (BBA) - General Subjects*, vol. 1760, no. 4, pp. 636 – 651, 2006.

[5] A. Kargol, L. Malkinski, and G. Caruntu, *Advanced Magnetic Materials*, ch. 4, pp. 89–118. InTech, 2012.

[6] F. Castet, V. Rodriguez, J.-L. Pozzo, L. Ducasse, A. Plaquet, and B. Champagne, "Design and Characterization of Molecular Nonlinear Optical Switches," *Accounts of Chemical Research*, vol. 46, no. 11, pp. 2656–2665, 2013, and references therein.

[7] S. R. Marder and J. W. Perry, "Molecular materials for second-order nonlinear optical applications," *Advanced Materials*, vol. 5, no. 11, pp. 804–815, 1993.

[8] S. R. Marder, B. Kippelen, A. K.-Y. Jen, and N. Peyghambarian, "Design and synthesis of chromophores and polymers for electro-optic

and photorefractive applications," *Nature*, vol. 388, pp. 845–851, 1 1997.

[9] F. Bures, "Fundamental aspects of property tuning in push-pull molecules," *RSC Adv.*, vol. 4, pp. 58826–58851, 2014.

[10] J. Zyss, P. Kelley, and L. P. F., *Molecular Nonlinear Optics.* Academic Press, 1994.

[11] A. Painelli, "Amplification of NLO responses: vibronic and solvent effects in push-pull polyenes," *Chemical Physics*, vol. 245, no. 1, pp. 185 – 197, 1999.

[12] A. Painelli, "Vibronic contribution to static NLO properties: exact results for the DA dimer," *Chemical Physics Letters*, vol. 285, no. 5, pp. 352 – 358, 1998.

[13] B. Boldrini, E. Cavalli, A. Painelli, and F. Terenziani, "Polar Dyes in Solution: A Joint Experimental and Theoretical Study of Absorption and Emission Band Shapes," *The Journal of Physical Chemistry A*, vol. 106, no. 26, pp. 6286–6294, 2002.

[14] F. Terenziani, G. D'Avino, and A. Painelli, "Multichromophores for Nonlinear Optics: Designing the Material Properties by Electrostatic Interactions," *ChemPhysChem*, vol. 8, no. 17, pp. 2433–2444, 2007.

[15] A. Painelli and F. Terenziani, "Multielectron Transfer in Clusters of Polar-Polarizable Chromophores," *Journal of the American Chemical Society*, vol. 125, no. 19, pp. 5624–5625, 2003.

[16] C. Pecile, A. Painelli, and A. Girlando, "Studies of Organic Semiconductors for 40 Years-V," *Molecular Crystals and Liquid Crystals Incorporating Nonlinear Optics*, vol. 171, no. 1, pp. 69–87, 1989.

[17] G. D'Avino, A. Painelli, and Z. G. Soos, "Modeling the Neutral-Ionic Transition with Correlated Electrons Coupled to Soft Lattices and Molecules," *Crystals*, vol. 7, no. 5, 2017.

[18] M. Masino, N. Castagnetti, and A. Girlando, "Phenomenology of the Neutral-Ionic Valence Instability in Mixed Stack Charge-Transfer Crystals," *Crystals*, vol. 7, no. 4, 2017.

[19] J. B. Torrance, "The difference between metallic and insulating salts of tetracyanoquinodimethone (TCNQ): how to design an organic metal," *Accounts of Chemical Research*, vol. 12, no. 3, pp. 79–86, 1979.

[20] D. Jérome and H. Schulz, "Organic conductors and superconductors," *Advances in Physics*, vol. 31, no. 4, pp. 299–490, 1982.

[21] S. Horiuchi and Y. Tokura, "Organic ferroelectrics," *Nat. Mater.*, vol. 7, pp. 357–366, 2008.

[22] G. Giovannetti, S. Kumar, A. Stroppa, J. van den Brink, and S. Picozzi, "Multiferroicity in TTF-CA Organic Molecular Crystals Predicted through Ab Initio Calculations," *Phys. Rev. Lett.*, vol. 103, p. 266401, Dec 2009.

[23] F. Kagawa, S. Horiuchi, M. Tokunaga, J. Fujioka, and Y. Tokura, "Ferroelectricity in a one-dimensional organic quantum magnet," *Nat. Phys.*, vol. 6, pp. 169–172, 2010.

[24] J. B. Torrance, J. E. Vazquez, J. J. Mayerle, and V. Y. Lee, "Discovery of a Neutral-to-Ionic Phase Transition in Organic Materials," *Phys. Rev. Lett.*, vol. 46, pp. 253–257, Jan 1981.

[25] J. B. Torrance, A. Girlando, J. J. Mayerle, J. I. Crowley, V. Y. Lee, P. Batail, and S. J. LaPlaca, "Anomalous Nature of Neutral-to-Ionic Phase Transition in Tetrathiafulvalene-Chloranil," *Phys. Rev. Lett.*, vol. 47, pp. 1747–1750, Dec 1981.

[26] A. Painelli and A. Girlando, "Zero-temperature phase diagram of mixed-stack charge-transfer crystals," *Phys. Rev. B*, vol. 37, pp. 5748–5760, Apr 1988.

[27] M. Le Cointe, M. H. Lemée-Cailleau, H. Cailleau, B. Toudic, L. Toupet, G. Heger, F. Moussa, P. Schweiss, K. H. Kraft, and N. Karl, "Symmetry breaking and structural changes at the neutral-to-ionic transition in tetrathiafulvalene-p-chloranil," *Phys. Rev. B*, vol. 51, pp. 3374–3386, Feb 1995.

[28] F. Terenziani, C. Sissa, and A. Painelli, "Symmetry Breaking in Octupolar Chromophores: Solvatochromism and Electroabsorption,"

The Journal of Physical Chemistry B, vol. 112, no. 16, pp. 5079–5087, 2008.

[29] F. Terenziani and A. Painelli, "Supramolecular interactions in clusters of polar and polarizable molecules," *Phys. Rev. B*, vol. 68, p. 165405, Oct 2003.

[30] Z. G. Soos and A. Painelli, "Metastable domains and potential energy surfaces in organic charge-transfer salts with neutral-ionic phase transitions," *Phys. Rev. B*, vol. 75, p. 155119, Apr 2007.

[31] G. D'Avino, M. Masino, A. Girlando, and A. Painelli, "Correlated electrons in soft lattices: Raman scattering evidence of the nonequilibrium dielectric divergence at the neutral-ionic phase transition," *Phys. Rev. B*, vol. 83, p. 161105, Apr 2011.

[32] A. Painelli and A. Girlando, "Electron-molecular vibration (e-mv) coupling in charge-transfer compounds and its consequences on the optical spectra: A theoretical framework," *The Journal of Chemical Physics*, vol. 84, no. 10, pp. 5655–5671, 1986.

[33] G.-P. Borghi, A. Girlando, A. Painelli, and J. Voit, "Exact numerical diagonalization of one-dimensional interacting electrons nonadiabatically coupled to phonons," *EPL (Europhysics Letters)*, vol. 34, no. 2, p. 127, 1996.

[34] L. Del Freo, F. Terenziani, and A. Painelli, "Static nonlinear optical susceptibilities: Testing approximation schemes against exact results," *The Journal of Chemical Physics*, vol. 116, no. 2, pp. 755–761, 2002.

[35] G. D'Avino, F. Terenziani, and A. Painelli, "Aggregates of Quadrupolar Dyes: Giant Two-Photon Absorption from Biexciton States," *The Journal of Physical Chemistry B*, vol. 110, no. 51, pp. 25590–25592, 2006.

[36] C. Sissa, F. Terenziani, A. Painelli, A. Abbotto, L. Bellotto, C. Marinzi, E. Garbin, C. Ferrante, and R. Bozio, "Dimers of Quadrupolar Chromophores in Solution: Electrostatic Interactions and Optical Spectra," *The Journal of Physical Chemistry B*, vol. 114, no. 2, pp. 882–893, 2010.

[37] C. Sissa, A. K. Manna, F. Terenziani, A. Painelli, and S. K. Pati, "Beyond the Förster formulation for resonance energy transfer: the role of dark states," *Phys. Chem. Chem. Phys.*, vol. 13, pp. 12734–12744, 2011.

[38] C. Sissa, F. Terenziani, A. Painelli, A. Manna, and S. Pati, "Resonance energy transfer between polar charge-transfer dyes: A focus on the limits of the dipolar approximation," *Chemical Physics*, vol. 404, no. Supplement C, pp. 9 – 15, 2012.

[39] S. Sanyal, A. Painelli, S. K. Pati, F. Terenziani, and C. Sissa, "Aggregates of quadrupolar dyes for two-photon absorption: the role of intermolecular interactions," *Phys. Chem. Chem. Phys.*, vol. 18, pp. 28198–28208, 2016.

[40] B. Bardi, C. Dall'Agnese, K. I. Moineau-Chane Ching, A. Painelli, and F. Terenziani, "Spectroscopic Investigation and Theoretical Modeling of Benzothiadiazole-Based Charge-Transfer Chromophores: From Solution to Nanoaggregates," *The Journal of Physical Chemistry C*, vol. 121, no. 32, pp. 17466–17478, 2017.

[41] S. Sanyal, C. Sissa, F. Terenziani, S. K. Pati, and A. Painelli, "Superlinear amplification of the first hyperpolarizability of linear aggregates of DANS molecules," *Phys. Chem. Chem. Phys.*, vol. 19, pp. 24979–24984, 2017.

[42] J. Hubbard, "Electron correlations in narrow energy bands," *Proceedings of the Royal Society of London A: Mathematical, Physical and Engineering Sciences*, vol. 276, no. 1365, pp. 238–257, 1963.

[43] M. C. Gutzwiller, "Effect of correlation on the ferromagnetism of transition metals," *Phys. Rev. Lett.*, vol. 10, pp. 159–162, Mar 1963.

[44] J. Kanamori, "Electron correlation and ferromagnetism of transition metals," *Progress of Theoretical Physics*, vol. 30, no. 3, pp. 275–289, 1963.

[45] P. W. Anderson, "New Approach to the Theory of Superexchange Interactions," *Phys. Rev.*, vol. 115, pp. 2–13, Jul 1959.

[46] A. Painelli and A. Girlando, "Valence-bond analysis of half-filled Hubbard chains with long-range interelectronic interactions and on-site energy alternation," *Phys. Rev. B*, vol. 45, pp. 8913–8923, Apr 1992.

[47] L. Cavatorta, A. Painelli, and Z. G. Soos, "Coherent excitations at the neutral-ionic transition: Femtosecond dynamics on diabatic potential energy surfaces," *Phys. Rev. B*, vol. 91, p. 174301, May 2015.

[48] G. D'Avino, A. Girlando, A. Painelli, M.-H. Lemée-Cailleau, and Z. G. Soos, "Anomalous Dispersion of Optical Phonons at the Neutral-Ionic Transition: Evidence from Diffuse X-Ray Scattering," *Phys. Rev. Lett.*, vol. 99, p. 156407, Oct 2007.

[49] L. Del Freo, A. Painelli, and Z. G. Soos, "Giant Infrared Intensity of the Peierls Mode at the Neutral-Ionic Phase Transition," *Phys. Rev. Lett.*, vol. 89, p. 027402, Jun 2002.

[50] C. Giannetti, M. Capone, D. Fausti, M. Fabrizio, F. Parmigiani, and D. Mihailovic, "Ultrafast optical spectroscopy of strongly correlated materials and high-temperature superconductors: a non-equilibrium approach," *Advances in Physics*, vol. 65, no. 2, pp. 58–238, 2016.

[51] T. Morimoto, T. Miyamoto, and H. Okamoto, "Ultrafast Electron and Molecular Dynamics in Photoinduced and Electric-Field-Induced Neutral-Ionic Transitions," *Crystals*, vol. 7, p. 132, 2017.

[52] G. D. Scholes *et al.*, "Using coherence to enhance function in chemical and biophysical systems," *Nature*, vol. 543, no. 7647, pp. 647–656, 2017.

[53] P. V. Parandekar and J. C. Tully, "Mixed quantum-classical equilibrium," *The Journal of Chemical Physics*, vol. 122, no. 9, p. 094102, 2005.

[54] C. P. van der Vegte, A. G. Dijkstra, J. Knoester, and T. L. C. Jansen, "Calculating Two-Dimensional Spectra with the Mixed Quantum-Classical Ehrenfest Method," *The Journal of Physical Chemistry A*, vol. 117, no. 29, pp. 5970–5980, 2013.

[55] A. G. Redfield, “On the Theory of Relaxation Processes,” *IBM Journal of Research and Development*, vol. 1, no. 1, pp. 19–31, 1957.

[56] S. Kaiser *et al.*, “Optical Properties of a Vibrationally Modulated Solid State Mott Insulator,” *Sci. Rep.*, vol. 4, p. 3823, 2014.

[57] R. Singla *et al.*, “THz-Frequency Modulation of the Hubbard U in an Organic Mott Insulator,” *Phys. Rev. Lett.*, vol. 115, p. 187401, Oct 2015.

[58] G. D. Scholes, “Introduction: Light Harvesting,” *Chemical Reviews*, vol. 117, no. 2, pp. 247–248, 2017.

[59] D. L. Dexter, “A Theory of Sensitized Luminescence in Solids,” *The Journal of Chemical Physics*, vol. 21, no. 5, pp. 836–850, 1953.

[60] R. D. Harcourt, G. D. Scholes, and K. P. Ghiggino, “Rate expressions for excitation transfer. II. Electronic considerations of direct and through-configuration exciton resonance interactions,” *The Journal of Chemical Physics*, vol. 101, no. 12, pp. 10521–10525, 1994.

[61] T. Mirkovic, E. E. Ostroumov, J. M. Anna, R. van Grondelle, Govindjee, and G. D. Scholes, “Light Absorption and Energy Transfer in the Antenna Complexes of Photosynthetic Organisms,” *Chemical Reviews*, vol. 117, no. 2, pp. 249–293, 2017.

[62] L. Stryer and R. P. Haugland, “Energy transfer: a spectroscopic ruler,” *Proc. Natl. Acad. Sci. U. S. A.*, vol. 58, no. 2, pp. 719–726, 1967.

[63] V. Bagalkot, L. Zhang, E. Levy-Nissenbaum, S. Jon, P. W. Kantoff, R. Langer, and O. C. Farokhzad, “Quantum Dot-Aptamer Conjugates for Synchronous Cancer Imaging, Therapy, and Sensing of Drug Delivery Based on Bi-Fluorescence Resonance Energy Transfer,” *Nano Letters*, vol. 7, no. 10, pp. 3065–3070, 2007.

[64] M. J. Currie, J. K. Mapel, T. D. Heidel, S. Goffri, and M. A. Baldo, “High-Efficiency Organic Solar Concentrators for Photovoltaics,” *Science*, vol. 321, no. 5886, pp. 226–228, 2008.

[65] T. Förster, “Zwischenmolekulare Energiewanderung und Fluoreszenz,” *Annalen der Physik*, vol. 437, no. 1-2, pp. 55–75, 1948.

[66] T. Förster, “10th Spiers Memorial Lecture. Transfer mechanisms of electronic excitation,” *Discuss. Faraday Soc.*, vol. 27, pp. 7–17, 1959.

[67] T. Förster, “Transfer Mechanisms of Electronic Excitation Energy,” *Radiation Research Supplement*, vol. 2, pp. 326–339, 1960.

[68] V. May and O. Kühn, *Charge and Energy Transfer Dynamics in Molecular Systems.* Wiley-VCH Verlag GmbH & Co. KGaA, 2011.

[69] P. Mazur and E. Montroll, “Poincaré Cycles, Ergodicity, and Irreversibility in Assemblies of Coupled Harmonic Oscillators,” *Journal of Mathematical Physics*, vol. 1, no. 1, pp. 70–84, 1960.

[70] M. E. Tuckerman, *Statistical Mechanics: Theory and Molecular Simulation*, p. 588. Oxford University Press, 2010.

[71] A. Altland and B. Simons, *Condensed Matter Field Theory.* Cambridge University Press, 2010.

[72] R. Kubo, “The fluctuation-dissipation theorem,” *Reports on Progress in Physics*, vol. 29, no. 1, p. 255, 1966.

[73] S. Nakajima, “On Quantum Theory of Transport Phenomena: Steady Diffusion,” *Progress of Theoretical Physics*, vol. 20, no. 6, pp. 948–959, 1958.

[74] R. Zwanzig, “Ensemble Method in the Theory of Irreversibility,” *The Journal of Chemical Physics*, vol. 33, no. 5, pp. 1338–1341, 1960.

[75] S. Mukamel, *Principles of Nonlinear Optical Spectroscopy*, p. 67. Oxford University Press, 1995.

[76] D. Egorova, M. Thoss, W. Domcke, and H. Wang, “Modeling of ultrafast electron-transfer processes: Validity of multilevel Redfield theory,” *The Journal of Chemical Physics*, vol. 119, no. 5, pp. 2761–2773, 2003.

[77] D. Egorova and W. Domcke, “Quantum dynamical simulations of ultrafast photoinduced electron-transfer processes,” *Journal of Photochemistry and Photobiology A: Chemistry*, vol. 166, no. 1, pp. 19 – 31, 2004.

[78] W. T. Pollard and R. A. Friesner, “Solution of the Redfield equation for the dissipative quantum dynamics of multilevel systems,” *The Journal of Chemical Physics*, vol. 100, no. 7, pp. 5054–5065, 1994.

[79] R. K. Wangsness and F. Bloch, “The Dynamical Theory of Nuclear Induction,” *Phys. Rev.*, vol. 89, pp. 728–739, Feb 1953.

[80] P. R. Eastham, P. Kirton, H. M. Cammack, B. W. Lovett, and J. Keeling, “Bath-induced coherence and the secular approximation,” *Phys. Rev. A*, vol. 94, p. 012110, Jul 2016.

[81] B. Balzer and G. Stock, “Modeling of decoherence and dissipation in nonadiabatic photoreactions by an effective-scaling nonsecular Redfield algorithm,” *Chemical Physics*, vol. 310, no. 1, pp. 33 – 41, 2005.

[82] M. Barzoukas and M. Blanchard-Desce, “Molecular engineering of push-pull dipolar and quadrupolar molecules for two-photon absorption: A multivalence-bond states approach,” *The Journal of Chemical Physics*, vol. 113, no. 10, pp. 3951–3959, 2000.

[83] M. Albota *et al.*, “Design of Organic Molecules with Large Two-Photon Absorption Cross Sections,” *Science*, vol. 281, no. 5383, pp. 1653–1656, 1998.

[84] O. Mongin, L. Porrès, M. Charlot, C. Katan, and M. Blanchard-Desce, “Synthesis, Fluorescence, and Two-Photon Absorption of a Series of Elongated Rodlike and Banana-Shaped Quadrupolar Fluorophores: A Comprehensive Study of Structure-Property Relationships,” *Chemistry - A European Journal*, vol. 13, no. 5, pp. 1481–1498, 2007.

[85] D. Beljonne, W. Wenseleers, E. Zojer, Z. Shuai, H. Vogel, S. Pond, J. Perry, S. Marder, and J.-L. Brédas, “Role of Dimensionality on the Two-Photon Absorption Response of Conjugated Molecules: The Case of Octupolar Compounds,” *Advanced Functional Materials*, vol. 12, no. 9, pp. 631–641, 2002.

[86] W.-H. Lee, H. Lee, J.-A. Kim, J.-H. Choi, M. Cho, S.-J. Jeon, and B. R. Cho, “Two-Photon Absorption and Nonlinear Optical Properties of Octupolar Molecules,” *Journal of the American Chemical Society*, vol. 123, no. 43, pp. 10658–10667, 2001.

[87] C. Katan, F. Terenziani, O. Mongin, M. H. V. Werts, L. Porrès, T. Pons, J. Mertz, S. Tretiak, and M. Blanchard-Desce, "Effects of (Multi)branching of Dipolar Chromophores on Photophysical Properties and Two-Photon Absorption," *The Journal of Physical Chemistry A*, vol. 109, no. 13, pp. 3024–3037, 2005.

[88] F. Terenziani, A. Painelli, C. Katan, M. Charlot, and M. Blanchard-Desce, "Charge Instability in Quadrupolar Chromophores: Symmetry Breaking and Solvatochromism," *Journal of the American Chemical Society*, vol. 128, no. 49, pp. 15742–15755, 2006.

[89] R. S. Mulliken, "Molecular Compounds and their Spectra. II," *Journal of the American Chemical Society*, vol. 74, no. 3, pp. 811–824, 1952.

[90] A. Painelli and F. Terenziani, "Optical Spectra of Push-Pull Chromophores in Solution: A Simple Model," *The Journal of Physical Chemistry A*, vol. 104, no. 47, pp. 11041–11048, 2000.

[91] L. Del Freo and A. Painelli, "Anharmonicity and NLO responses: an exact diagonalization study," *Chemical Physics Letters*, vol. 338, no. 2, pp. 208 – 216, 2001.

[92] C. Sissa, F. Delchiaro, F. Di Maiolo, F. Terenziani, and A. Painelli, "Vibrational coherences in charge-transfer dyes: A non-adiabatic picture," *The Journal of Chemical Physics*, vol. 141, no. 16, p. 164317, 2014.

[93] F. Terenziani and A. Painelli, "Two-dimensional electronic-vibrational spectra: modeling correlated electronic and nuclear motion," *Phys. Chem. Chem. Phys.*, vol. 17, pp. 13074–13081, 2015.

[94] C. Sissa, V. Calabrese, M. Cavazzini, L. Grisanti, F. Terenziani, S. Quici, and A. Painelli, "Tuning the Nature of the Fluorescent State: A Substituted Polycondensed Dye as a Case Study," *Chemistry - A European Journal*, vol. 19, no. 3, pp. 924–935, 2013.

[95] W. Liptay, "Electrochromism and Solvatochromism," *Angewandte Chemie International Edition in English*, vol. 8, no. 3, pp. 177–188, 1969.

[96] S. Di Bella, T. J. Marks, and M. A. Ratner, "Environmental Effects on Nonlinear Optical Chromophore Performance. Calculation of Molecular Quadratic Hyperpolarizabilities in Solvating Media," *Journal of the American Chemical Society*, vol. 116, no. 10, pp. 4440–4445, 1994.

[97] A. Painelli and F. Terenziani, "A non-perturbative approach to solvatochromic shifts of push-pull chromophores," *Chemical Physics Letters*, vol. 312, no. 2, pp. 211 – 220, 1999.

[98] D. Feinberg, S. Ciuchi, and F. De Pasquale, "Squeezing Phenomena In Interacting Electron-Phonon Systems," *International Journal of Modern Physics B*, vol. 04, no. 07n08, pp. 1317–1367, 1990.

[99] F. Di Maiolo, M. Masino, and A. Painelli, "Terahertz-pulse driven modulation of electronic spectra: Modeling electron-phonon coupling in charge-transfer crystals," *Phys. Rev. B*, vol. 96, p. 075106, Aug 2017.

[100] L. Verlet, "Computer "Experiments" on Classical Fluids. I. Thermodynamical Properties of Lennard-Jones Molecules," *Phys. Rev.*, vol. 159, pp. 98–103, Jul 1967.

[101] N. G. Jensen and O. Farago, "A simple and effective Verlet-type algorithm for simulating Langevin dynamics," *Molecular Physics*, vol. 111, pp. 983–991, 2013.

[102] J. C. Tremblay and T. J. Carrington, "Using preconditioned adaptive step size Runge-Kutta methods for solving the time-dependent Schrödinger equation," *The Journal of Chemical Physics*, vol. 121, no. 23, pp. 11535–11541, 2004.

[103] H.-P. Breuer and F. Petruccione, *The Theory of Open Quantum Systems*, p. 129. Oxford University Press, 2010.

[104] A. Nitzan, *Chemical Dynamics in Condensed Phases*, p. 384. Oxford University Press, 2013.

[105] R. Fee and M. Maroncelli, "Estimating the time-zero spectrum in time-resolved emission measurements of solvation dynamics," *Chemical Physics*, vol. 183, no. 2, pp. 235 – 247, 1994.

[106] M. L. Horng, J. A. Gardecki, A. Papazyan, and M. Maroncelli, "Subpicosecond Measurements of Polar Solvation Dynamics: Coumarin 153 Revisited," *The Journal of Physical Chemistry*, vol. 99, no. 48, pp. 17311–17337, 1995.

[107] M. Am-Shallem, A. Levy, I. Schaefer, and R. Kosloff, "Three approaches for representing Lindblad dynamics by a matrix-vector notation," *arXiv:1510.08634 [quant-ph]*, 2015.

[108] A. Girlando, A. Painelli, S. Bewick, and Z. Soos, "Charge fluctuations and electron-phonon coupling in organic charge-transfer salts with neutral-ionic and Peierls transitions," *Synthetic Metals*, vol. 141, no. 1, pp. 129 – 138, 2004, and references therein.

[109] M. Masino, A. Girlando, and Z. G. Soos, "Evidence for a soft mode in the temperature induced neutral-ionic transition of TTF-CA," *Chemical Physics Letters*, vol. 369, no. 3, pp. 428 – 433, 2003.

[110] S. Horiuchi, Y. Okimoto, R. Kumai, and Y. Tokura, "Quantum Phase Transition in Organic Charge-Transfer Complexes," *Science*, vol. 299, no. 5604, pp. 229–232, 2003.

[111] A. Girlando, M. Masino, A. Painelli, N. Drichko, M. Dressel, A. Brillante, R. G. Della Valle, and E. Venuti, "Direct evidence of overdamped Peierls-coupled modes in the temperature-induced phase transition in tetrathiafulvalene-chloranil," *Phys. Rev. B*, vol. 78, p. 045103, Jul 2008.

[112] M. Dressel and N. Drichko, "Optical Properties of Two-Dimensional Organic Conductors: Signatures of Charge Ordering and Correlation Effects," *Chemical Reviews*, vol. 104, no. 11, pp. 5689–5716, 2004.

[113] S. Horiuchi, R. Kumai, and Y. Tokura, "Chemical Control of Ferroelectric Neutral-Ionic Transition in Charge-Transfer Complexes, $\mathrm{TTF}_{1-x}\mathrm{TSF}_x\mathrm{QCl}_4$ [TTF = Tetrathiafulvalene; TSF = Tetraselenafulvalene; QCl_4 = p-Chloranil]," *Journal of the American Chemical Society*, vol. 120, no. 29, pp. 7379–7380, 1998.

[114] K. Kobayashi, S. Horiuchi, R. Kumai, F. Kagawa, Y. Murakami, and Y. Tokura, “Electronic Ferroelectricity in a Molecular Crystal with Large Polarization Directing Antiparallel to Ionic Displacement,” *Phys. Rev. Lett.*, vol. 108, p. 237601, Jun 2012.

[115] J. Campo, A. Painelli, F. Terenziani, T. Van Regemorter, D. Beljonne, E. Goovaerts, and W. Wenseleers, “First Hyperpolarizability Dispersion of the Octupolar Molecule Crystal Violet: Multiple Resonances and Vibrational and Solvation Effects,” *Journal of the American Chemical Society*, vol. 132, no. 46, pp. 16467–16478, 2010.

[116] J. Roncali, “Molecular Bulk Heterojunctions: An Emerging Approach to Organic Solar Cells,” *Accounts of Chemical Research*, vol. 42, no. 11, pp. 1719–1730, 2009.

[117] S. Günes, H. Neugebauer, and N. S. Sariciftci, “Conjugated Polymer-Based Organic Solar Cells,” *Chemical Reviews*, vol. 107, no. 4, pp. 1324–1338, 2007.

[118] M. Grätzel, “Recent Advances in Sensitized Mesoscopic Solar Cells,” *Accounts of Chemical Research*, vol. 42, no. 11, pp. 1788–1798, 2009.

[119] S. R. Forrest, “The path to ubiquitous and low-cost organic electronic appliances on plastic,” *Nature*, vol. 428, pp. 911–918, 2004.

[120] M. S. T. Gonçalves, “Fluorescent Labeling of Biomolecules with Organic Probes,” *Chemical Reviews*, vol. 109, no. 1, pp. 190–212, 2009.

[121] M. Y. Berezin and S. Achilefu, “Fluorescence Lifetime Measurements and Biological Imaging,” *Chemical Reviews*, vol. 110, no. 5, pp. 2641–2684, 2010.

[122] H. Kobayashi, M. Ogawa, R. Alford, P. L. Choyke, and Y. Urano, “New Strategies for Fluorescent Probe Design in Medical Diagnostic Imaging,” *Chemical Reviews*, vol. 110, no. 5, pp. 2620–2640, 2010.

[123] G. D’Avino, L. Grisanti, J. Guasch, I. Ratera, J. Veciana, and A. Painelli, “Bistability in Fc-PTM Crystals: The Role of Intermolecular Electrostatic Interactions,” *Journal of the American Chemical Society*, vol. 130, no. 36, pp. 12064–12072, 2008.

[124] G. D'Avino, L. Grisanti, A. Painelli, J. Guasch, I. Ratera, and J. Veciana, "Cooperativity from electrostatic interactions: understanding bistability in molecular crystals," *CrystEngComm*, vol. 11, pp. 2040–2047, 2009.

[125] J. Guasch, L. Grisanti, M. Souto, V. Lloveras, J. Vidal-Gancedo, I. Ratera, A. Painelli, C. Rovira, and J. Veciana, "Intra- and Intermolecular Charge Transfer in Aggregates of Tetrathiafulvalene-Triphenylmethyl Radical Derivatives in Solution," *Journal of the American Chemical Society*, vol. 135, no. 18, pp. 6958–6967, 2013.

[126] J. Guasch, L. Grisanti, V. Lloveras, J. Vidal-Gancedo, M. Souto, D. C. Morales, M. Vilaseca, C. Sissa, A. Painelli, I. Ratera, C. Rovira, and J. Veciana, "Induced Self-Assembly of a Tetrathiafulvalene-Based Open-Shell Dyad through Intramolecular Electron Transfer," *Angewandte Chemie International Edition*, vol. 51, no. 44, pp. 11024–11028, 2012.

[127] M. Souto, J. Guasch, V. Lloveras, P. Mayorga, J. T. López Navarrete, J. Casado, I. Ratera, C. Rovira, A. Painelli, and J. Veciana, "Thermomagnetic Molecular System Based on TTF-PTM Radical: Switching the Spin and Charge Delocalization," *The Journal of Physical Chemistry Letters*, vol. 4, no. 16, pp. 2721–2726, 2013.

[128] J. B. Torrance, B. A. Scott, B. Welber, F. B. Kaufman, and P. E. Seiden, "Optical properties of the radical cation tetrathiafulvalenium (TTF^+) in its mixed-valence and monovalence halide salts," *Phys. Rev. B*, vol. 19, pp. 730–741, Jan 1979.

[129] Z. G. Soos, "Theory of π-Molecular Charge-Transfer Crystals," *Annual Review of Physical Chemistry*, vol. 25, no. 1, pp. 121–153, 1974.

[130] A. Girlando, R. Bozio, C. Pecile, and J. B. Torrance, "Discovery of vibronic effects in the Raman spectra of mixed-stack charge-transfer crystals," *Phys. Rev. B*, vol. 26, pp. 2306–2309, Aug 1982.

[131] J. Ferraris, D. O. Cowan, V. Walatka, and J. H. Perlstein, "Electron transfer in a new highly conducting donor-acceptor complex," *Journal of the American Chemical Society*, vol. 95, no. 3, pp. 948–949, 1973.

[132] M. Souto, M. V. Solano, M. Jensen, D. Bendixen, F. Delchiaro, A. Girlando, A. Painelli, J. O. Jeppesen, C. Rovira, I. Ratera, and J. Veciana, "Self-Assembled Architectures with Segregated Donor and Acceptor Units of a Dyad Based on a Monopyrrolo-Annulated TTF-PTM Radical," *Chemistry - A European Journal*, vol. 21, no. 24, pp. 8816–8825, 2015.

[133] M. Souto, D. Bendixen, M. Jensen, V. Díez-Cabanes, J. Cornil, J. Jeppesen, I. Ratera, C. Rovira, and J. Veciana, "Synthesis and Characterization of Ethylenedithio-MPTTF-PTM Radical Dyad as a Potential Neutral Radical Conductor," *Magnetochemistry*, vol. 2, p. 46, Dec 2016.

[134] Z. G. Soos and S. Mazumdar, "Neutral-ionic interface in organic charge-transfer salts," *Phys. Rev. B*, vol. 18, pp. 1991–2003, Aug 1978.

[135] H. M. McConnell, B. M. Hoffman, and R. M. Metzger, "CHARGE TRANSFER IN MOLECULAR CRYSTALS," *Proc. Natl. Acad. Sci. U. S. A.*, vol. 53, pp. 46–50, January 1965.

[136] Z. G. Soos and S. Ramasesha, "Valence-bond theory of linear Hubbard and Pariser-Parr-Pople models," *Phys. Rev. B*, vol. 29, pp. 5410–5422, May 1984.

[137] S. Sahoo and S. Ramasesha, "Full spin and spatial symmetry adapted technique for correlated electronic hamiltonians: Application to an icosahedral cluster," *International Journal of Quantum Chemistry*, vol. 112, no. 4, pp. 1041–1054, 2012.

[138] S. Ramasesha, "Electron-electron interactions in polyacetylene," *Journal of Chemical Sciences*, vol. 96, pp. 509–521, Apr 1986.

[139] Intel, *The Intel®Math Kernel Library Developer Reference.* 2017.

[140] R. Lehoucq, D. Sorensen, and C. Yang, *ARPACK Users' Guide.* Society for Industrial and Applied Mathematics, 1998.

[141] A. Painelli and A. Girlando, "Mixed regular stack charge-transfer crystals: Fundamental microscopic parameters from optical spectra," *The Journal of Chemical Physics*, vol. 87, no. 3, pp. 1705–1711, 1987.

[142] G. D'Avino and M. J. Verstraete, "Are Hydrogen-Bonded Charge Transfer Crystals Room Temperature Ferroelectrics?," *Phys. Rev. Lett.*, vol. 113, p. 237602, Dec 2014.

[143] D. C. Jiles and D. L. Atherton, "Theory of ferromagnetic hysteresis," *Journal of Magnetism and Magnetic Materials*, vol. 61, no. 1, pp. 48 – 60, 1986.

[144] R. Resta and S. Sorella, "Electron Localization in the Insulating State," *Phys. Rev. Lett.*, vol. 82, pp. 370–373, Jan 1999.

[145] R. Resta, "Why are insulators insulating and metals conducting?," *Journal of Physics: Condensed Matter*, vol. 14, no. 20, p. R625, 2002.

[146] E. Dagotto, "Complexity in Strongly Correlated Electronic Systems," *Science*, vol. 309, no. 5732, pp. 257–262, 2005.

[147] W. P. Su, J. R. Schrieffer, and A. J. Heeger, "Solitons in Polyacetylene," *Phys. Rev. Lett.*, vol. 42, pp. 1698–1701, Jun 1979.

[148] S. Mazumdar and Z. G. Soos, "Valence-bond analysis of extended Hubbard models: Charge-transfer excitations of molecular conductors," *Phys. Rev. B*, vol. 23, pp. 2810–2823, Mar 1981.

[149] Painelli, A. and Soos, Z. G., "Polarization and polarizability in extended one-dimensional organic materials," *Chemical Physics*, vol. 325, no. 1, pp. 48 – 59, 2006.

[150] P. F. Maldague, "Optical spectrum of a Hubbard chain," *Phys. Rev. B*, vol. 16, pp. 2437–2446, Sep 1977.

[151] M. J. Frisch *et al.*, "Gaussian 09 Revision D.01," Gaussian Inc. Wallingford CT (2009).

[152] G. Cerullo and S. De Silvestri, "Ultrafast optical parametric amplifiers," *Review of Scientific Instruments*, vol. 74, no. 1, pp. 1–18, 2003.

[153] S.-H. Shim, D. B. Strasfeld, E. C. Fulmer, and M. T. Zanni, "Femtosecond pulse shaping directly in the mid-IR using acousto-optic modulation," *Opt. Lett.*, vol. 31, pp. 838–840, Mar 2006.

[154] S.-H. Shim, D. B. Strasfeld, and M. T. Zanni, “Generation and characterization of phase and amplitude shaped femtosecond mid-IR pulses,” *Opt. Express*, vol. 14, pp. 13120–13130, Dec 2006.

[155] B. Green *et al.*, “High-Field High-Repetition-Rate Sources for the Coherent THz Control of Matter,” *Sci. Rep.*, vol. 6, p. 22256, 2016.

[156] C. Kübler, H. Ehrke, R. Huber, R. Lopez, A. Halabica, R. F. Haglund, and A. Leitenstorfer, “Coherent Structural Dynamics and Electronic Correlations during an Ultrafast Insulator-to-Metal Phase Transition in VO_2,” *Phys. Rev. Lett.*, vol. 99, p. 116401, Sep 2007.

[157] M. Liu *et al.*, “Terahertz-field-induced insulator-to-metal transition in vanadium dioxide metamaterial,” *Nature*, vol. 487, pp. 345–348, 2012.

[158] T. Kubacka *et al.*, “Large-Amplitude Spin Dynamics Driven by a THz Pulse in Resonance with an Electromagnon,” *Science*, vol. 343, no. 6177, pp. 1333–1336, 2014.

[159] S. Baierl, M. Hohenleutner, T. Kampfrath, A. K. Zvezdin, A. V. Kimel, R. Huber, and R. V. Mikhaylovskiy, “Nonlinear spin control by terahertz-driven anisotropy fields,” *Nature Photonics*, vol. 10, pp. 715–720, 2016.

[160] H. Uemura and H. Okamoto, “Direct Detection of the Ultrafast Response of Charges and Molecules in the Photoinduced Neutral-to-Ionic Transition of the Organic Tetrathiafulvalene-*p*-Chloranil Solid,” *Phys. Rev. Lett.*, vol. 105, p. 258302, Dec 2010.

[161] T. Miyamoto, H. Yada, H. Yamakawa, and H. Okamoto, “Ultrafast modulation of polarization amplitude by terahertz fields in electronic-type organic ferroelectrics,” *Nat. Commun.*, vol. 4, p. 2586, 2013.

[162] T. Morimoto, T. Miyamoto, H. Yamakawa, T. Terashige, T. Ono, N. Kida, and H. Okamoto, “Terahertz-field-induced large macroscopic polarization and domain-wall dynamics in an organic molecular dielectric,” *Phys. Rev. Lett.*, vol. 118, p. 107602, Mar 2017.

[163] A. Girlando, “Charge Sensitive Vibrations and Electron-Molecular Vibration Coupling in Bis(ethylenedithio)-tetrathiafulvalene (BEDT-TTF),” *J. Phys. Chem. C*, vol. 115, p. 19371, 2011.

[164] M. Mizuno, A. Garito, and M. Cava, “Organic Metals: Alkylthio Substitution Effects in Tetrathiafulvalene-Tetracyanoquinodimethane Charge-transfer Complexes,” *J. Chem. Soc., Chem. Commun.*, p. 18, 1978.

[165] T. Mori and H. Inokuchi, “Structural and electrical properties of (BEDT-TTF)(TCNQ),” *Solid State Communications*, vol. 59, no. 6, p. 355, 1986.

[166] T. Mori and H. Inokuchi, “Crystal Structure of the Mixed-Stacked Salt of Bis(ethylenedithio)-tetrathiafulvalene (BEDT-TTF) and Tetracyanoquinodimethane (TCNQ),” *Bull. Chem. Soc. Jpn.*, vol. 60, no. 1, p. 402, 1987.

[167] T. Hasegawa, S. Kagoshima, T. Mochida, S. Sugiura, and Y. Iwasa, “Electronic states and anti-ferromagnetic order in mixed-stack charge-transfer compound (BEDT-TTF)(F_2TCNQ),” *Solid State Communications*, vol. 103, no. 8, p. 489, 1997.

[168] S. Wall, D. Brida, S. R. Clark, H. P. Ehrke, D. Jaksch, A. Ardavan, S. Bonora, H. Uemura, Y. Takahashi, T. Hasegawa, H. Okamoto, G. Cerullo, and A. Cavalleri, “Quantum interference between charge excitation paths in a solid-state Mott insulator,” *Nat. Phys.*, vol. 7, p. 114, 2011.

[169] A. Girlando, L. Grisanti, M. Masino, I. Bilotti, A. Brillante, R. G. Della Valle, and E. Venuti, “Peierls and Holstein carrier-phonon coupling in crystalline rubrene,” *Phys. Rev. B*, vol. 82, p. 035208, Jul 2010.

[170] E. Scriven and B. J. Powell, “Toward the parametrization of the Hubbard model for salts of bis(ethylenedithio)tetrathiafulvalene: A density functional study of isolated molecules,” *The Journal of Chemical Physics*, vol. 130, no. 10, p. 104508, 2009.

[171] A. Fortunelli and A. Painelli, “Ab initio estimate of Hubbard model parameters: A simple procedure applied to BEDT-TTF salts,” *Phys. Rev. B*, vol. 55, pp. 16088–16095, Jun 1997.

[172] Z. G. Soos, S. A. Bewick, A. Peri, and A. Painelli, “Dielectric response of modified Hubbard models with neutral-ionic and Peierls transitions,” *The Journal of Chemical Physics*, vol. 120, no. 14, pp. 6712–6720, 2004.

[173] A. E. Feiguin and S. R. White, “Time-step targeting methods for real-time dynamics using the density matrix renormalization group,” *Phys. Rev. B*, vol. 72, p. 020404, Jul 2005.

List of publications

- F. Di Maiolo and C. Sissa and A. Painelli, “Combining intra- and intermolecular charge-transfer: a new strategy towards molecular ferromagnets and multiferroics,” *Scientific Reports*, vol. 6, p. 19682, 2016.
- F. Di Maiolo and M. Masino and A. Painelli, “Terahertz-pulse driven modulation of electronic spectra: Modeling electron-phonon coupling in charge-transfer crystals,” *Phys. Rev. B*, vol. 96, p. 075106, 2017.

Acknowledgements

I want to thank my PhD supervisor Prof. Anna Painelli for her constant support and invaluable guidance. I will never forget her passionate voice while explaining Quantum Mechanics!

I also want to thank all the other members of the research group: Prof. Alberto Girlando, Prof. Francesca Terenziani, Prof. Matteo Masino, Dr. Cristina Sissa.

During my stay in Bangalore, India, I had the honor to collaborate with Prof. Swapan K. Pati, one of the world's leading experts in Density Matrix Renormalization Group (DMRG) algorithm. I wish to thank him for his guidance and help.

Furthermore, I want to thank all my labmates: Dr. Francesca Delchiaro, Dr. Somananda Sanyal, Dr. Nicola Castagnetti, Dr. Siarhei Kurhuzenkau and Dr. Domna-Maria Nikolaidou. A special mention undoubtedly goes to Dr. Bradraj Pandey with whom I collaborated during a four-month period in India. We worked non stop on the development and parallelization of time-dependent DMRG (tDMRG) algorithm, mutually exchanging our knowledge.

Last but not least, I want to thank my whole family for trusting and encouraging me.

The work presented in this Thesis was supported by the Italian Ministry for Education through:

- FIRB RBFR10Y5VW, "Studio del flusso di energia e di carica in nuovi sistemi multicromoforici sintetizzati ad hoc, di complessità controllata e crescente: verso sistemi intelligenti per la fotovoltaica organica";
- PRIN 2010ERFKXL, "Studi di frontiera in spettroscopia e dinamica

molecolare: da sistemi molecolari semplici ad aggregati supramolecolari e materiali avanzati";

- PRIN 2012T9XHH7, "Nuovi aspetti del trasferimento di energia risonante in mezzi organizzati: effetti dinamici e controllo ottico".

I thank the *Indo-Italian Executive Programme of Scientific & Technological Cooperation* for one-month stay in India during 2015. I thank the *Overworld program 2015-2016* for the scholarship during the four-month stay in India during 2016.

I thank CINECA for HPC projects: IsC20_MMMmodel, IsC28_MMM2, IsC35_MMMoptic, IsC43_MMM-CT, IsC50_MMM-time.

This Thesis is dedicated to Mary.